Bottom quark charge identification using muons in jets

Master's Thesis

Bc. Lukáš Novotný

Faculty of Nuclear Sciences and Physical Engineering
CZECH TECHNICAL UNIVERSITY IN PRAGUE

Department of Physics

Supervisor: Ing. Michal Marčišovský, Ph.D.
Prague, 2018

Identifikace náboje bottom kvarků pomocí mionů v jetech

Diplomová práce

Bc. Lukáš Novotný

Fakulta jaderná a fyzikálně inženýrská
České vysoké učení technické v Praze

Katedra fyziky

Vedoucí práce: Ing. Michal Marčišovský, Ph.D.
Praha, 2018

Abstract

TITLE:	Bottom quark charge identification using muons in jets
AUTHOR:	Lukáš Novotný
SPECIALIZATION:	Experimental nuclear and particle physics
SORT OF PROJECT:	Master's thesis
SUPERVISOR:	Ing. Michal Marčišovský, Ph.D.
ABSTRACT:	This thesis is dedicated to the study of the tag power and tag probability of a B^+ meson, which is used as the calibration tool in a $B_s^0 \to J/\psi\phi$ opposite side tagging. For this purpose, the whole 2015 and 2016 datasets recorded by the ATLAS detector at the LHC are used. In introductory chapter, the Standard Model with emphasis on the CKM formalism is presented, followed by the theoretical background of $B_s^0 - \bar{B}_s^0$ mixing in the $B_s^0 \to J/\psi\phi$ decay mode. Further chapters are devoted to the ATLAS detector description and ATLAS trigger system and offline software. The thesis concludes with the tagging studies with new results applied to the ongoing ATLAS analysis.
KEY WORDS:	B physics, CP violation, tag probability, ATLAS, LHC

Abstrakt

NÁZEV PRÁCE:	Identifikace náboje bottom kvarků pomocí mionů v jetech
AUTOR:	Lukáš Novotný
OBOR:	Experimentální jaderná a částicová fyzika
DRUH PRÁCE:	Diplomová práce
VEDOUCÍ PRÁCE:	Ing. Michal Marčišovský, Ph.D.
ABSTRAKT:	Tato práce se věnuje tagování mezonu B^+, jehož tagovací pravděpodobnost je použita pro kalibraci tagování mezonu $B_s^0 \to J/\psi\phi$. Pro tento účel byla použita data z pp srážek získaná detektorem ATLAS na LHC v letech 2015 a 2016. Zpočátku se práce věnuje Standardnímu modelu částic a interakcí s důrazem mechanismus mixování kvarků v Standardním modelu. Následuje teoretický popis CP narušení v $B_s^0 - \bar{B}_s^0$ oscilaci. Poté je popsán systém triggerování a offline software na detektoru ATLAS. Na závěr je ukázán analyzační model a získané výsledky analýzy získané v rámci analyzační ATLAS skupiny.
KLÍČOVÁ SLOVA:	B fyzika, CP narušení, pravděpodobnost tagování, ALTAS, LHC

Acknowledgements

I would like to express my gratitude to my supervisor Michal Marčišovský for his invaluable advice, patience, willingness and professional guidance during the realization of this work. I am very grateful to Mária Marčišovská for language corrections and to Václav Vrba for overall support of my work. Furthermore, I would like to thank James William Walder, Adam Edward Barton and Radek Novotný for preparing the data sample and helping with data analysis and Mária Smižanská for her helpful advices and discussions. Last but not least, I would like to thank my girlfriend Kristýna Šrámková, my whole family and friends for their encouragement and support during my studies.

Lukáš Novotný

Declaration

I hereby declare that this project is the result of my own work and all the sources I used are in the list of references. I have no objection to usage of this work in compliance with the act §60 Law No. 121/2000 Coll. (Copyright Act), and with the rights connected with the copyright act including the changes in the act.

Prohlášení

Prohlašuji, že jsem tuto práci vypracoval samostatně a použil jsem pouze podklady uvedené v přiloženém seznamu. Nemám závažný důvod proti použití tohoto díla ve smyslu §60 zákona č.121/2000 Sb., o právu autorském, o právech souvisejících s právem autorským a o změně některých zákonů (autorský zákon).

V Praze dne: ....

Lukáš Novotný

Table of Contents

List of Tables

Table **Page**

List of Figures

Figure **Page**

Introduction

The CP violating phase ϕ_s arises in the interference between the amplitudes of B_s^0 mesons decaying via $b \to s$ transitions and those decaying after oscillation. The flavour tagging has significant impact on the precision of the ϕ_s phase studies, especially in the case the opposite side tagging.

To study and calibrate the opposite side tagging method, the decay, where the sign of a B meson is known is used. It is amongst important contributions of the author of this thesis to the ongoing analysis.

This diploma thesis is organised as follows: The first chapter gives a brief overview of the Standard Model, paying particular attention to the concepts surrounding discrete symmetries and CKM formalism.

The second chapter is dedicated to the theoretical background of the $B_s^0 - \bar{B}_s^0$ mixing. The B meson properties are followed by $B_s^0 - \bar{B}_s^0$ mixing overview in the $B_s^0 \to J/\psi\phi$ decay mode. The difference between flavour and mass eigenstates is described there, leading to the measured differential branching ratio in terms of transversality formalism. Previous measurements of CP violation at D0, LHCb, CMS and ATLAS detectors are briefly described at the end of this chapter.

Third chapter introduces the ATLAS and its subdetectors, followed by the fourth chapter, where the ATLAS trigger system and the ATLAS offline software are introduced. The muon reconstruction method is described here, dividing muons into groups according to the available hit information input used for the reconstruction algorithms and their quality of reconstruction. The software used in this analysis is also described in this chapter, namely ROOT, RooFit and sPlot.

The main part of this work is presented in the final two chapters. The $B^{\pm}$ flavour tagging analysis, such as the candidate reconstruction and the determination of the selection cut, is discussed in the fifth chapter. The results of $B^{\pm} \to J/\psi K^{\pm}$ mass fit are discussed here, followed by the description of the sideband subtraction method. Further, the single muon tagging and cone charge tagging results with respect to the cuts and parameters variations are presented. The partial resulting observables employed in the construction

of the tag variables together with the production of calibration curves for B_s^0 flavour tagging is discussed at the end of the fifth chapter.
The sixth chapter presents the usage of the calibration curves in the B_s^0 tag probability production. These probabilities are fitted and used in the B_s^0 angular fit, giving the increased sensitivity on variables of interest, such as ϕ_s, Γ_s and $\Delta\Gamma$. The calculation of systematic uncertainties is discussed at the end of this chapter.

CHAPTER 1

INTRODUCTION TO THE PARTICLE PHYSICS

Contemporary instrumentation and predictive theoretical models allow us to describe behaviour of the observable world on the elementary particle level. These objects and their mutual interactions are described by the Standard Model of particles and fields. According to this model, all observable matter is made of particles without inner structure, called elementary particles, and they interact through force carriers.

1.1 The Standard Model

This theory, developed in the 1970s, successfully explains collider experimental results. It contains 6 bosons with integer fundamental spin and 12 fermions with half-integer fundamental spin. Fermions obey Fermi-Dirac statistics and bosons obey Bose-Einstein statistics. For more details about particle species and their physical properties, see Table 1.1.

1.1.1 Fundamental Interactions

There are four known fundamental interactions - strong, electromagnetic, weak and gravitational, but only the first three are incorporated into the Standard Model and are mediated by gauge bosons enumerated in Table 1.1. In our everyday macroscopic and mundane life, the gravitational and electromagnetic forces are usually observed,

family		symbol	name	mass	spin	charge
fermions	quarks	u	up	$2.3^{+0.7}_{-0.5}$ MeV	1/2	2/3
		d	down	$4.8^{+0.5}_{-0.3}$ MeV	1/2	−1/3
		s	strange	95 ± 5 MeV	1/2	−1/3
		c	charm	1.275 ± 0.025 GeV	1/2	2/3
		b	bottom	4.18 ± 0.03 GeV	1/2	−1/3
		t	top	$173.21 \pm 0.51 \pm 0.71$ GeV	1/2	2/3
	leptons	e	electron	510.998928 ± 0.000011 keV	1/2	-1
		μ	muon	$105.6583715 \pm 0.0000035$ MeV	1/2	-1
		τ	tau	1776.82 ± 0.16 MeV	1/2	-1
		ν_e	e-neutrino	< 2 eV	1/2	0
		ν_μ	μ-neutrino	< 0.19 MeV	1/2	0
		ν_τ	τ-neutrino	< 18.2 MeV	1/2	0
bosons	vector	γ	photon	$< 10^{-18}$ eV	1	0
		g	gluon	0	1	0
		$W^\pm$	W boson	80.385 ± 0.015 GeV	1	±1
		Z^0	Z boson	91.1876 ± 0.0021 GeV	1	0
	scalar	H	Higgs boson	125.7 ± 0.4 GeV	0	0

TABLE 1.1. Particles (6 quarks and 6 leptons) and force carriers (6 bosons) in the Standard Model [1]. The Higgs boson is a recently observed particle [2].

strong and weak interaction become important at the distance scales of 10^{-15} m and smaller. The comparison of the strength of each interaction (except gravitation) is shown in Figure 1.1.

1.1.1.1 Electromagnetic Interaction

Electromagnetic interactions between charged particles are mediated by a photon exchange. Particles with the same sign of electric charge exert repelling force onto each other and particles with the opposite charge attract each other. The value of the coupling constant, or the fine structure constant, equals at low energy limit to:

$$\alpha = \frac{1}{4\pi\varepsilon_0}\frac{e^2}{\hbar c} \simeq \frac{1}{137}, \tag{1.1}$$

where e is the elementary charge, $\hbar$ is reduced Planck constant, c is the speed of light in vacuum and ε is vacuum permeability. The lightest charged particle is the electron

	gravitational	electromagnetic	weak	strong
boson	graviton[1]	photon	$W^{\pm}$, Z^0	gluons
spin-parity	2^+	1^-	1^-, 1^+	1^-
mass [GeV/c^2]	0[2]	0	$m_W = 80.2$, $m_Z = 91.2$	0
range [m]	∞	∞	10^{-18}	$\leq 10^{-15}$
coupling constant	$\frac{G_N M^2}{4\pi\hbar c} = 5 \cdot 10^{-40}$	$\alpha = \frac{e^2}{4\pi\hbar c} = \frac{1}{137}$	$\frac{G(Mc^2)^2}{(\hbar c)^3} = 1 \cdot 10^{-5}$	$\alpha_S \lesssim 1$

TABLE 1.2. Fundamental interactions [4].

with a lifetime $\tau_e > 6.6 \cdot 10^{28}$ years [3]. Because electron can decay only by violating the charge conservation law and since this violation has not been observed in nature, it is assumed, that in every interaction or decay, the total electric charge is conserved. The electromagnetic interaction is formulated within the quantum electrodynamics framework (QED). In this theory, the definition of α (1.1) is not constant, but it depends on the energy scale at which the measurement is made, such as

$$\alpha\left(Q^2\right) = \frac{\alpha(0)}{1 - \frac{\alpha(0)}{3\pi}\ln\left(Q^2/m_e^2\right)}, \tag{1.2}$$

where $\alpha(0) = 1/137$, m_e is electron mass and Q^2 is negative transferred four momentum. At the energy scales of the Z^0 boson mass, the coupling constant $\alpha \simeq \frac{1}{128}$.

1.1.1.2 Gravitational Interaction

The effects of the gravitational interaction demonstrate themselves predominantly in the macroscopic world and especially at large spatial scales, where it was observed that gravitating objects curve the spacetime around themselves. This curvature can manifest itself by exerting a force on a nearby objects or in the language of general theory of relativity, object follows the geodesic curves. The gravity binds objects to the surface of the Earth, holds together star clusters, galaxies and clusters of galaxies. Its coupling strength is defined by the Newtonian constant

$$G = 6.673 \cdot 10^{-11}\,\mathrm{m^3kg^{-1}s^{-2}}, \tag{1.3}$$

[1]The graviton is a hypothetical particle, which is not included in the Standard Model, because consistent and predictive quantum gravity theory has not been formulated yet. However, the gravitational waves (pertubations in linearized spacetime) were observed in 2016 [5].

[2]The mass of graviton is expected to be zero in four dimensions (three space and one time dimension), but it can have nonzero mass in theories with more dimensions.

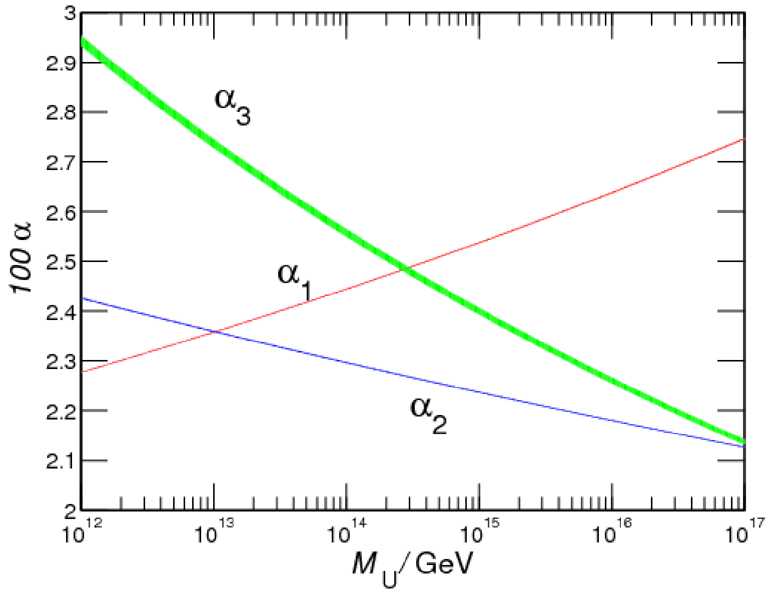

FIGURE 1.1. The running of the gauge couplings in the Standard Model in dependence on the energy scale (note the logarithmic scale). α_1 corresponds to electromagnetic coupling, α_2 to weak and α_3 to the strong coupling [6].

which is a constant used in the Einstein field equations of the general theory of relativity:

$$R_{\mu\nu} - \frac{1}{2} R g_{\mu\nu} + \Lambda g_{\mu\nu} = \frac{8\pi G}{c^4} T_{\mu\nu}, \tag{1.4}$$

where $R_{\mu\nu}$ is the Ricci curvature tensor, R is the scalar curvature (the Ricci scalar), $g_{\mu\nu}$ is the metric tensor, Λ is cosmological constant (the value of the energy density of the vacuum of space) and $T_{\mu\nu}$ is the stress-energy tensor generalizing the stress tensor of Newtonian physics [7].

In the Newtonian approach, the magnitude of the force between two point particles with mass M and distance r is given by $\frac{G_N M^2}{r^2}$. When calculating the electromagnetic force strength between charged particles, e^2/r^2, we can substitute GM^2 in the definition (1.1) for e^2/ε_0 and obtain a constant

$$\frac{GM^2}{4\pi\hbar c} = 5.34 \cdot 10^{-40}. \tag{1.5}$$

This value demonstrates the relative strength of the gravity to electromagnetism. In comparison with the fine structure constant (1.1), the gravitational interaction is negligibly small at the high energy physics scale and it is not included in the Standard Model. On the other hand, gravitational interaction is crucial at large spatial scales such as in orbital dynamics and cosmology, because it is a long-distance interaction. Moreover,

there has not been observed a negative gravitational charge yet.
Therefore, the gravitational force is only attractive and it is hypothetically mediated through the graviton in the corresponding quantum field theories [8]. In the four dimensional models, it is a massless particle with spin 2. As noted in the footnote of the Table 1.2, the gravitational waves have been recently observed, but the graviton particle has not been observed yet.

1.1.1.3 Strong Interaction

Unlike leptons, quarks and gluons interact via the strong interaction. This force is responsible for binding quarks and gluons together, forming mesons and baryons (and other exotic states like tetraquarks and pentaquarks). The strong interaction is described within the quantum chromodynamics framework (QCD).
After observation of the three up quark system, Δ^{++} in 1952 [9], the color quantum number has been introduced as an extra degree of freedom in the quark model in order for quarks in baryons to not violate the Pauli exclusion principle. Every quark has assigned either red (r), blue (b) or green (g) colour. Similarly, antiquarks have their anticolour (antired - $\bar{r}$, antiblue - $\bar{b}$ or antigreen $\bar{g}$). O. Greenberg [10] proposed that the non-Abelian group represented by the 3×3 unitary matrices $\mathrm{SU(3)}_C$ is the local symmetry corresponding to the gauge field of the QCD [11]. For $\mathrm{SU(3)}_C$, we obtain $N^2-1=3^2-1=8$ gluons, represented by 8 generators derived from Gell-Mann matrices λ^C_{ab}.
The dynamics of the quarks and gluons (massless particle with spin 1) is defined by the gauge invariant QCD Lagrangian

$$\mathscr{L}=\sum_{q,C}\bar{\psi}_{q,a}\left(i\gamma^\mu\partial_\mu\delta_{ab}-g_s\gamma^\mu t^C_{ab}G^C_\mu-m_q\delta_{ab}\right)\psi_{q,b}-\frac{1}{4}G^A_{\mu\nu}G^{A\mu\nu}, \tag{1.6}$$

where $\psi_{q,a}$ are quark-field spinors for a quark q with mass m_q and color index a, that runs from 1 to $N_c=3$ since quarks can have assigned one of three colours. The γ_μ are Dirac matrices, G^C_μ stands for the gluon field with C running from 1 to $N_c^2-1=8$. The $t^C_{ab}=\lambda^C_{ab}/2$ correspond to the Gell-Mann matrices. The quantity g_s is the QCD coupling constant and $G^A_{\mu\nu}$ is field-strength tensor given by

$$G^A_{\mu\nu}=\partial_\mu G^A_\nu-\partial_\nu G^A_\mu-g_s f_{ABC}G^B_\mu G^C_\nu, \tag{1.7}$$

where f_{ABC} are structure constants of the SU(3) group.
The interaction between two colour charged particles is characterized by the running

coupling constant α_s which is related to the QCD coupling constant g_s,

$$\alpha_s\left(Q^2\right) = \frac{g_s^2\left(Q^2\right)}{4\pi} \approx \frac{12\pi}{\left(33-12N_f\right)\ln\left(Q^2/\Lambda_{QCD}\right)}, \tag{1.8}$$

where N_f is the number of quark flavours, $Q^2 = -q^2$ is negative transferred four momentum and $\Lambda_{QCD} \sim 0.2\,\mathrm{GeV}$ is the non-perturbative scale of QCD (energy at which the perturbative coupling diverges).

1.1.1.4 Weak Interaction

Unlike the strong and electromagnetic interactions with their massless gluons and photons, the weak interaction is mediated through the exchange of heavy gauge bosons $W^{\pm}$ and Z^0. Due to their large invariant masses, physicists were unable to experimentally observe them until the particle accelerators were powerful enough to produce them.
An example of the common weak interaction is the β decay (Fig. 1.2) of a neutron inside nucleus

$$n \to p + e^- + \overline{\nu}. \tag{1.9}$$

The last term (particle $\overline{\nu}$) in equation (1.9) was postulated by Wolfgang Pauli [12] and named (anti)neutrino in 1931 by Enrico Fermi. On the quark level of interaction, the

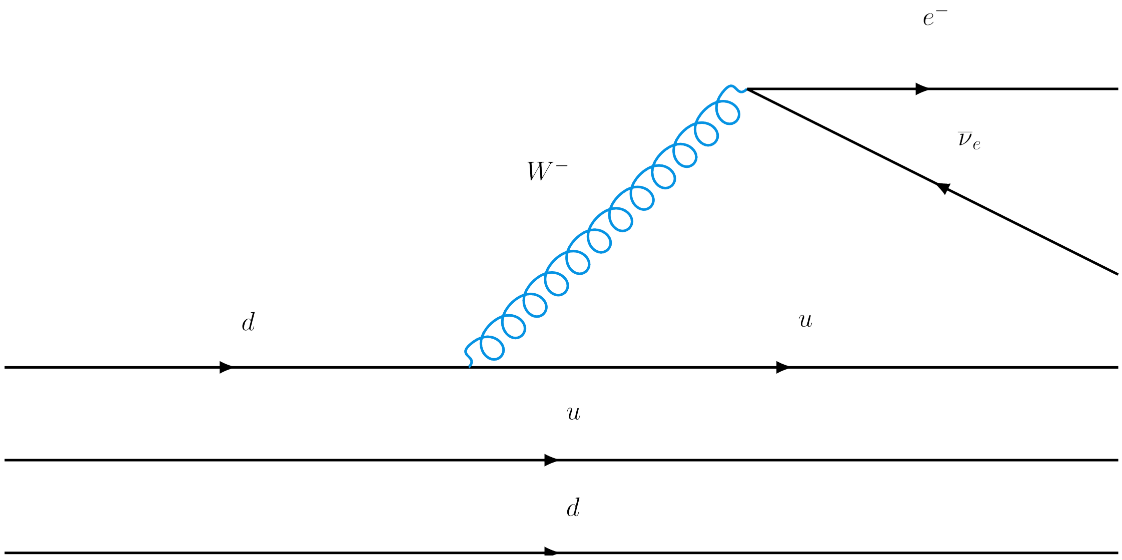

FIGURE 1.2. The neutron (valence quarks ddu) decaying into proton (valence quarks udu), electron and electron antineutrino via the weak interaction.

down quark d radiates the virtual W^- boson while transforming to the up quark u. This virtual boson then decays into electron e^- and electron anti-neutrino $\bar{\nu}$. In the Standard Model, this transformation of one quark into another quark is possible only in the weak reactions and it is described by the CKM matrix (for further details jump to the section 1.3).

Electroweak unification Each of the three fermion generations is represented in a pair of particles, forming electroweak doublets[3]. Electromagnetic interaction affects only particles with non-zero electric charge and weak interaction acts on the entire left-handed doublet. The electromagnetic force always conserves electric charge and can be modelled by the commutative group U(1). Weak interaction act on a particle doublet, so 2×2 matrices are necessary for weak interactions and so the Pauli matrices $\sigma_1/2$, $\sigma_2/2$ and $\sigma_3/2$ form the group SU(2). However, the generator σ_3 violates the total electromagnetic charge due to the one of diagonal components equal to -1. This can be fixed by combining electromagnetic and weak interaction into a group

$$\mathrm{SU}(2)_L \bigotimes \mathrm{U}(1)_Y, \tag{1.10}$$

where L refers to left-handed fields and Y is the hypercharge. This group has four generators (three for weak group and one for electromagnetic group), therefore four gauge bosons (W_1, W_2, W_3 and B) exist. Linear combination of these yields into the observable gauge bosons W^+ and W^-, which carry the charged current (where the flavour of the fermion is changed), and Z and γ, which carry the the neutral current. Flavour changing neutral currents (FCNC) are suppressed in the Standard Model in tree-level processes.

1.1.2 Leptons

In the current state of knowledge, six leptons are known to exist. Negatively charged leptons are electron e (believed to be stable), unstable muon μ and tau τ with mean lifetimes $t_\mu = 2.197 \cdot 10^{-6}$ s for μ and $t_\tau = 2.9 \cdot 10^{-13}$ s for τ respectively [1]. Corresponding flavour neutrino ν (with zero electromagnetic charge) partners with each of charged leptons.
All leptons have spin 1/2 and interact weakly, but only charged leptons interact electromagnetically. Thus, neutrinos can pass through the ordinary matter much more easily

[3]The helicity of particle is right-handed, if its spin is same as the direction of motion. The left-handed particles have opposite directions of spin and motion

than other leptons. It is assumed in the Standard Model that neutrinos are massless, however neutrino flavour mixing and flavour oscillations have been observed, which implies that neutrinos are not massless particles [4] and that the Standard Model is an incomplete theory.

1.1.3 Quarks

Similarly to leptons, quarks are fermions and form three electroweak doublets

$$\begin{pmatrix} u \\ d \end{pmatrix}, \begin{pmatrix} c \\ s \end{pmatrix}, \begin{pmatrix} t \\ b \end{pmatrix}. \tag{1.11}$$

Quarks u and d form first, s and c second and t and b third generation. The upper part of doublets has electric charge 2/3 (u, c and t) and the bottom part has charge of $-1/3$ (d, s and b). Quarks interact through all known fundamental forces, and are the only ones which do through the strong force, because they carry color charge.
The existence of quarks was independently postulated in 1964 by G. Zweig [14] and M. Gell-Mann [15]. Only up, down and strange quarks were known at the time. Other quarks were discovered later, charm quark in 1974 [16], bottom quark in 1977 [17] and top quark in 1995 [18].
Quarks can exist only in a bound state with another quarks or antiquarks, separate single quark has not been observed, except for the top quark, which decays before it has a chance to hadronize due to its small lifetime $\tau = 5 \cdot 10^{-25}$ s [1]. Quark composites are called hadrons, the most common are mesons and baryons, but recently also tetraquarks and pentaquarks have been observed.

Mesons have baryon number $B = 0$ and are bosons, because with given spin of quarks $\frac{1}{2}$, their total spin is either 0 or 1. They are bound states of quark q and antiquark $\overline{q}$, where flavour of q and $\overline{q}$ can be different.

Baryons are bound states of three quarks. They are fermions (the total spin is an integer multiple of 1/2) and their baryon number is $B = 1$ ($B = -1$ for antibaryons). Observable world is primarily made of baryons with u and d quarks. The most common baryons are proton (uud) and neutron (udd), which form the nucleus of each atom.

[4] Masses of neutrino are estimated in the Table 1.1. According to precise cosmological measurement of Planck probe, the sum of neutrino masses is $\sum m_\nu < 0.23$ eV [13].

Tetraquarks and pentaquarks are new composite structures of quarks and antiquarks, which have been recently observed and cannot be classified either as mesons or baryons. In 2007, the observation of the $Z(4430)$ state, a $c\bar{c}d\bar{u}$ tetraquark candidate, was announced by the Belle experiment in Japan [19]. The observation of $Z(4430)$ was confirmed in 2014 by the LHCb experiment [20].
After this observation, it is not surprising, that also pentaquark state has been observed, namely the $J/\psi p$ resonance in $\Lambda_b^0 \to J/\psi K^- p$ decays [21]. The quark content of this pentaquark is expected to be $c\bar{c}uud$.
These new composite objects are not completely unexpected, since they have been discussed in the original Gell-Mann paper [15].

1.1.4 Antiparticles

Antiparticles are objects with the same mass as the corresponding particles, but they have opposite sign of electric and colour charge. Their existence was predicted originally in 1929 by Paul Dirac [22]. The first antiparticle (positron) was discovered in 1932 in a cloud chamber exposed to cosmic rays. Subsequently, other antiparticles have been discovered. Not all particles have its antipartner, for example, the boson Z^0 or γ are particles and their own antiparticles simultaneously. Using the fact that leptons behave as left-handed in the weak interactions (as noted in (1.10)), the anti-leptons behave as right-handed in the same type of interaction.

1.2 Symmetries

In physics, the system motion equations are determined by the Lagrangian of a given system. This Lagrangian is usually a function of several variables (like space position, angles, vector of momentum or angular momentum).

Property	**Symmetry**	**Conserved quantity**
homogeneity of time	time translation	energy
homogeneity of space	space translation	momentum
isotropy of space	space rotation	angular momentum

TABLE 1.3. Examples of the continuous symmetries and their conserved quantities.

Applying a transformation (e. g. Lorentz or Galilean transformation), Euler-Lagrange equations for a given Lagrangian can be the same as they have been before the transformation. In this case, the system is invariant under the transformation and for every symmetry of a Lagrangian there exists a conserved quantity called the constant of motion. Examples of symmetries and their conserved quantities are shown in the Table 1.3. In this table, only continuous symmetries are discussed, but also discrete symmetries exists, which are subject of the next section.

1.2.1 Discrete Symmetries

In quantum mechanics the state of a physical system is defined by a ray $|\psi\rangle$ in a Hilbert space. The time dependent system (its non-relativistic case) is fully described by the Schrödinger equation

$$\imath\hbar\frac{\partial}{\partial t}|\psi\rangle = \hat{\mathscr{H}}|\psi\rangle. \tag{1.12}$$

In this case, the Hamiltonian $\hat{\mathscr{H}}$ has a discrete spectrum of eigenvalues. Other examples of discrete spectra are squared angular momentum $\hat{L}^2$ with eigenvalues $\sqrt{l(l+1)}\hbar$ ($l \in \mathbb{N}$) and the third component of angular momentum $\hat{L}_z$ with eigenvalues $m\hbar$ ($m \in \mathbb{Z}$).
Special group of symmetries are represented by unitary or anti-unitary operators. The eigenvalues of these operators are 1 or -1. This group contains operators important in the next chapters of this work, such as the parity operator $\hat{P}$, charge conjugation operator $\hat{C}$ and time reversal operator $\hat{T}$.

1.2.1.1 The Parity

The parity or space inversion operation converts a right handed coordinate system to left handed ($x, y, z \to -x, -y, -z$)

$$\hat{P}\psi(\mathbf{r}) = \psi(-\mathbf{r}). \tag{1.13}$$

Moreover, it also inverts the direction of momentum, but it does not affect time and angular momentum. In two dimension, the inversion of axes is equivalent to the 180° rotation.
Applying twice the parity operator, the original state is obtained, which implies that the eigenvalues of the parity are ± 1.
Parity conservation implies that any physical process will happen identically when viewed in a mirror image.
The parity had seemed to be conserved in every physical process until 1956, when Wu observed an parity violation in ^{60}Co decay [23]. The cobalt nuclei were placed in the magnetic field and then their beta decays products ^{60}Ni, electron and one photon (from deexcitation of nickel) were detected. The parity would be conserved if the electron and

photons were found to be emitted in the same direction and electrons would have no preferred direction of decay relative to the nuclear spin. However, Wu observed electrons direction opposite to the direction of photons. So the most of the electrons preferred a specific direction of decay, opposite to that of the nuclear spin, so the parity has been violated.

1.2.1.2 The Charge Conjugation

The charge conjugation operator $\hat{C}$ changes the sign of the all quantum charges and does not affect the mass, linear momentum and spin of the particle. This implies that the operator $\hat{C}$ transform the particle into antiparticle,

$$\hat{C}\psi(\mathbf{r}) = \bar{\psi}(\mathbf{r}). \tag{1.14}$$

This operator is similarly to parity conserved in electromagnetic and strong interactions and violated in weak interactions. The charge conjugation is violated in the transformation of left-handed neutrino into the left-handed anti-neutrino, which was not observed[5].

1.2.1.3 The Time Reversal

The time reversal operator $\hat{T}$ changes the time direction,

$$\hat{T}\psi(r,t) = \psi(r,-t). \tag{1.15}$$

Since CP symmetry has been observed to be violated and CPT symmetry has not, the time reversal symmetry must also be violated. The first direct observation of the T-symmetry violation was made at CERN LEAR ring in 1998 [22].

1.2.1.4 CPT Invariance

The CPT theorem states that all interactions are invariant under the simultaneous application of the parity, charge conjugation and time reversal operators. Because the time reversal is violated, the combination of parity and charge conjugation is also expected to be violated (CP violation). This violation was firstly observed in the neutral kaon decay [24]. The CPT invariance in the observations of the high energy physics experiments is conserved [25–27].

[5]As discussed in the previous section, there exist only left-handed neutrino and right-handed anti-neutrino in the Standard Model using the Dirac description of neutrinos.

1.2.2 CP Violation

As discussed in section 1.2.1, the parity CP is violated. If CP were an exact symmetry, the laws of Nature would be the same for matter and for antimatter. We observe that most phenomena are C- and P-symmetric, and therefore, also CP-symmetric. In particular, these symmetries are respected by the gravitational, electromagnetic, and strong interactions and weak interaction. The situation changed in 1964, when Christenson, Cronin, Fitch and Turlay were studying eigenstates of two neutral K mesons in the kaon decays, labelled short-lived and long-lived kaons, K_S^0 and K_L^0. If CP is to be conserved, the final states can only be $K_S^0 \to 2\pi$ and $K_L^0 \to 3\pi$ and mass eigenstates are also CP eigenstates. As it was seen, K_L^0 also sometimes decays to 2 pions, which implies the CP eigenstates are different from the mass eigenstates and the K^0 and $\bar{K}^0$ can oscillate between each other, thus the CP symmetry is violated in certain rare processes.

There are three ways, how the CP symmetry can be violated in the Standard Model hadrons - CP violation in decay, in mixing and in the interference of mixing and decay.

The CP violation in decay (also known as direct CP violation) is the only possible source of CP asymmetry in charged meson decays. The decay amplitude Γ of the particle M into the final state f is different from the decay amplitude of its antiparticle into its final anti-state,

$$\Gamma(M \to f) \neq \Gamma\left(\bar{M} \to \bar{f}\right). \tag{1.16}$$

The CP violation in mixing (or indirect CP violation) arises when the probability of oscillation from meson to anti-meson is different from the probability of oscillation from anti-meson to meson,

$$\mathrm{Prob}\left(P^0 \to \bar{P}^0\right) \neq \mathrm{Prob}\left(\bar{P}^0 \to P^0\right). \tag{1.17}$$

Thus the mass eigenstates are not CP eigenstates.

The CP violation in interference of mixing and decay occurs in case both meson and antimeson decay into the same final state, $M^0 \to f$ and $M^0 \to \bar{M}^0 \to f$. This case occurs for example in the decay of $B_s^0 \to J/\psi\phi$.

1.3 The CKM Formalism

In 1963, Nicola Cabibbo [28] found, that the mass eigenstate and the interaction eigenstate of down and strange quark differ in the weak interaction. The charged current part of Lagrangian for weak interactions of quarks can be expressed as [29]:

$$\mathscr{L}_Y^q = -\frac{g}{\sqrt{2}} \bar{u_L}_i' \gamma^\mu \delta_{ij} \bar{d_L}_j' W_\mu^+ + h.c., \tag{1.18}$$

where u_L' and d_L' are quarks fields denote the interaction eigenvectors, γ^μ is Dirac matrix and W_μ^+ is a gauge field. Writing interaction eigenvectors in term of mass eigenvectors $d_L' = V_{dL}^\dagger d_L$ and $\bar{u}_L' = V_{uL} u_L$, the Lagrangian (1.18) is in the form

$$\mathscr{L}_Y^q = -\frac{g}{\sqrt{2}} \bar{u_L}_i \gamma^\mu \bar{V}_{ij} \bar{d_L}_j W_\mu^+ + h.c., \tag{1.19}$$

where $V_{ij} = V_{uL}^\dagger V_{dL}$ is the CKM matrix (Cabibbo-Kobayashi-Maskawa matrix), denoted as

$$V_{CKM} = \begin{pmatrix} V_{ud} & V_{us} & V_{ub} \\ V_{cd} & V_{cs} & V_{cb} \\ V_{td} & V_{ts} & V_{tb} \end{pmatrix}. \tag{1.20}$$

1.3.1 PDG and Wolfenstein Parametrisation

The matrix (1.20) is a complex 3×3 unitary matrix. Therefore, it has 18 parameters (9 complex elements), of which only four parameters are independent - 3 Euler mixing angles and one CP-violating CKM phase using the PDG parametrisation [1]. Defining $s_{ij} = \sin\theta_{ij}$, $c_{ij} = \cos\theta_{ij}$ and δ as the phase causing CP violation, the CKM matrix (1.20) can be written as multiple of three matrices

$$\begin{aligned} V_{CKM} &= \begin{pmatrix} 1 & 0 & 0 \\ 0 & c_{23} & s_{23} \\ 0 & -s_{23} & c_{23} \end{pmatrix} \begin{pmatrix} c_{13} & 0 & s_{13}e^{-\imath\delta} \\ 0 & 1 & 0 \\ -s_{13}e^{\imath\delta} & 0 & c_{13} \end{pmatrix} \begin{pmatrix} c_{12} & s_{12} & 0 \\ -s_{12} & c_{12} & 0 \\ 0 & 0 & 1 \end{pmatrix} = \\ &= \begin{pmatrix} c_{12}c_{13} & s_{12}c_{13} & s_{13}e^{-\imath\delta} \\ -s_{12}c_{23} - c_{12}s_{23}s_{13}e^{\imath\delta} & c_{12}c_{23} - s_{12}s_{23}s_{13}e^{\imath\delta} & s_{23}c_{13} \\ s_{12}s_{23} - c_{12}c_{23}s_{13}e^{\imath\delta} & -c_{12}s_{23} - s_{12}c_{23}s_{13}e^{\imath\delta} & c_{23}c_{13} \end{pmatrix}, \end{aligned} \tag{1.21}$$

each describing the two dimensional rotation. The angle θ_{12} is identified as the Cabibbo angle.

Based on the fact that $s_{13} \ll s_{23} \ll s_{12} \ll 1$, the CKM matrix in Wolfenstein parametrization [1] takes form

$$V_{CKM} = \begin{pmatrix} 1-\frac{1}{2}\lambda^2-\frac{1}{8}\lambda^4 & \lambda & A\lambda^3(\rho-\imath\eta) \\ -\lambda & 1-\frac{1}{2}\lambda^2-\frac{1}{8}\lambda^4\left(1+4A^2\right) & A\lambda^2 \\ A\lambda^3(1-\rho-\imath\eta) & -A\lambda^2+\frac{1}{2}A\lambda^4(1-2(\rho+\imath\eta)) & 1-\frac{1}{2}A^4\lambda^4 \end{pmatrix} + \mathcal{O}(\lambda^5), \tag{1.22}$$

with the parametrization

$$\begin{aligned} s_{12} &= \lambda, \\ s_{23} &= A\lambda^2, \\ s_{13}e^{\imath\delta} &= A\lambda^3(\rho+\imath\eta). \end{aligned} \tag{1.23}$$

The values from the experimental data [1] are:

$$\begin{aligned} \lambda =& 0.22506 \pm 0.00050, \\ A =& 0.811 \pm 0.026, \\ \bar{\rho} =& \rho\left(1-\frac{1}{2}\lambda\right) = 0.124^{+0.019}_{-0.018}, \\ \bar{\eta} =& \eta\left(1-\frac{1}{2}\lambda\right) = 0.356 \pm 0.011. \end{aligned} \tag{1.24}$$

From these results and parametrisation (1.22) of the CKM matrix (1.20), it is demonstrable that the diagonal elements are ~ 1, whereas the non-diagonal elements (which are responsible for the the quark generation change) are smaller than 1, specifically $|V_{us}|, |V_{cd}| \sim \lambda$, $|V_{cb}|, |V_{ts}| \sim \lambda^2$ and $|V_{ub}|, |V_{td}| \sim \lambda^3$. The imaginary part is larger for the $|V_{ub}| \sim \lambda^3$ and $|V_{td}|, |V_{ts}| \sim \lambda^4$.

1.3.2 Unitary Triangles

The unitarity condition of the CKM matrix can be manifestly demonstrated by noting that $V_{CKM}V^{\dagger}_{CKM} = 1$ is equivalent to the orthonormality of columns or rows in V_{CKM} expressed as

$$\sum_{\alpha=u,c,t} V_{\alpha i}V^*_{\alpha j} = \delta_{ij}, \sum_{i=d,s,b} V_{\alpha i}V^*_{\beta i} = \delta_{\alpha\beta}. \tag{1.25}$$

One of these unitarity triangles is

$$V_{ud}V^*_{ub} + V_{cd}V^*_{cb} + V_{td}V^*_{tb} = 0, \tag{1.26}$$

interpreted as triangle in the complex plane (see Figure 1.3).

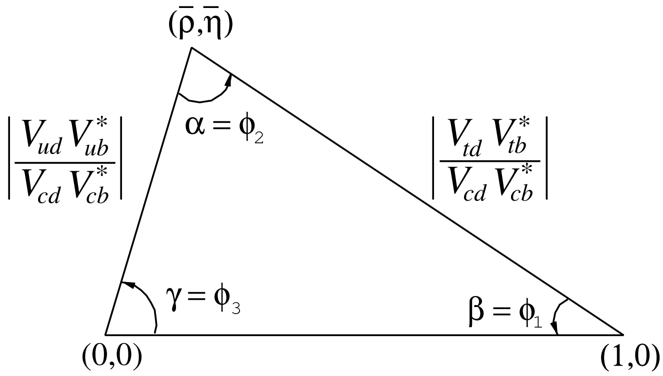

FIGURE 1.3. Unitarity triangle corresponding to the equation (1.26) [30].

This equation is often called B_d^0 triangle, because the angles α, β, γ from Fig. 1.3 are well measured in the B_d^0 decays. The B_s^0 triangle gives the relation

$$V_{us}V_{ub}^* + V_{cs}V_{cb}^* + V_{ts}V_{tb}^* = 0, \tag{1.27}$$

from which the small angle

$$\beta_s = \arg\left(-\frac{V_{ts}V_{tb}^*}{V_{cs}V_{cb}^*}\right) \tag{1.28}$$

can be obtained. This angle is sensitive to CP violation via the element V_{ts} (at $\mathcal{O}\left(\lambda^4\right)$). Both B_d^0 and B_s^0 triangles can be seen in Figure 1.4.

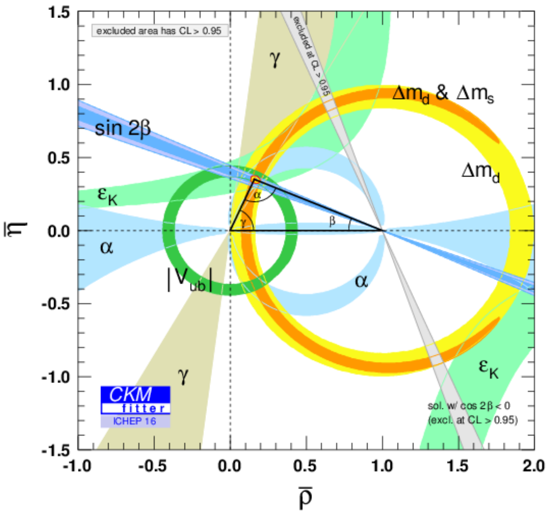

(a) B_d^0 triangle.

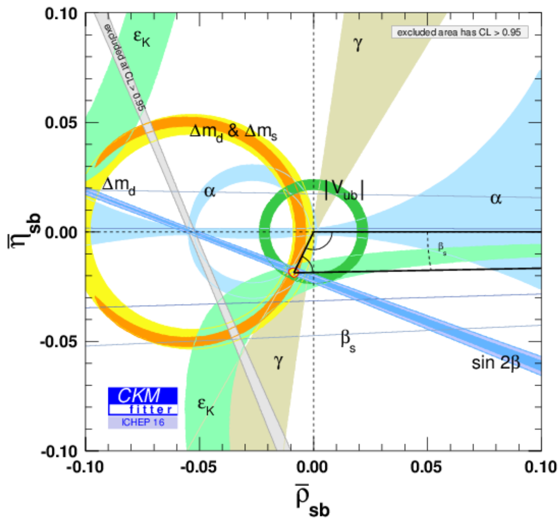

(b) B_s^0 triangle.

FIGURE 1.4. B_d^0 and B_s^0 (right) triangles from experimental results [31]. $\bar{\eta}$ and $\bar{\rho}$ are defined in equation (1.24).

Chapter 2

B physics

The first experimental evidence of the b quark has been observed in 1977 by Leon Lederman at Fermilab in proton beam collisions with the fixed target made of copper and platinum [32]. The Lederman's group observed resonance in the invariant $\mu^+\mu^-$ mass distribution around 9450 GeV and named this resonance Υ. It is a low-energy state of a meson composed of one b quark and one b anti-quark. This meson has also heavier resonances, all together forming a so called bottomonium state (bound state of the quark and anti-quark with same flavour, another example is charmonium $c\bar{c}$).

2.1 Production Mechanism of B Mesons at the LHC

At the LHC, B mesons are produced during the hadronization of b and $\overline{b}$ quarks. The b quark production is described within perturbative QCD calculations as an expansion in a series of the coupling constant α_s. Heavy flavour events can then be subdivided into three production classes, pair creation, flavour excitation and gluon splitting. The examples of each class are shown in Figure 2.1. The total bottom quark cross-section is shown in Figure 2.2.

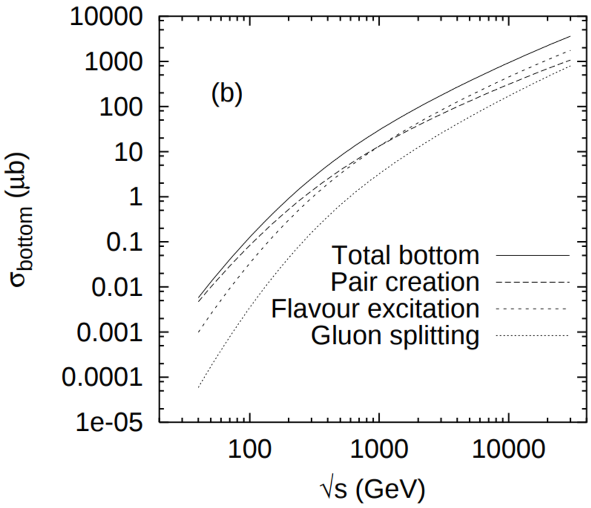

FIGURE 2.1. Bottom cross-section for the proton-proton collisions as the function of $E_{CM} = \sqrt{s}$. The contributions from pair creation, flavour excitation and gluon splitting are shown separately [33].

2.1.1 Pair Creation

It is represented by the $\mathcal{O}\left(\alpha_s^2\right)$ leading order (LO) process. This class of processes includes the $q\overline{q} \to b\overline{b}$ annihilation creating $b\overline{b}$ pair and the gluon-gluon QCD scattering $gg \to b\overline{b}$. Adding $\mathcal{O}\left(\alpha_s^3\right)$ next-to-leading order (NLO) perturbative processes provides the correction to higher order of perturbative expansion.

2.1.2 Flavour Excitation

In this NLO process, one gluon splits into $b\overline{b}$ pair. Then, one of these quarks together with the second gluon incoming to the reaction interchange a virtual gluon. The final state is the same as the NLO pair production has, but there is a requirement on the hard scattering to be more virtual than in the pair production [33].

2.1.3 Gluon Splitting

The gluon splitting is also by definition a NLO process, where the gluon splits into the quark anti-quark pair, $g \to b\overline{b}$, and no heavy flavour enters the hard scattering. When a gluon first branches into $b\overline{b}$ and the b later emits another gluon that is the one to enter the hard scattering, it can be considered as the flavour excitation. However, if no flavour enters the hard scattering, so this process is considered to be a gluon splitting process [33].

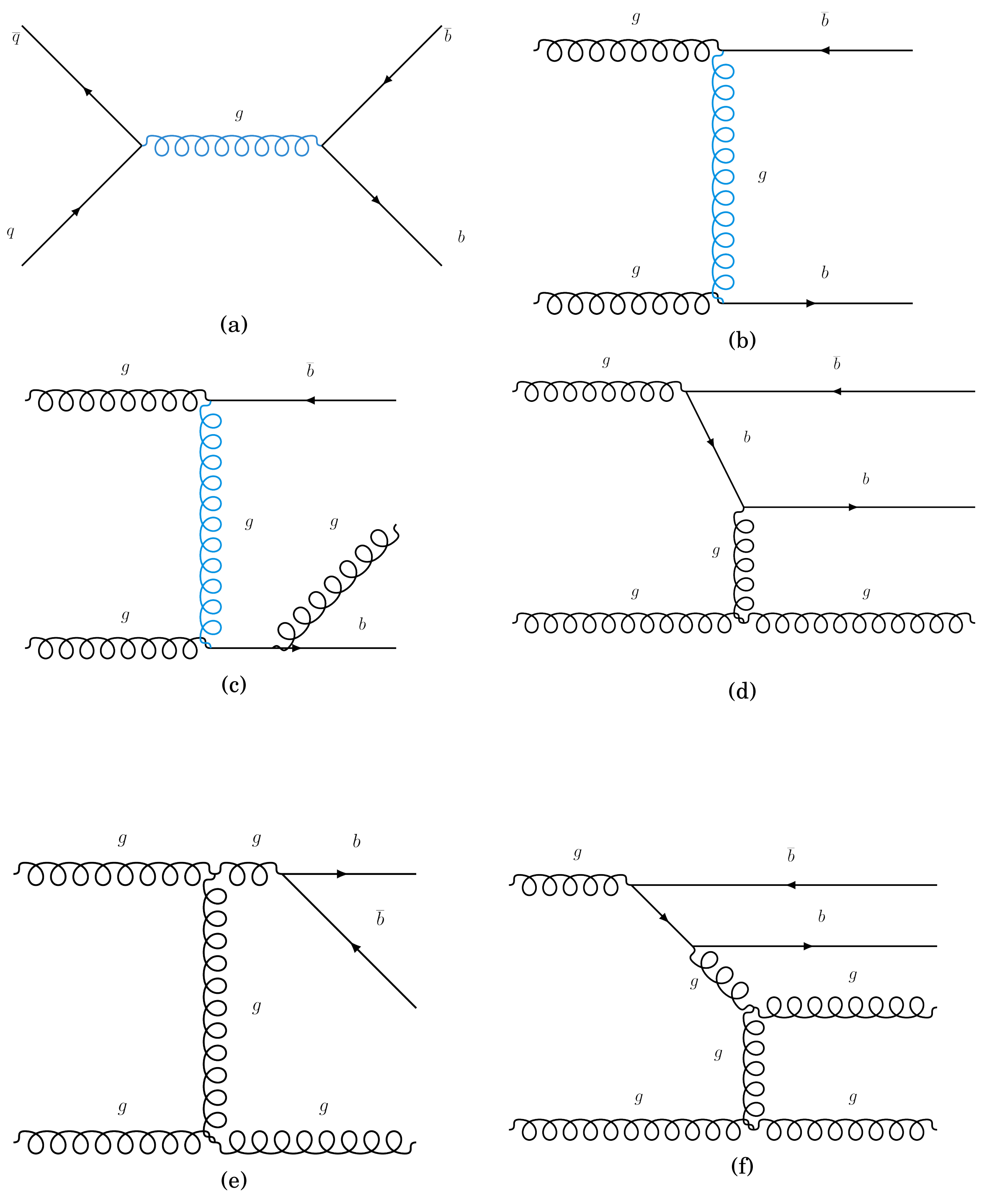

FIGURE 2.2. Examples of heavy-flavour production diagrams. (a,b) Leading order pair production. (c) Pair creation (with gluon emission). (d) Flavour excitation. (e) Gluon splitting. (f) Events classified as gluon splitting but of flavour-excitation character.

2.2 B Meson Properties

The B meson is a combination of $q\overline{q}$ with nonzero beauty quantum number B and it is sometimes called open-beauty meson. Usually, the bottomonium states (so-called hidden-beauty, the beauty quantum number $B = 0$) are not considered to be B mesons. The lowest mass B mesons are pseudoscalar particles, which can be charged or neutral. The summary of pseudoscalar B mesons in the ground state is shown in Table 2.1. Surprisingly, the B meson lifetime is larger than the lifetime of charmed mesons and their typical flight length before decaying is $c\tau \approx 0.5\,\mathrm{mm}$.

B mesons, due to their large mass, decay weakly. The dominant decay mode of the b

Name	Valence quark composition	Mass m [MeV]	Lifetime τ [ps]
$B^{\pm}$	$u\overline{b}$	5279.26 ± 0.17	1.519 ± 0.005
B^0_d	$d\overline{b}$	5279.58 ± 0.17	1.638 ± 0.004
B^0_s	$s\overline{b}$	5366.77 ± 0.24	1.512 ± 0.007
$B^{\pm}_c$	$c\overline{b}$	6275.6 ± 1.1	0.452 ± 0.033

TABLE 2.1. The lightest B mesons and their properties [1].

quark in a B meson is via $b \to c + W^-$ [1], where the W boson is virtual and subsequently decays into a pair of leptons or quarks. The $b \to u + \cdots$ transition is also allowed, however it is suppressed by the $|V_{ub}/V_{cb}|^2 \approx (0.1)^2$ relative to the $b \to c + \cdots$ [1]. Standard Model rare decays were also observed, such as is the decay $B^0_s \to \mu^+\mu^-$ [34].

The study of B mesons and their decays proved fruitful as it improved the understanding of hadronic processes. For example, semileptonic decays $B \to X_c l\nu$ and $B \to X_u l\nu$ are excellent tools to measure the magnitude of the CKM matrix elements V_{cb} and V_{ub}. Another example is the measurement of the CP violating phase $\phi_s = 2\beta_s$ from (1.28) in the mixing $B^0_s - \overline{B}^0_s$.

Besides CP violation, there are many other fields of study of B meson properties - for example measurement of the production cross-sections of beauty and charm hadrons and of the heavy flavour quarkonia. In this way, sensitive tests of QCD predictions of production in pp collisions could be provided.

2.3 $B_s - \overline{B}_s$ Mixing in $B^0_s \to J/\psi\phi$ Decay

Neutral B mesons have the ability to oscillate from particle into their own antiparticle and back. As referred in section 1.2.2 in chapter 1, since the flavour eigenstates are not equivalent to the mass eigenstates, the mixing is observed. The time evolution of the $B_s^0 - \overline{B}_s^0$ system can be described by the time dependent Schrödinger equation [29]

$$\imath\hbar\frac{\partial}{\partial t}\psi = \boldsymbol{H}\psi = \left(\boldsymbol{M} - \frac{\imath}{2}\boldsymbol{\Gamma}\right)\psi, \tag{2.1}$$

where ψ is the linear combination of B_s^0 and $\overline{B}_s^0$ wave functions, $\boldsymbol{M}$ is hermitian matrix providing mass terms and $\boldsymbol{\Gamma}$ is hermitian matrix describing the exponential decay

$$\boldsymbol{M} = \begin{pmatrix} M_{11} & M_{12} \\ M_{12}^* & M_{22} \end{pmatrix}, \boldsymbol{\Gamma} = \begin{pmatrix} \Gamma_{11} & \Gamma_{12} \\ \Gamma_{12}^* & \Gamma_{22} \end{pmatrix}. \tag{2.2}$$

Assuming the CPT symmetry is conserved, the diagonal terms $M_{11} = M_{22} = M$ and $\Gamma_{11} = \Gamma_{22} = \Gamma$ and the non-diagonal elements correspond to the $B_s^0 - \overline{B}_s^0$ mixing. If the CP symmetry is also conserved, the non-diagonal terms are equal, $M_{12} = M_{12}^*$ and $\Gamma_{12} = \Gamma_{12}^*$. The Schrödinger equation (2.1) can be solved by the diagonalization of the matrix $\boldsymbol{H}$. The solution are two mass eigenstates with defined decay widths. These eigenstates are defined as B_H and B_L for the light and heavy state respectively,

$$\begin{aligned} |B_L\rangle &= p\,|B_s^0\rangle + q\,|\overline{B}_s^0\rangle \text{ and} \\ |B_H\rangle &= p\,|B_s^0\rangle - q\,|\overline{B}_s^0\rangle \end{aligned} \tag{2.3}$$

with complex coefficients p, q satisfying the normalisation condition $|p|^2 + |q|^2 = 1$. Using the mass and lifetime of the eigenstates $|B_L\rangle$ and $|B_H\rangle$, the difference in mass and lifetime of the eigenvalues can be expressed as

$$\begin{aligned} \Delta m_s &= m_H - m_L, \\ \Delta\Gamma_s &= \Gamma_L - \Gamma_H. \end{aligned} \tag{2.4}$$

By definition Δm_s is positive, but $\Delta\Gamma_s$ can be negative. The Δm_s impacts the mixing frequency of the $B_s^0 - \overline{B}_s^0$ oscillation.

Using equations (2.3) and (2.1), the mass eigenstates have a simple exponential evolution in proper time t,

$$\begin{aligned} |B_L(t)\rangle &= \exp\left(-\imath(M_L - \frac{\imath}{2}\Gamma_L)t\right)|B_L(0)\rangle\,, \\ |B_H(t)\rangle &= \exp\left(-\imath(M_H - \frac{\imath}{2}\Gamma_H)t\right)|B_H(0)\rangle\,. \end{aligned} \tag{2.5}$$

The time evolution of flavour state B_s^0 and $\overline{B}_s^0$ can be obtained using this equation and (2.3):

$$\begin{aligned} |B_s^0(t)\rangle &= g_+(t)\,|B_s^0(0)\rangle - \frac{q}{p}g_-(t)\,|\overline{B}_s^0(0)\rangle \text{ and} \\ |\overline{B}_s^0(t)\rangle &= g_+(t)\,|\overline{B}_s^0(0)\rangle - \frac{p}{q}g_-(t)\,|B_s^0(0)\rangle\,, \end{aligned} \tag{2.6}$$

where

$$g_{\pm}(t) = \frac{1}{2}e^{-\imath M_s t - \Gamma t/2}\left[\cosh(\frac{\Delta\Gamma_s}{2}t) \pm \cos(\Delta M_s t)\right]. \tag{2.7}$$

For simplification, the decay amplitudes at $t = 0$ can be denoted as

$$\begin{aligned} A_f &= \langle f|\boldsymbol{H}|B_s^0(0)\rangle \qquad \bar{A}_f = \langle f|\boldsymbol{H}|\overline{B}_s^0(0)\rangle \\ A_{\bar{f}} &= \langle\overline{f}|\boldsymbol{H}|B_s^0(0)\rangle \qquad \bar{A}_{\bar{f}} = \langle\bar{f}|\boldsymbol{H}|\overline{B}_s^0(0)\rangle. \end{aligned} \tag{2.8}$$

The differential decay rate is calculated by taking the modulus squared of the amplitudes (2.8). The branching ratio (decay rate) for $B_s^0 \to f$ can be expressed as [35]

$$\begin{aligned} \Gamma\left(B_s^0(t) \to f\right) =& e^{\Gamma t}\left[\left(|A_f|^2 + |\frac{q}{p}\bar{A}_f|^2\right)\cosh\frac{\Delta\Gamma_s t}{2} + \left(|A_f|^2 - |\frac{q}{p}\bar{A}_f|^2\right)\cos\Delta M t\right. \\ &\left. + 2\mathscr{R}e\left(\frac{q}{p}A_f^*\bar{A}_f\right)\sinh\frac{\Delta\Gamma_s t}{2} - 2\mathscr{I}m\left(\frac{q}{p}A_f^*\bar{A}_f\right)\sin\Delta M t\right]. \end{aligned} \tag{2.9}$$

The branching ratio for $\bar{B}_s^0$ looks similar:

$$\begin{aligned} \Gamma\left(\bar{B}_s^0(t) \to f\right) =& e^{\Gamma t}\left[\left(|A_f|^2 + |\frac{q}{p}\bar{A}_f|^2\right)\cosh\frac{\Delta\Gamma_s t}{2} - \left(|A_f|^2 - |\frac{q}{p}\bar{A}_f|^2\right)\cos\Delta M t\right. \\ &\left. + 2\mathscr{R}e\left(\frac{q}{p}A_f^*\bar{A}_f\right)\sinh\frac{\Delta\Gamma_s t}{2} - 2\mathscr{I}m\left(\frac{q}{p}A_f^*\bar{A}_f\right)\sin\Delta M t\right]. \end{aligned} \tag{2.10}$$

This theoretical $B_s^0 \to J/\psi\phi$ decay rate then can be expressed differentially as a function of time and three transversity angles Ω defined in Figure 2.3. The branching ratios (2.9) and (2.10) can be decomposed into these three transversity angles or in three complex polarisation amplitudes, $A_0(t)$, $A_\perp(t)$, $A_\parallel(t)$, that describe the different polarisation states of the $J/\psi(\mu\mu)\phi(KK)$ system. At the time $t = 0$, the longitudinally polarized amplitude $A_0 = A_0(t = 0)$ is CP-even and the two transversely polarised amplitudes $A_\perp = A_\perp(t = 0)$ and $A_\parallel = A_\parallel(t = 0)$ are CP-odd.

Using the polarisation amplitude and the transversity notation, the differential decay rate can be written in the form:

$$\frac{d^4\Gamma}{dt d\Omega} = \sum_{k=1}^{6}\mathscr{O}^k(t)g^k(\theta_T, \psi_T, \phi_T), \tag{2.11}$$

where $\mathscr{O}^k$ describe the time evolution of the angular distribution $g^k(\theta_T, \psi_T, \phi_T)$ (θ_T, ψ_T, ϕ_T are defined in Figure 2.3) and it can be expressed in terms of real or imaginary parts of bilinear combinations of decay amplitudes. Including some additional terms (S-wave contribution and its interference with (2.11)), the equation (2.11) is extended into [37]:

$$\frac{d^4\Gamma}{dt d\Omega} = \sum_{k=1}^{10}\mathscr{O}^k(t)g^k(\theta_T, \psi_T, \phi_T), \tag{2.12}$$

where $\mathcal{O}^k(t)$ are the time-dependent functions corresponding to the contributions of the four amplitudes A_0, $A_\parallel$, $A_\perp$, and A_S and their interference terms and $g^k(\theta_T, \psi_T, \phi_T)$ are the functions of the transversity angles ϕ_T, ψ_T, θ_T, see Table 2.2. This equation is valid for both B_s^0 and $\overline{B}_s^0$ decay rate, the sign reverses in the terms containing Δm_s.
The equation (2.12) is expressed for the tagged events. If no tagging information is available (untagged event), all terms with Δm_s are cancelled out. As the terms with Δm_s in Table 2.2 also contain $\cos\phi_s$ or $\sin\phi_s$, tagged events provide higher sensitivity to the measurement of ϕ_s.

2.3.1 Flavour Tagging

As discussed earlier, B mesons are produced in pairs (in QCD), so the initial flavour of a neutral B-meson can be determined by the species identification of the second hadron containing the second b quark. This can be done by a variety of complex methods summarily called flavour tagging. These methods can be divided into two categories: same side flavour tagging and opposite side tagging.
Same side tagging algorithm uses information that comes with B_s^0,which contains the $\overline{b}$ quark and also s quark. This s quark was created together with its antiparticle $\overline{s}$ in the $p-p$ collision and this $\overline{s}$ forms meson or baryon during the hadronization. So in case of

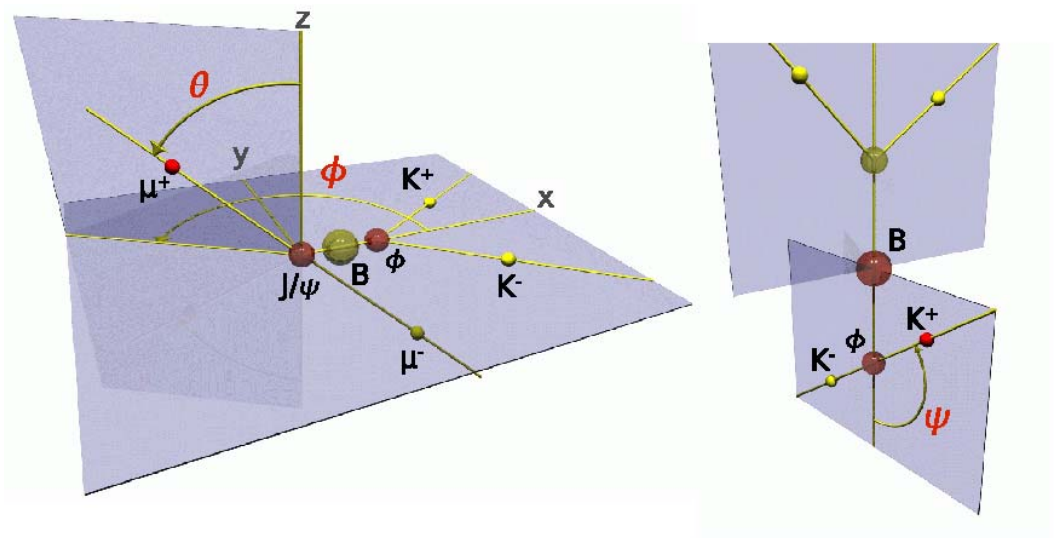

FIGURE 2.3. The description of the decay angles. On the left θ and ϕ defined in the $J/\psi(\mu\mu)$ rest frame and on the right ψ defined in the $\phi(KK)$ rest frame [36].

k	$\mathcal{O}^k(t)$	$g^k(\theta_T,\psi_T,\phi_T)$
1	$\frac{1}{2}\lvert A_0\rvert^2\left[(1+\cos\phi_s)e^{-\Gamma_L t}+(1-\cos\phi_s)e^{-\Gamma_H t}\pm 2e^{-\Gamma_s t}\sin(\Delta m_s t)\sin\phi_s\right]$	$2\cos^2\psi_T(1-\sin^2\theta_T\cos^2\phi_T)$
2	$\frac{1}{2}\lvert A_\parallel\rvert^2\left[(1+\cos\phi_s)e^{-\Gamma_L t}+(1-\cos\phi_s)e^{-\Gamma_H t}\pm 2e^{-\Gamma_s t}\sin(\Delta m_s t)\sin\phi_s\right]$	$\sin^2\psi_T(1-\sin^2\theta_T\sin^2\phi_T)$
3	$\frac{1}{2}\lvert A_\perp\rvert^2\left[(1-\cos\phi_s)e^{-\Gamma_L t}+(1+\cos\phi_s)e^{-\Gamma_H t}\mp 2e^{-\Gamma_s t}\sin(\Delta m_s t)\sin\phi_s\right]$	$\sin^2\theta_T\sin^2\psi_T$
4	$\frac{1}{2}\lvert A_\parallel\rvert\lvert A_0\rvert\cos\delta_\parallel\left[(1+\cos\phi_s)e^{-\Gamma_L t}+(1-\cos\phi_s)e^{-\Gamma_H t}\pm 2e^{-\Gamma_s t}\sin(\Delta m_s t)\sin\phi_s\right]$	$\frac{1}{\sqrt{2}}\sin 2\psi_T\sin^2\theta_T\sin\phi_T$
5	$\lvert A_\parallel\rvert\lvert A_\perp\rvert\left[\frac{1}{2}\left(e^{-\Gamma_L t}-e^{-\Gamma_H t}\right)\cos(\delta_\perp-\delta_\parallel)\sin\phi_s \pm e^{-\Gamma_s t}\left(\sin(\delta_\perp-\delta_\parallel)\cos\Delta m_s t-\cos(\delta_\perp-\delta\parallel)\cos\phi_s\sin\Delta m_s t\right)\right]$	$-\sin^2\psi_T\sin 2\theta_T\sin\phi_T$
6	$\lvert A_0\rvert\lvert A_\perp\rvert\left[\frac{1}{2}\left(e^{-\Gamma_L t}-e^{-\Gamma_H t}\right)\cos\delta_\perp\sin\phi_s \pm e^{-\Gamma_s t}\left(\sin\delta_\perp\cos\Delta m_s t-\cos\delta_\perp\cos\phi_s\sin\Delta m_s t\right)\right]$	$\frac{1}{\sqrt{2}}\sin 2\psi_T\sin 2\theta_T\cos\phi_T$
7	$\frac{1}{2}\lvert A_S\rvert^2\left[(1-\cos\phi_s)e^{-\Gamma_L t}+(1+\cos\phi_s)e^{-\Gamma_H t}\mp 2e^{-\Gamma_s t}\sin\Delta m_s t\sin\phi_s\right]$	$\frac{2}{3}\left(1-\sin^2\theta_T\cos^2\phi_T\right)$
8	$\lvert A_S\rvert\lvert A_\parallel\rvert\left[\frac{1}{2}\left(e^{-\Gamma_L t}-e^{-\Gamma_H t}\right)\sin(\delta_\parallel-\delta_S)\sin\phi_s \pm e^{-\Gamma_s t}\left(\cos(\delta_\parallel-\delta_S)\cos\Delta m_s t-\sin(\delta_\parallel-\delta_S)\cos\phi_s\sin\Delta m_s t\right)\right]$	$\frac{\sqrt{6}}{3}\sin\psi_T\sin^2\theta_T\sin 2\phi_T$
9	$\frac{1}{2}\lvert A_\perp\rvert\lvert A_S\rvert\sin(\delta_\perp-\delta_S)\left[(1-\cos\phi_s)e^{-\Gamma_L t}+(1+\cos\phi_s)e^{-\Gamma_H t}\mp 2e^{-\Gamma_s t}\sin(\Delta m_s t)\sin\phi_s\right]$	$\frac{\sqrt{6}}{3}\sin\psi_T\sin 2\theta_T\cos\phi_T$
10	$\lvert A_0\rvert\lvert A_S\rvert\left[\frac{1}{2}\left(e^{-\Gamma_H t}-e^{-\Gamma_L t}\right)\sin\delta_S\sin\phi_s\pm e^{-\Gamma_s t}\left(\cos\delta_S\cos\Delta m_s t-\sin\delta_S\cos\phi_s\sin\Delta m_s t\right)\right]$	$\frac{4\sqrt{3}}{3}\cos\psi_T\left(1-\sin^2\theta_T\cos^2\phi_T\right)$

TABLE 2.2. Table showing the ten time-dependent functions $\mathcal{O}^k(t)$ and the functions of the transversity angles $g^k(\theta_T,\psi_T,\phi_T)$ [37].

detecting the K^+ meson pointing to the same vertex[1], we can then distinguish whether B_s^0 or $\overline{B}_s^0$ was in the initial state.

The opposite side flavour tagging uses the fact, that the b quark is created together with the $\overline{b}$ in the B_s^0. This b quark also forms a hadron. b quark can decay into charged particles (muons, electrons, jets, ...) by semi-leptonic b-hadron decays or by chained $b \to c \to s$ decay. These two decays are competitive, because oppositely charged particle are created in these two types of decays, but the semi-leptonic is more probable, so the composition of the opposite side B meson and also signal B meson can be estimated.

Because of only daughter particles are detected, both methods are just estimation and only the probability of tagging can be used in the fit of the decay rate (2.12). In order to improve the tagging estimation, the decay of charged B meson can be used, because the charge is known by detecting the mesons daughter particle. The calibration channel used in this diploma thesis is $B^\pm \to J/\psi K^\pm$, where the charge of B meson is known and the opposite side is used for the identification when decaying into jets, muon or electron. The probability of correctly determined opposite charge is obtained and it is used as the calibration for flavour tagging in the $B_s^0 \to J/\psi\phi$ decays.

2.3.2 Previous Measurements

The measurement of the CP violation phase ϕ_s in the decay $B_s^0 \to J/\psi\phi$ has been and is being carried out by several large experiments, of which the most important results are coming from LHCb, ATLAS and CMS at the LHC and D0 at Tevatron. Some of these detectors are optimized for B physics, so the results are considered precise. In performed analyses, these experimental collaborations employ information from the same side tagging (checking the charge and flavour composition of meson that comes from the same vertex as B_s^0) to improve the measurement.

2.3.2.1 D0

D0 is the detector that has been operating at the $p\bar{p}$ Tevatron collider. In the published measurement result, the data sample corresponds to an integrated luminosity of 8.0 fb^{-1} accumulated with the D0 detector using $p\bar{p}$ collisions at $\sqrt{s}$ = 1.96 TeV [38]. The oscillation frequency has been constrained to $\Delta m_s = (17.77 \pm 0.12)$ ps^{-1}. Including the systematic uncertainties, the phase ϕ_s and decay width difference are

$$\Delta\Gamma_s = 0.163^{+0.065}_{-0.064}\,\mathrm{ps}^{-1} \qquad \phi_s = -0.55^{+0.38}_{-0.36}. \tag{2.13}$$

[1]Point in the space, where particles decay and produce daughter particle.

The 68%, 90% and 95% CL contours in the $\phi_s - \Delta\Gamma_s$ plane are in Figure 2.4.

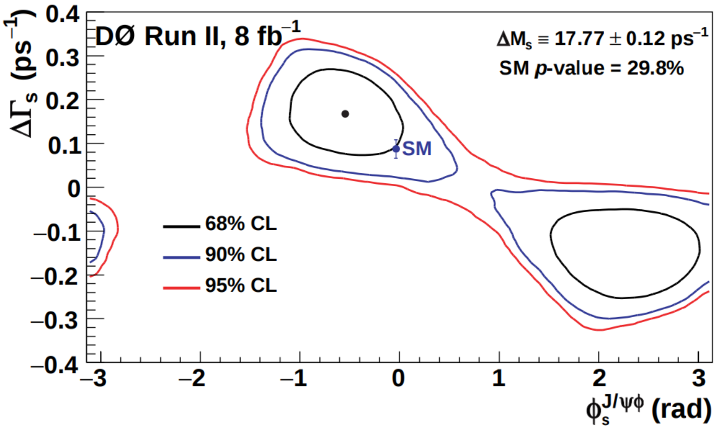

FIGURE 2.4. Likelihood confidence regions including systematic uncertainties measured at D0. The Standard Model expectation is indicated as a point with an error [38].

2.3.2.2 LHCb

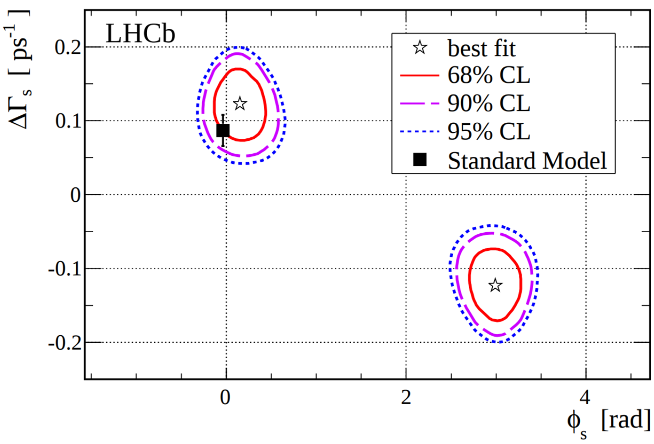

FIGURE 2.5. Likelihood confidence regions including systematic uncertainties measured at LHCb. The Standard Model expectation is indicated as a point with an associated error contour [39].

The LHCb is the detector built exclusively for study of B physics processes. A sample of about 8500 $B_s^0 \to J/\psi\phi$ events isolated from 0.37 fb^{-1} of pp collisions at $\sqrt{s} = 7$ TeV was used in [39]. Due to the high fraction of tagged events in the signal sample $\epsilon = (24.9 \pm 0.5)\%$, an effective tagging efficiency is $TP = (1.91 \pm 0.23)\%$, so the tagging has large impact on the analysis precision. The decay width difference $\Delta\Gamma_s$, the average decay width Γ_s and the phase ϕ_s are

$$
\begin{aligned}
\Gamma_s &= (0.657 \pm 0.009 \pm 0.008)\,\text{ps}^{-1} \\
\Delta\Gamma_s &= (0.125 \pm 0.029 \pm 0.01)\,\text{ps}^{-1} \\
\phi_s &= (0.15 \pm 0.18 \pm 0.06)
\end{aligned}
\tag{2.14}
$$

and the 68%, 90% and 95% CL contours in the $\phi_s - \Delta\Gamma_s$ plane are shown in Figure 2.5.

2.3.2.3 ATLAS

ATLAS is a general-purpose detector. It has been primarily built to study the high p_{T} particle physics beyond the Standard Model (ATLAS was built to study and discover the basic block of matter, to investigate properties of the previously undiscovered Higgs boson). pp collisions data recorded at ATLAS can be also used for successfully study of the CP violation in $B_s^0 - \bar{B}_s^0$ mixing. ATLAS B physics group measured the B_s^0 decay parameters using an integrated luminosity of 14.3 fb^{-1} collected by the ATLAS detector at $\sqrt{s} = 8$ TeV pp collisions at the LHC and combined them with earlier data using integrated luminosity of 4.9 fb^{-1} and c.m.s. energy of $\sqrt{s} = 7$ TeV [37]. The opposite side tagging was used as well at the LHCb experiment. However, the effective tagging efficiency of muon is smaller, $TP = (1.49 \pm 0.02)\%$. Using results of the full simultaneous unbinned maximum-likelihood fit of data at $\sqrt{s} = 8$ TeV and combining them with data at $\sqrt{s} = 7$ TeV, the decay width difference $\Delta\Gamma_s$, the average decay width Γ_s and the phase ϕ_s are

$$
\begin{aligned}
\Gamma_s &= (0.675 \pm 0.003 \pm 0.003)\,\text{ps}^{-1} \\
\Delta\Gamma_s &= (0.085 \pm 0.011 \pm 0.007)\,\text{ps}^{-1} \\
\phi_s &= (-0.090 \pm 0.078 \pm 0.041)
\end{aligned}
\tag{2.15}
$$

and the 68% and 95% CL contours in the $\phi_s - \Delta\Gamma_s$ plane are shown in Figure 2.6.

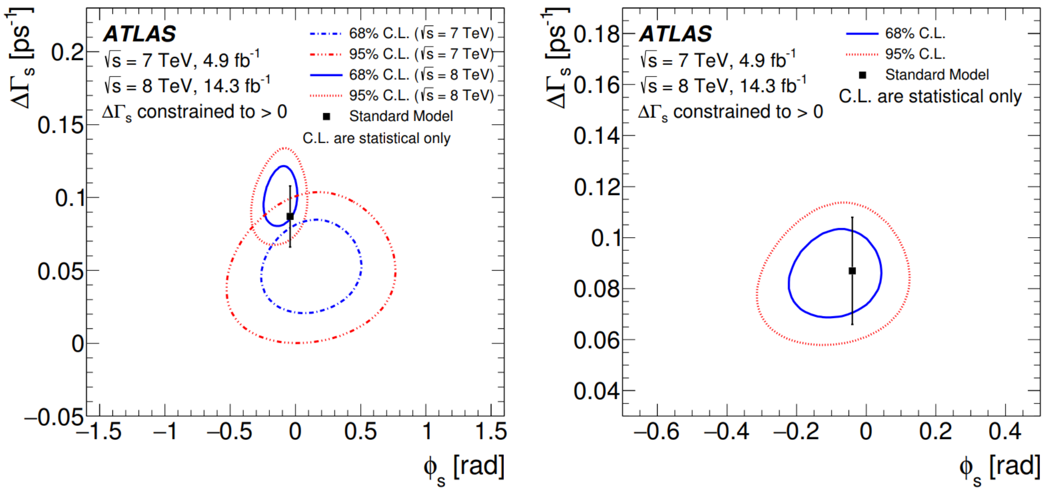

FIGURE 2.6. Likelihood contours in the $\phi_s - \Delta\Gamma_s$ plane for individual results from 7 TeV and 8 TeV data (left) and a final statistical combination of the results from 7 TeV and 8 TeV data (right). The Standard Model expectation is indicated as the point with an error [37].

CHAPTER 3

THE ATLAS DETECTOR AT THE LHC

To study and test the predictions of the Standard Model and discover the physics beyond its boundaries, particle accelerators and corresponding detectors are systematically used as exploration tools. In these apparatuses, charged particles are accelerated to nearly the speed of light by the electromagnetic fields, then collided at interaction points, where particle detectors are placed and secondary particles are studied. The best known colliders are the Large Hadron Collider (LHC) at CERN[1], Relativistic Heavy Ion Collider (RHIC) at Brookhaven National Laboratory and Tevatron at Fermilab. All these colliders are circular synchrotron accelerators. The Stanford Linear Accelerator Center (SLAC) represents the other type of accelerator, the linear accelerator, which is suitable for accelerating and colliding light electrons which would otherwise suffer from synchrotron radiation losses in a circular accelerator.

3.1 The Large Hadron Collider

3.1.1 History of the LHC

The Large Hadron Collider is the most powerful particle collider ever built. It is located in an underground 27 kilometres in circumference at the France–Switzerland border near Geneva, Switzerland. The first proposal of the Large Hadron Collider was presented

[1]European Organization for Nuclear Research (in French: Conseil Européen en pour la Recherche Nucleaire), www.cern.ch.

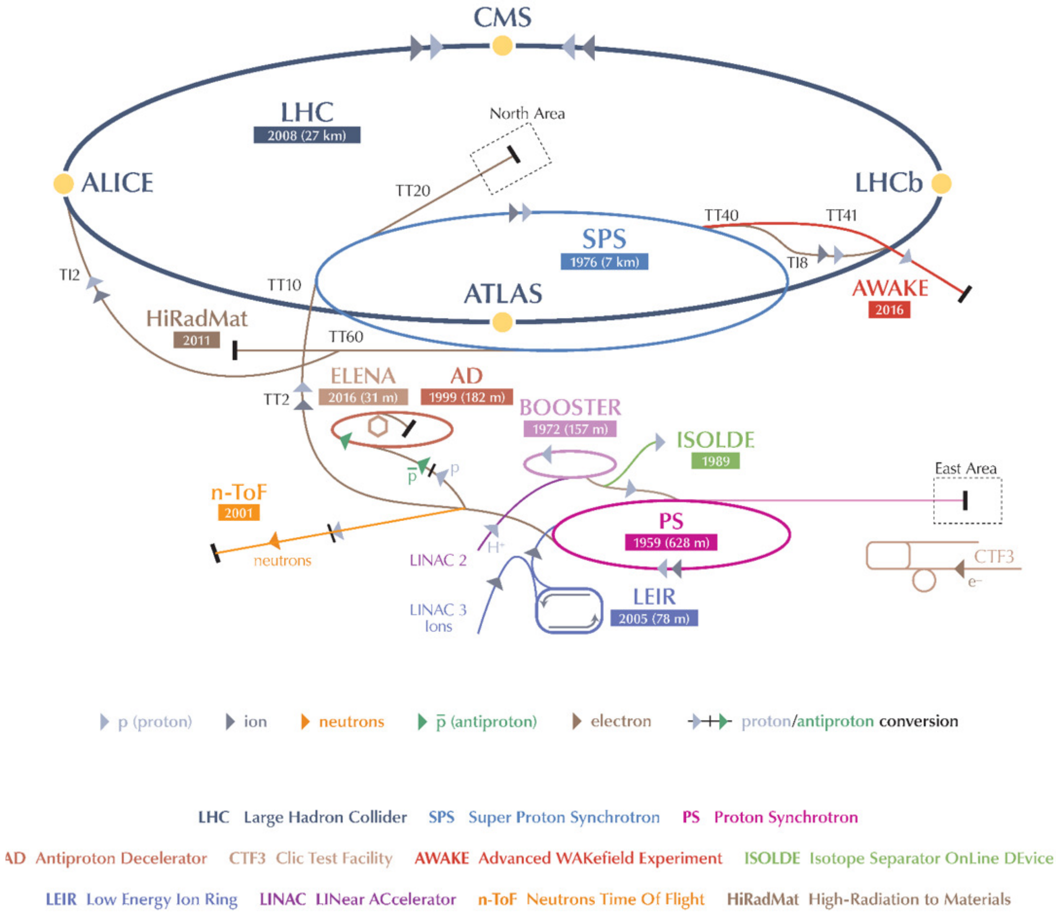

FIGURE 3.1. The CERN accelerator complex. The proton chain starts in the LINAC 2, the ^{208}Pb chain starts in LINAC 3. The nuclei then travel through the BOOSTER (LEIR for ^{208}Pb), PS, SPS and are collided in the LHC main ring. The accelerating sequence is described in section 3.1.2 [40].

in 1984 on the CERN and ECFA[2] workshop in Lausanne, Switzerland. In this proposal, the excavated tunnel for Large Electron-Positron collider (LEP) at CERN would be later used for the LHC. The excavation of this tunnel was completed in 1988 and the LEP collider started operation in August 1989 with the total beam energy of 45 GeV for accelerated electrons and positrons. These particles were preaccelerated and injected in to the main LEP ring by the Super Proton Synchrotron (SpS), the older accelerator and collider used previously as independent accelerator of protons (later protons and antiprotons, Sp$\bar{\text{p}}$S) between 1981 and 1984. During the LEP era, it was included into the LEP (later LHC) accelerator chain. The LEP center of mass energy reached its maximum

[2]European Committee for Future Accelerators, ecfa.web.cern.ch.

of 209 GeV in 2000 and at the end of the year, the LEP Collider was shut down due to the construction of the LHC.

The CERN council approved the construction of the Large Hadron Collider in 1994 and the design report of the LHC was published in 1995. The ATLAS, CMS and ALICE experiments were approved in 1997, the LHCb experiment a year later. After years of construction, the LHC operation was started on September 10$^{\text{th}}$ 2008, but nine days later, a fault forcing a shutdown occured in the electrical bus connection and the helium from the cooling system was released. The LHC was restarted in November 2009. A month later, LHC was operated with the collisions energy of 2.36 TeV, which set the new world record. After a short technical stop, the LHC was started again with the physics programme and the first collisions at 7 TeV centre-of-mass energy until 2011. Then in 2012, the collision energy was increased to 8 TeV. In this period (2010-2012), denoted as LHC Run 1, among the most important discoveries were the Higgs boson[2], the bottomium state $\chi_b(3P)$ [41] and also observation of a rare decay of B_s meson into two muons andits compatibility with Standard Model predictions. The Run 1 ended in winter 2012, followed by the shutdown LS1.

After shutdown for hardware upgrade, Run 2 started in June 2015 at a record collision energy 13 TeV. This period will last for three years and the second shutdown will follow. The preliminary LHC schedule to year 2037 is shown in Figure 3.2.

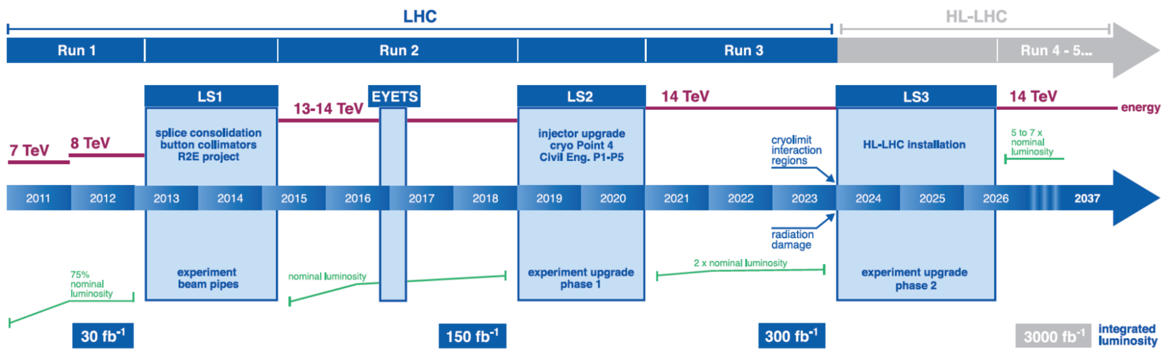

FIGURE 3.2. The outline LHC schedule out to 2037 with the LS shutdowns and Extended Year End Technical Stop (EYETS)[42].

3.1.2 The LHC Accelerator

The main accelerator ring lies in a tunnel 27 kilometres in circumference. It contains two adjacent parallel beam pipes. 1232 dipole magnets located around these pipes are used to bend the beam and 392 quadrupole magnets focus the beam. Another type of magnet is used to focus the beam closer together in order to increase the chance of collision. The operating temperature of magnets is 1.9 K, so the cooling system is filled with the superfluid ^{4}He.

The LHC can accelerate and collide several types of particles - protons (majority of the year), nuclei of lead (last month of operating time of the year, at the centre-of-mass energy 5.02 TeV) or xenon (12 October 2017, Xe-Xe collisions at a centre-of-mass energy of 5.44 TeV per colliding nucleon pair).

Hydrogen is used as a source of protons. These protons are sent into the linear accelerator Linac2, where they are accelerated to energy of 50 MeV. Thereafter, the beam continues to the Proton Synchrotron Booster (PSB), that pushes the beam energy to 1.4 GeV. Going through the Proton Synchrotron (PS), which accelerates protons to 25 GeV, they reach the Super Proton Synchrotron, where they are accelerated to 450 GeV. Finally, the protons are injected into the two LHC beam pipes,where are accelerated to the beam energy (6.5 TeV per beam during Run 2), one beam circulates clockwise and the the other beam circulates counterclockwise. It takes 4 minutes and 20 seconds to fill the LHC ring. After the final acceleration, proton bunches are collided with the frequency of 40 MHz (which corresponds to the time distance between bunches of 25 ns). The whole accelerator chain is shown in Figure 3.1.

Not all protons in bunches are collided at the end of LHC fill. The protons in bunches have large kinetic energy and therefore high destructive power, so they are sent to the beam dump, where they are safely disposed of. The beam dump has blocks several meters long made of copper, aluminium, carbon and beryllium.

In the LHC, besides protons also ^{208}Pb nuclei are accelerated and collided. They start their journey at the linear accelerator Linac3 and after accumulation in the LEIR storage ring, they are injected into the PS. Then, the acceleration process is the same as for protons [43].

3.1.3 Detectors at the LHC

The beams in both pipes are collided at four locations around the accelerator ring. At these places, four large experiments (with their own interaction point) and three small ones (they share the collision point with one of the large detector) are build.

ATLAS **A T**oroidal **L**HC **A**pparatu**S** is a multi-purpose detector. It is built to study the particle physics beyond the Standard Model. ATLAS was built to discover the basic block of matter, to investigate properties of the previously undiscovered Higgs boson or the asymmetry between the behavior of matter and antimatter, known as the CP violation [44].

CMS The **C**ompact **M**uon **S**olenoid was built with similar purpose as ATLAS. The main goals of this experiment are the same as the goals of ATLAS, but CMS and ATLAS use different technical solutions and design of their detector magnet system [44].

ALICE **A L**arge **I**on **C**ollider **E**xperiment is a detector built primary to detect particles originating in the heavy ion collisions. At these collisions, the temperature much higher than inside the Sun is reached and also the signs of the quark gluon plasma state[3] (QGP) is possibly observed [44].

LHCb **L**arge **H**adron **C**ollider **b**eauty is designed to study the difference between matter and antimatter by studying the properties of mesons and baryons witch contains the b quark. LHCb is also capable to perform measurements of electroweak physics in the forward region [44].

LHCf **L**arge **H**adron **C**ollider **f**orward is an experiment intended for studying astroparticle (cosmic ray) physics. It is built at the same collision point as ATLAS. It uses particles thrown in the forward direction by collisions as a source to simulate cosmic rays [44].

TOTEM The full name of this experiment is **TOT**al cross section, **E**lastic scattering and diffraction dissociation **M**easurement at the LHC. It shares the collision point with the CMS. The detector aims at the measurement of total cross section and elastic scattering in forward region [44].

MoEDAL The **Mo**nopole and **E**xotics **D**etector **a**t the **L**HC is located near the LHCb experiment. The main goal of this detector is the search of the magnetic monopole, a hypothetical particle with a magnetic charge. MOEDAL also looks for highly ionizing Stable Massive Particles (SMPs), predicted by theories beyond the Standard Model [44].

[3]The state few milliseconds after the Big Bang, where quarks and gluons are free.

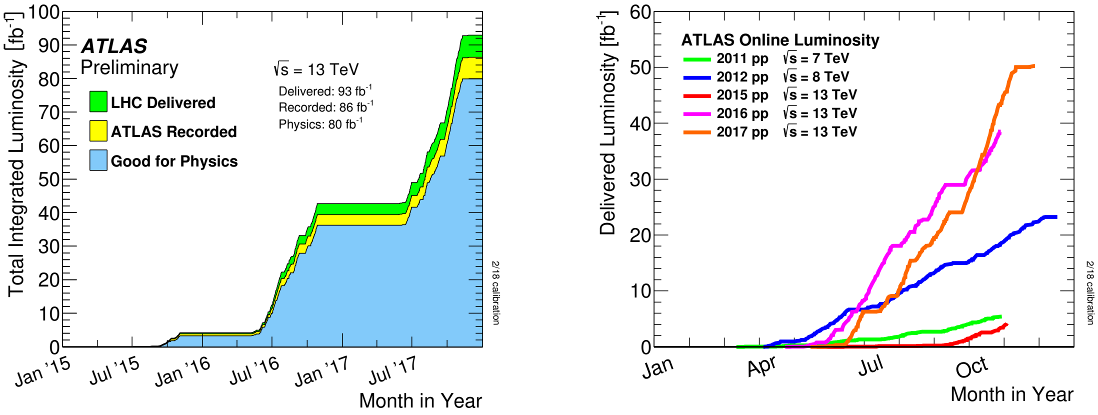

FIGURE 3.3. The total integrated luminosity at the LHC and ATLAS during Run2 (left) and the comparison of integrated luminosities for each year of the ATLAS operation (right).

3.2 A Toroidal LHC ApparatuS

ATLAS is a multi-purpose detector at the Large Hadron Collider. It is placed 100 m below ground near the village Meyrin in Switzerland. With the weight 7000 tonnes, length 46 m, 25 m height and 25 m width, ATLAS is in the fact the largest particle collider detector ever constructed. It is designed to detect particles from the proton-proton collision at the luminosity 10^{34} cm^{-2}s^{-1} and the energy 14 TeV and the ^{208}Pb-^{208}Pb collision at the luminosity 10^{27} cm^{-2}s^{-1} and the energy 5.5 TeV per nucleon pair. The total integrated luminosity of the LHC during 2011-2017 and ATLAS during 2015-2017 running is shown in Figure 3.3. ATLAS consists of several subdetectors with a different pseudorapidity[4] coverage, the largest one $|\eta| < 4.9$ is in the forward hadronic calorimetry. The ATLAS detector is forward-backward symmetric with respect to the interaction point. It consists of four detector systems and solenoidal and toroidal magnet systems. The innermost subdetector is the Inner Detector (ID), which is responsible for the measurement of trajectories of charged particles. The ID is surrounded by the Electromagnetic and Hadronic Calorimeters, the devices measuring the energy of particles passing through the detector, the Electromagnetic Calorimeter detects especially light particles interacting via the electromagnetic force, like electrons, positrons, muons and photons. On the contrary, the Hadronic Calorimeter detects hadrons and mesons. The outermost layer is the Muon Spectrometer, which is designed to measure the muon momentum with

[4]The pseudorapidity detector coordinate is defined as $\eta = -\ln\tan(\Theta/2)$, where Θ is the polar angle from the beam axis.

excellent resolution (80 μm per chamber of Monitored Drift Tubes [45]). The view of the ATLAS detector with its subdetectors is shown in Figure 3.4.

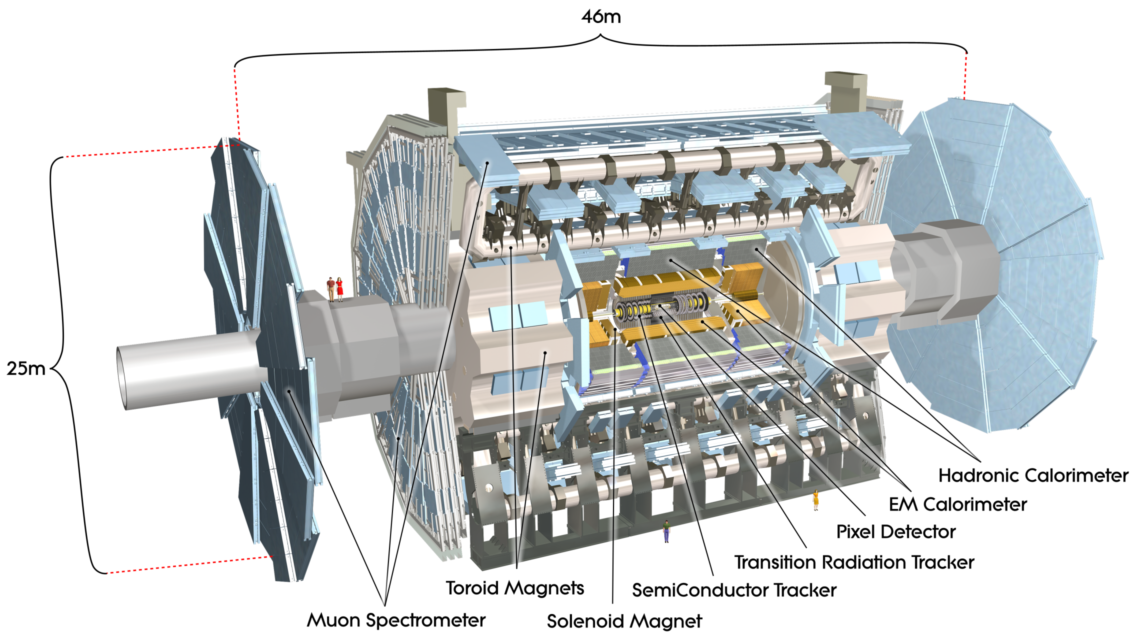

FIGURE 3.4. The ATLAS detector with its subdetectors [45].

3.2.1 Magnet System

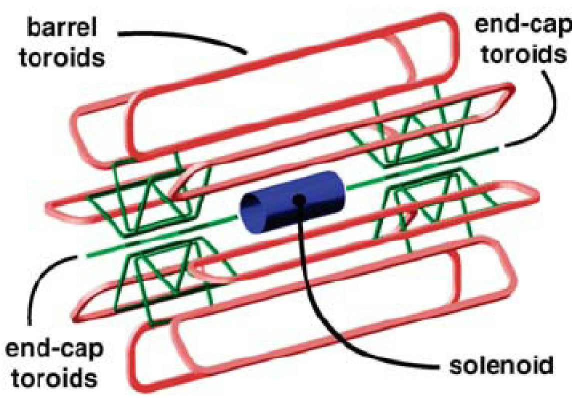

FIGURE 3.5. The ATLAS magnet system [46].

The ATLAS magnet system is 22 m wide and 26 m long [45] and consists of four large superconducting magnets, one solenoid, one barrel toroid and two end-cap toroids (see Figure 3.5).

The Central Solenoid Magnet lies between the ID and Electromagnetic Calorimeter. It is capable to produce a 2 T axial field. This magnet has to be thin in order not to shield particles travelling from Inner Detector to Calorimeter, so the inner and outer diameters are 2.46 m and 2.56 m. Its axial length is 5.8 m. Because this magnet works at temperatures close to absolute zero, the heat shield made of 2 mm thick aluminium panel is added.

The Barrel Toroid consists of eight coils. The overall length of this toroid system is 25.3 m, the inner and outer diameters are 9.4 m and 20.1 m. Each coil is separated and surrounded by cryostats. It produces 0.5 T toroidal magnetic field for the muon spectrometer in the central region.

Similarly to the Barrel Toroid, both End-cap Toroids consist of eight coils, but they are rotated by 22.5° with respect to the Barrel Toroid. Each end-cap toroid produces 1 T magnetic field for the muon spectrometer in the end-cap region.

3.2.2 Inner Detector

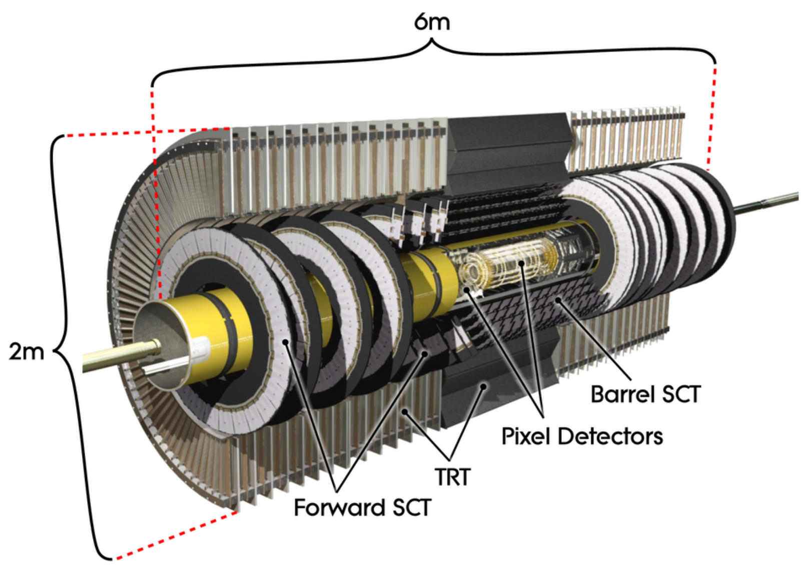

FIGURE 3.6. The ATLAS Inner Detector with its parts [45].

The Inner Detector covers the pseudorapidity $|\eta| < 2.5$ and a full azimuthal angle Φ. It is built few centimetres from the beam axis and its radius is 1.2 m and length is 6.2 m. It provides excellent momentum resolution and vertex reconstruction for charged particles. The Inner Detector consists of Pixel Detectors, SemiConductor Tracker (SCT) and Transition Radiation Tracker (TRT). In the barrel section, Pixel Detector and SCT form cylinders around the beam axis, in the end-cap regions they are located on disks perpendicular to the beam axis. The barrel TRT straws are parallel to the beam direction. The ID immersed in a 2 T magnetic field produced by the central superconducting solenoid. The cut-away view of the ATLAS Inner Detector is shown in Figure 3.6.

3.2.2.1 Pixel Detector

The innermost part of the Inner Detector is the Pixel Detector. It is a system of four layers, the Insertable B-Layer (IBL) was installed during the first long shutdown (2013-2014) [47]. The pixel detector consists of four barrels and of three disks at a distance 59.5 m on each side. This distribution provides three measurement points of each particle travelling from the collision with the maximal pseudorapidity $|\eta| < 2.5$. The Pixel Detector is composed of modules, each module contains 47232 pixels. About 90% of pixels has the area of 50×400 μm^2, the size of the remaining pixels is 50×600 μm^2 (ganged pixels) and 50×250 μm^2 (IBL). To reduce the leakage current, the sensors are operated between -5°C and -10°C.

3.2.2.2 SemiConductor Tracker

The SemiConductor Tracker (SCT) is the middle component of the Inner Detector and encloses the Pixel Detector. It is composed of four layers and provides four hits per track in ideal case. The SCT is especially used for the measurement of momentum. Each layer consists of the barrel modules, that are mounted on cylinders at radii of 29.9 cm, 37.1 cm, 44.3 cm, and 51.4 cm. The SCT consists of 4088 silicon strip sensors forming four cylindrical barrel and two end-caps of nine disks each. The strips in the barrel SCT are parallel to the field produced by the solenoid.

3.2.2.3 Transition Radiation Tracker

The Transition Radiation Tracker (TRT) is a combination of a straw tracker and a transition radiation detector and it is the outermost part of the Inner Detector with the inner radius of 55.4 cm and outer radius of 108.2 cm. The basic TRT elements are polyamide drift (straw) tubes. Each straw is 4 mm in diameter, the maximum length 144 cm in the barrel and 37 cm in the end-cap region and they are are filled with xenon and carbon dioxide gas. The barrel contains about 50000 straws and the end-caps contain 320000 radial straws. The spatial resolution of each straw is 170 μm. These allow the detector to distinguish two types of hits, the tracking hits (pass the lower threshold) and transition radiation hits(pass the higher threshold). The particle with the transverse momentum $p_{\mathrm{T}} > 0.5$ GeV and pseudorapidity $|\eta| < 2$ travelling through the TRT should cross typically more than 30 straws.

3.2.3 Calorimeters

Both electromagnetic and hadronic calorimeter are outside the solenoidal magnet. They are designed to measure the energy of incoming particle by absorbing it with creation of the electromagnetic or hadronic shower. The ATLAS calorimeter system consists of a number of detector. The electromagnetic calorimeters, which are closest to the beam axis are situated in the cryostats, are divided into three parts, a barrel and two end-caps. There is the electromagnetic barrel calorimeter in the barrel cryostat, end-caps contain an ElectroMagnetic End-cap Calorimeter (EMEC), Hadronic End-cap Calorimeter (HEC) behind the EMEC and Forward calorimeter (FCal) closest to the beam axis. The outer calorimeters are scintillator tile barrel and two extended tile barrels. The cut-away view of the ATLAS calorimeter system is shown in Figure 3.7.

3.2.3.1 Electromagnetic Calorimeters

The electromagnetic (EM) calorimeters detect photons and charged particles interacting through the electromagnetic interaction. They deposit part of their energy producing an electromagnetic shower. Lead and stainless steel are used as the energy absorbing material and the liquid argon (LAr) filling EM calorimeters is used as the sampling material due to its stability of response over time. The geometry of calorimeter allows the calorimeters to have several active layers, three in the precision-measurement region $0 < |\eta| < 2.5$, two in the region $2.5 < |\eta| < 3.2$ and one in the overlap region between the barrel and the EMEC. This results to the overall EM calorimeters coverage of the pseudorapidity $\eta < |3.2|$.

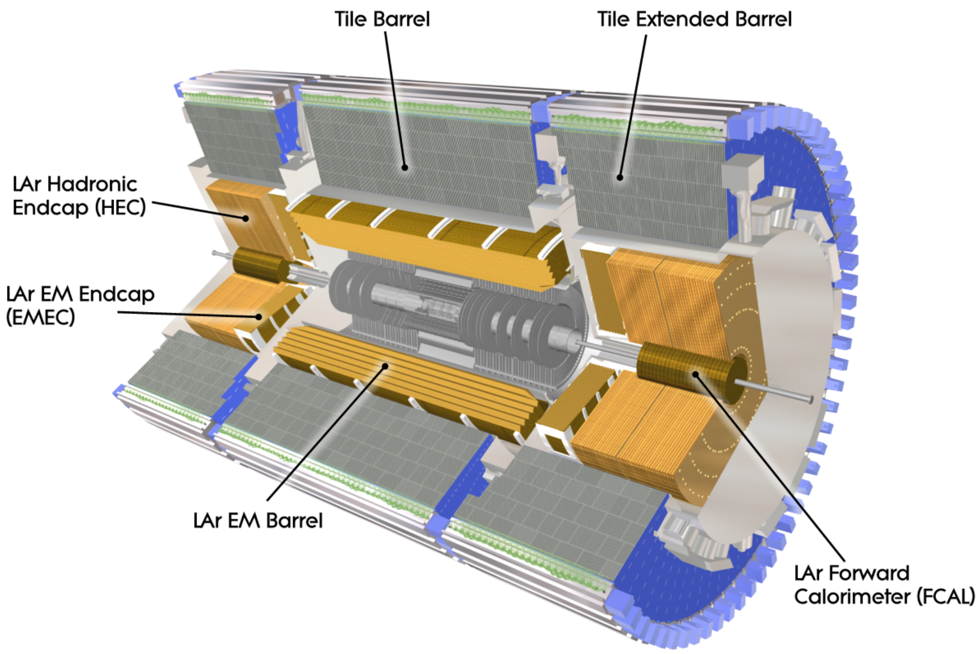

FIGURE 3.7. The ATLAS calorimeter system [45].

3.2.3.2 Hadronic Calorimeters

In contrast with the electromagnetic calorimeter, the hadronic calorimeter detects the particles interacting through the strong interaction, primary the hadrons, which annihilate with the production of the shower. The scintillator tiles are used as sampling medium and for the absorber medium is used steel. The ATLAS hadronic calorimeter system consists of tile calorimeter and and two hadronic end-cap calorimeters (HEC). The tile calorimeter with inner radius 2.28 m and outer radius 4.25 m itself consists of one central barrel and two extended barrels. The barrel part covers the region $\eta < |1.0|$ and extended barrels cover region $0.8 < |\eta| < 1.7$. The tile calorimeter with its extended parts is divided in to three layers.

The LAr (liquid argon) hadron end-cap calorimeter (HEC) uses the copper plates with the LAr gaps as the active medium. Located behind the end-cap electromagnetic calorimeter, with the same LAr cryostats, it is composed of two wheels at each end-cap. Each wheel is segmented into two layers, totally four layers per end-cap region. The HEC overlaps with the pseudorapidity coverage $1.5 < |\eta| < 3.2$ in to the extended tile calorimeter region.

The LAr Forward Calorimeter (FCal) is the outer part in the end-cap cryostat and it consists of three parts, one part made of copper to provide electromagnetic measurements and two parts made of tungsten measure the energy of hadronic interactions. The FCal overall covers the pseudorapidity $3.1 < |\eta| < 4.9$.

3.2.4 Muon Spectrometer

Muons unlike other charged particles are not stopped by the Inner Detector and Calorimeters. To measure their momentum and trajectory, the outermost part of the ATLAS detector system, the Muon Spectrometer, is used. The measurement is based on the examination of the muon track deflection, induced by the ATLAS magnet system. Muons with the psedorapidity in the range $|\eta| < 1.4$ are deflected by the Barrel Toroid, muons with pseudorapidity $1.6 < |\eta| < 2.7$ are bent by end-cap magnet. In the region $1.4 < |\eta| < 1.6$, the deflection is provided by both Barrel Toroid Magnet and End-cap Toroid Magnet. Thus, the overall pseudorapidity coverage by the muon system is $|\eta| < 2.7$. The coverage is provided by Monitored Drift Tubes (MDT's) over the most η and by Cathode Strip Chambers (CSC's) at large pseudorapidity. The ATLAS muon system has also another purpose, the trigger system (for instance, it provide p_{T} threshold or bunch-crossing identification for the muon spectrometer). This system cover the range $|\eta| < 2.4$ and is formed by Resistive Plate Chambers (RPC's) in the barrel section and Thin Gap Chambers (TGC's) in the end-cap regions.
In the barrel region, the muon chambers are arranged three cylindrical layers around the beam axis. Chambers in the end-cap and transition region are also installed in three layers, orthogonal to the beam axis. The view of the ATLAS muon system is shown in Figure 3.8.

3.2.4.1 Monitored Drift Tubes

Monitored Drift Tubes (MDTs) provide precise measurement of muon momentum in almost whole Muon Spectrometer. The basic MDT element is a drift tube with a diameter 29.97 mm and length in a range 0.9 to 6.2 m made of aluminium. The tube is filled with Argon (93%) and Carbon dioxide (7%) at the pressure 3 bar. There is the tungsten-rhenium wire inside the tube, used for the collecting electrons created by the ionization of the gas by incoming particle. Each MDT chamber is formed by two multilayers, which itself consists of three or four layers of the drift tubes. The chambers are equipped with the temperature monitors (for correction of the tube thermal deformation) and

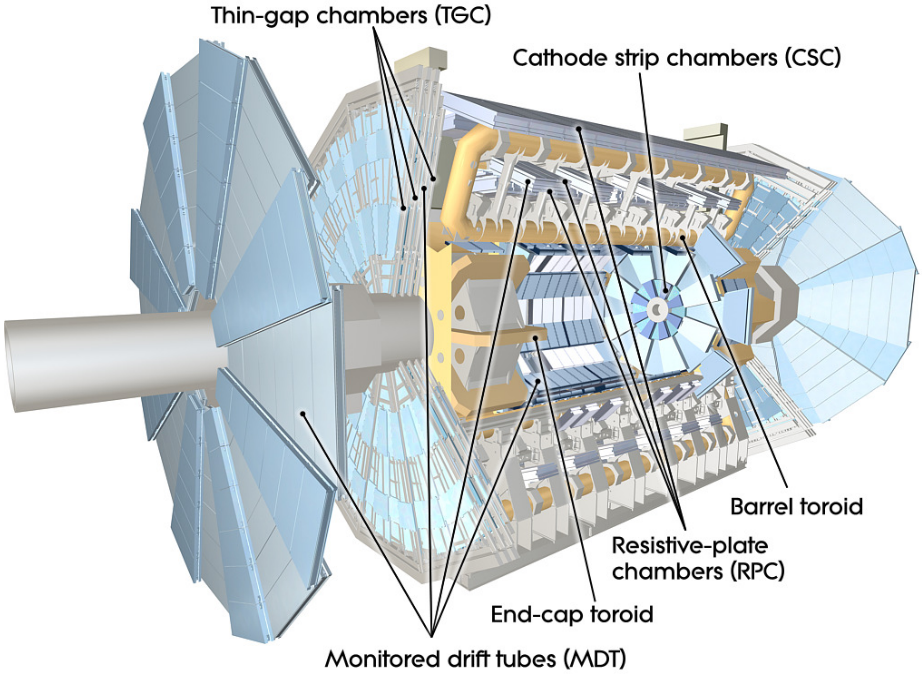

FIGURE 3.8. The ATLAS muon spectrometer [45].

aluminium frame supporting the multilayers is fit up with the monitoring system to control the sagging and torsion of the chamber.

3.2.4.2 Cathode Strip Chambers

Because the MDT has limit of counting rate 150 Hz/cm^2 for safe operation, in the region $|\eta| > 2$, where this limit can be exceeded due to the thermalised neutrons coming from the Calorimeter, the Cathode Strip Chambers (CSCs) are used. CSCs are multi-wire proportional chambers with strip read and form two discs with eight large and eight small chambers each. Each chamber has four CSC plane, so this part provides four independent measurement along each track with the resolution 60 μm in η and 5 μm in the Φ plane. Each chamber consists of four wire planes, so the CSC system provide similar configuration like MDT system, but with higher quality of granularity.

3.2.4.3 Resistive Plate Chambers

The Resistive Plate Chambers (RPCs) serve as the muon trigger in the barrel region and also provide second coordinate measurements. It consists of three layers around the beam axis, two inner layers surround the middle MDTs and the outer layer is located

between the MDT chamber for the large sectors and MDT for small sectors. Two inner RPCs provide the transverse momentum trigger in the range $6-9$ GeV (low-p_{T} trigger) and configuration of inner and outer RPCs provide the p_{T} trigger in the range $9-35$ GeV (high-p_{T} trigger).
RPC has two parallel electrode-plates at the distance 2 mm, made of phenolic-melaminic plastic laminate. The filling gas is the mixture of $C_2H_2F_4$ (94.7%), Iso-C_4H_{10} (5%) and SF_6 (0.3%). The electric field in the gas is 4.9 kV/mm, allowing the formation of the avalanches created by the incoming particle. The signal is read out by the metallic strips, which are installed on the outer side of the resistive plates.

3.2.4.4 Thin Gap Chambers

The Thin Gap Chambers (TGCs) are located in the en-cap region and provide the muon trigger capability and the measurement of the azimuthal coordinate. In the end-cap region, the middle layer of the MDTs is complemented by seven layers of TGCs and the inner layer of the MDTs is complemented by two layers of TGCs, the end-cap (EI) and forward (FI) TGCs. The Thin Gap Chambers do not touch the MDT like the RPCs, but they have own support system or use support system of other parts of the ATLAS apparatus, the EI TGC is for example mounted on the support structure of the barrel toroid coils.
TGC's are multi-wire proportional chambers with the wire-to-cathode distance of 1.4 mm smaller than the wire-to-wire distance of 1.8 mm. The position measurement is made by the strips (azimuthal angle) and wires (pseudorapidity) with pseudorapidity coverage $1.05 < |\eta| < 2.7$. This together with high electric field around the TGC wires leads to very good time resolution for the majority of the muon tracks. The pseudorapidity region for triggering is $1.05 < |\eta| < 2.4$ and important is that the TGCs used for the position measurement are not used for triggering.

3.2.5 ATLAS Upgrade

The Run 2 would end at the end of this year (2018) followed by Long Shutdown LS2. In this shutdown, the detector improvement will be made in order to prepare for the HL-LHC era. In Run 1, the average number of inelastic proton-proton collisions per crossing was $\mu \simeq 25$. This number has increased in run to the value $\mu \simeq 50$. In the HL-LHC, the average number of inelastic proton-proton collisions per crossing is expected to be $\mu \simeq 140-200$ [48].

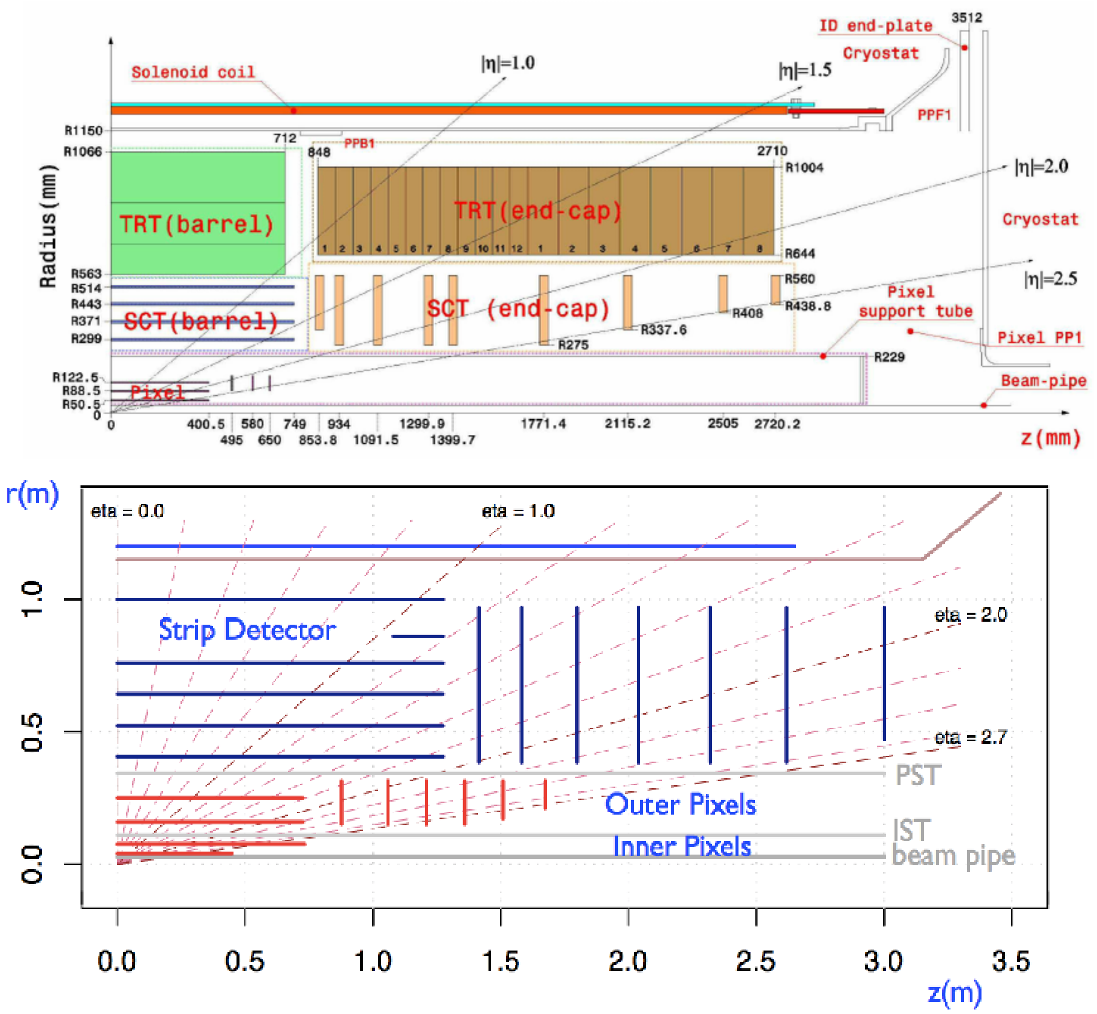

FIGURE 3.9. Comparison of the old [45] (up) and new [49] (down) Inner Detector layout. The new ITk (Inner Tracking) will have extended pseudorapidity coverage up to $|\eta| < 4$ after the LS3 installation.

This increasing luminosity along with data rate and accumulated radiation damage demonstrate that the current ATLAS Inner Detector will be inoperable in the next Run 3 and HL-run. The ATLAS collaboration decided that the Inner Detector will be replaced with a new all-silicon tracker to maintain tracking performance in this high-occupancy environment and to cope with the increase of approximately a factor of ten in the integrated radiation dose [48]. The new ITk (Inner Tracker Detector) has twice the radius and four times the length of the current pixel. The comparison of the old and new inner detector system is shown in Figure 3.9.

The New Small Wheel (NSW) will replace the present innermost stations of the endcap

Muon Spectrometer, the so-called Small Wheels, with a new improved performance detector assembly. New detector technologies used for the NSW, MicroMesh Gaseous Structures (Micromegas, MM) and small-strip Thin Gap Chambers (sTGC) will provide both tracking and triggering information [48].

The increasing collision rate will also make demands on the more effective Level-1 Trigger (L1). Also HLT (High Level Trigger) will have to make complex track-based trigger decisions very rapidly [48].

CHAPTER 4

THE ATLAS TRIGGER SYSTEM AND OFFLINE SOFTWARE

4.1 The Trigger and Data Acquisition System

Operating at the designed luminosity of 10^{34} cm^{-2}s^{-1}, the proton-proton bunch crossing design frequency is 40 MHz [45]. In every bunch crossing dozens of protons interact, so the total inelastic interaction rate is approximately 1 GHz. Due to the technical limitations, only the event rate of about 1 kHz (in Run 2) can be recorded to tape. Therefore, it is important to select interesting events with maximum efficiency in the selected physics channels. This event reduction is performed by the Trigger System, which has two distinct levels, L1 and High-Level Trigger (merged L2 and Event Filter for Run 1) [50]. The architecture of the ATLAS Trigger and Data Acquisition System (TDAQ) in Run 2 is shown in Figure 4.1.

In the first stage of the ATLAS Trigger System, the L1 Trigger reduces the rate from 40 MHz to 100 kHz. Its decision is formed by the Central Trigger Processor (CTP), which uses information from Muon Spectrometer subdetectors and from all calorimeter subsystems. The L1 Calorimeter Trigger (L1Calo) searches events with high transverse energy E_T such as electron, photons, jets and τ-leptons decaying into hadron and also events with large total transverse energy and large missing transverse energy $E_{\mathrm{T}}^{\mathrm{miss}}$. The L1 Muon Trigger receives the signals from the muon trigger chambers RPCs and TGCs. It selects events with high-p_{T} muons based on six p_{T} thresholds.

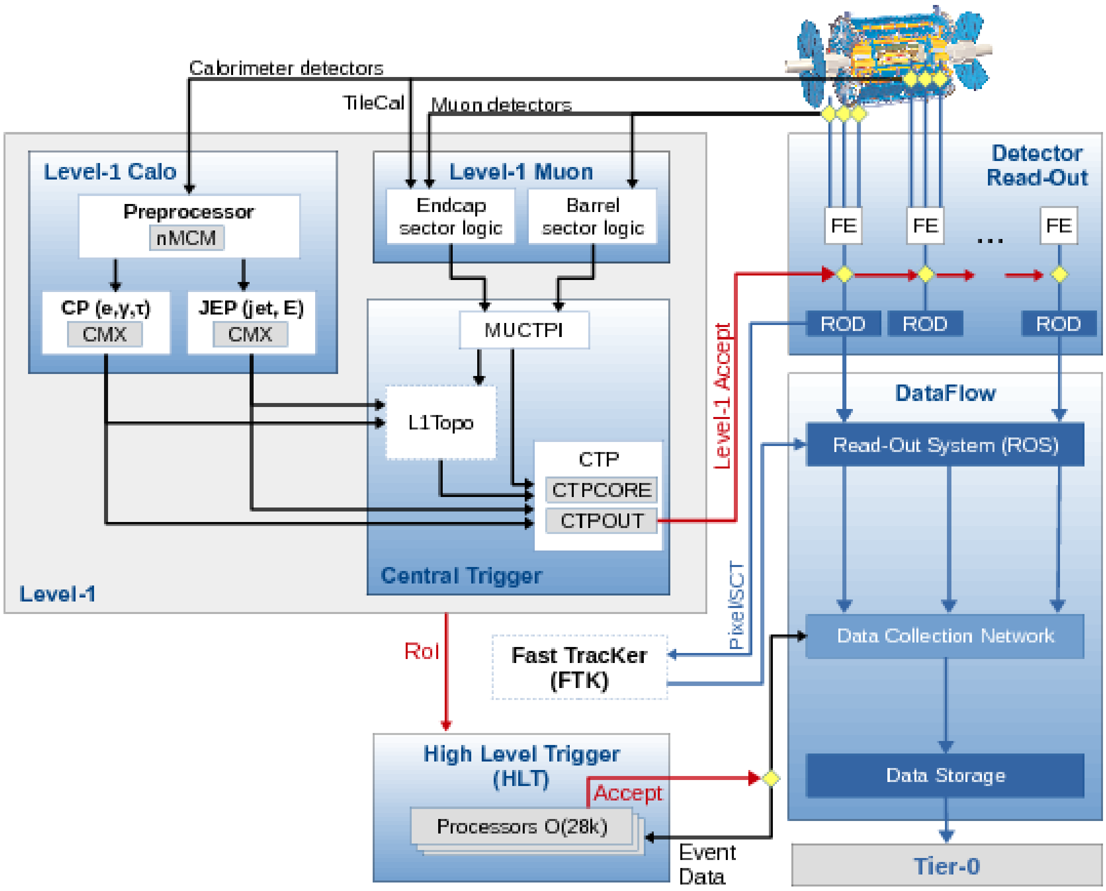

Figure 4.1: The architecture ATLAS Trigger and Data Acquisition System (TDAQ) in Run 2 [51].

The L1 Trigger latency is required to be less than 2.5 μs. The decision together with other signals is sent to the detector front-end system by the Timing, Trigger and Control system (TTC). In case the L1 Trigger accepts the event, the information is sent as a Region-of-Interest (RoI) to the High-Level Trigger.

High-Level Trigger (HLT) works with additional detector information such as the Inner Detector hits, full information from Calorimeter and from muon detectors. The HLT reconstructs the track in RoI using fast reconstruction algorithms. When the event passes the HLT, the selected event is classified and reconstructed with complete detector information. Then, the events are stored for offline reconstruction as a bytestream 'RAW' data and the rate of recording of these events is 1 kHz. The information flow in the beginning with the rate of approximately 10 PB/s is reduced to ~ 1 GB/s. RAW data are further converted using the Athena framework into the xAOD data format, which is used for further physics analyse.

4.1.1 B Physics Trigger

The B mesons (approximately 20 candidates per event) are are in principle cosidered low p_{T} events with respect to the other physics channels, so calorimetry trigger information is not generally used, except the low luminosities, when the background does not dominate. However, the LHC usually operates at high luminosities, so only muon spectrometer can be effectively used for B triggers, typical candle is $J/\psi \rightarrow \mu^+\mu^-$ decay.
The B trigger system is composed of several triggering algorithms. Beside the most dominant di-muon vertex trigger, where muons with transversal momentum greater than some predefined threshold (4 or 6 GeV) are required to be originating from a common vertex, single or two muon triggers also exists. These serve as control and calibration triggers since they are the least complicated but inefficient at selecting interesting events.

4.1.2 Muon Triggers

The L1 muon selection is based on the measurement of the p_{T}, which can be measured thanks to the barrel and end-cap toroid magnetic system. The toroids produce strong magnetic field (4 T), where muon tracks are curved and give the muon p_{T} indication by passing through the Muon Spectrometer layers. The muon trigger has hardware logic designed for low p_{T} (for B physics) and high p_{T} (e. g. Higgs physics) thresholds. For low p_{T} muons, hits in two inner RPC and two outer TGC layers are required. The thresholds are usually at value 4,6 or 8 GeV in order to remove background from decays-in-flight such as π/K.

4.2 Muon Reconstruction

The muons are an important tool for studying the variety of high energy physics processes, including the B physics properties and the study of charmonia, because charmonia can decay via the electromagnetic interaction into two oppositely charged muons. While events with these muons are triggered and saved to disk (ATLAS online algorithms), they are reconstructed (by ATLAS offline algorithms) using information from the Inner Detector and Muon Spectrometer. Muon track candidates are connected with hits in segments of the detector (especially in the Muon Spectrometer). If the fit used for the hit association satisfies the selection criteria, the track is assigned to muon.

4.2.1 Types of Muons

Muons differ in the information from ATLAS sub-detector used for the offline reconstruction. Generally, muons are divided into four groups: Combined, Segment-tagged, Calorimeter-tagged and Extrapolated muons [52].

Combined muons: The reconstruction uses the fitted hits obtained independently by the Inner Detector and Muon Spectrometer. To improve the fit quality, some tracks can be added or removed. This refit can be made for example by the *MuId* algorithm [53]. These muons are used for the J/ψ reconstruction in order to ensure a good quality of the signal.

Segment-tagged muons: The tracks in the Inner Detector assigned to muons are extrapolated to the hits in the Muon Spectrometer. When there is only one hit in the Muon Spetrometer, the reconstructed muons are called segment-tagged muons. The common algorithm for reconstruction of these muons is *MuTag*. [54].

Calorimeter-tagged muons: When tracks in the Inner Detector is associated with muons, the energy deposited in the Calorimeter is also connected with these track, but not connected with hits in the Muon Spectrometer, the muons are called Calorimeter-tagged muons. These muon are located primarily in the region, where is no Muon Spectrometer coverage because of the support system of the Inner Detector and the Calorimeter [53].

Extrapolated muons: These muons, also called stand-alone muons, are associated only with the track in the Muon Spectrometer, which are extrapolated to the interaction point. To be classified as this type, the muon has to hit at least two layers of the Spectrometer. The track can be reconstructed for example by the *Muonboy* algorithm [54].

4.2.2 Muon Qualities

The muons are reconstructed with different quality of the fit (association to the track). There exist four groups of muons according their quality of offline reconstruction: tight muon, medium muons, loose muons and very loose muons [55].

Very loose muons: The reconstructed muons can have very small reliability of the particle identification to muon. When track is not included into loose, medium or tight muon group, but is still considered to be muon, it is called very loose muon.

Loose muons: The loose identification criteria are designed to maximize the reconstruction efficiency while providing good quality muon tracks. All muon types are used, calorimeter-tagged and segment-tagged muons are restricted to the area with psedorapidity $\eta \approx 0$ because of the cabling in the area [55].

Medium muons: The Medium identification criteria provide the default selection for muons in ATLAS. They minimize the systematic uncertainties associated with muon reconstruction and calibration. Only combined and standalone muons are used in this selection. Standalone medium muons require at least three hits in each of the three layers of MDT or CSC. Combined medium muons satisfy condition of at least two hits on at least two layers of MDT [55].

Tight muons: Tight muons are selected to optimize the purity of the sample. Only tracks associated to the combined muon and satisfying the Medium requirements are considered. To remove fake tracks,cuts on the the normalized χ^2 of the combined track fit and on the compatibility between the momenta measured in the ID and MS are applied [55].

4.3 ATLAS Offline Software

4.3.1 The Athena Framework

A majority of the ATLAS software is implemented within the Athena, an object-oriented framework designed to provide a common infrastructure and environment for simulation, reconstruction and analysis applications of a high-energy physics experiment. It is based on C++ and Python and it is an implementation of the underlying Gaudi [56], architecture developed by the LHCb but commonly used by both ATLAS and LHCb.
The Athena contains a skeleton of an application, into which the developers can plug-in their codes. Also in the Athena, the data in RAW format is transformed into xAOD (formerly AOD) and it serves as a central software repository of all algorithms. The

data slimming together with production of NTuples and production of the Monte Carlo samples were run in the Athena in this analysis. The places, where the Athena is used in the ATLAS data flow, are shown in Figure 4.2.

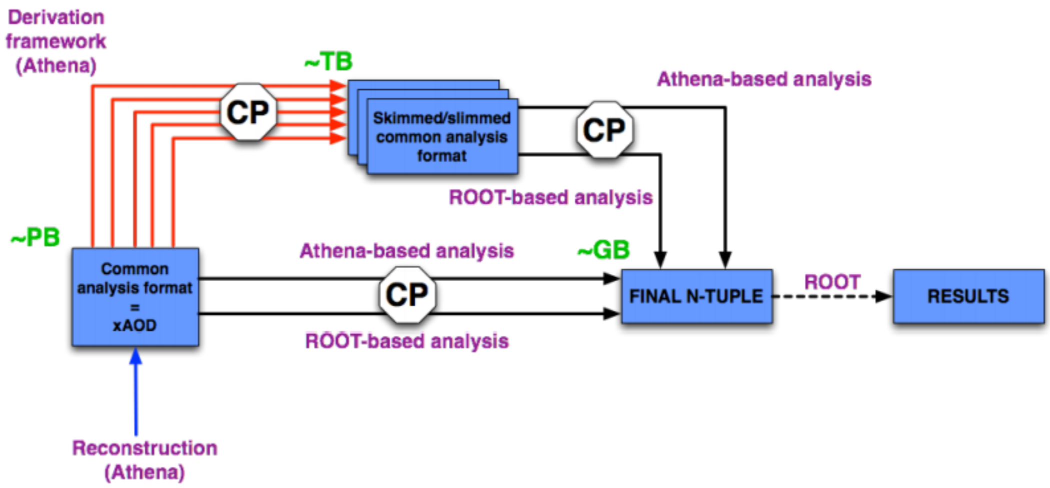

FIGURE 4.2. : The ATLAS Run 2 analysis model showing how the reconstruction output (xAOD) is transformed by derivation framework into multiple streams of DxAOD [57]. Both xAOD and DxAOD are then used for the production of NTuples, where partial results and other needed information are stored.

4.3.2 ROOT Framework

ROOT [58] is an object-oriented framework and it was originally designed at CERN by René Brun and Fons Rademakers. It has a C/C++ interpreter (CINT) and C/C++ compiler (ACLIC) and can be used as an interactive environment (running code in the command line) or execute scripts. Its large advantage is the ability to handle large files. It is able to make multi-dimensional histograms, curve fitting and storage of analysis results as ROOT files. ROOT provides the Virtual Monte Carlo interface to simulation engines such as Geant 4 and can be also used to develop an event display, an application providing the detector geometry or the particle path visualisation [59].
The ROOT version 6.04.00 is primarily used to plot histograms in the analysis presented in this thesis.

4.3.2.1 Roofit

Roofit [60] is a library of C++ classes providing the data fitting and modelling in the ROOT framework. In was originally developed for the BaBar collaboration at Stanford Linear Accelerator Center.
Roofit works with the normalised PDFs (Probability Density Functions) describing the probability density of the observables distribution with respect on the parameters of the density function.
Roofit can be used to perform unbinned and binned maximum likelihood fits and to produce plots. It also allows multidimensional fitting, description of correlations between observables and the universal implementation of toy Monte Carlo sampling techniques.
The Roofit is used for fitting and computing fit parameters in presented analysis.

4.3.2.2 sPlot

The sPlot [61] technique is a statistical tool dedicated to the analysis of a data sample consisting several sources of events (like signal and background source). These sources are merged into one sample which contains variables with known signal and background distributions. These variables are called discriminating variables. Using known distributions, sPlot can compute a particular weight (likeliness that the event is of signal type or background type). These weights (called sWeights) are applied on control variables, in order to obtain signal and background distributions separately. More details can be found in [61].
In this analysis, the B^+ mass is used as the discriminating variable and the muon charge is used as the control variable.

CHAPTER 5

Tagging in $B^\pm \to J/\psi(\mu^+\mu^-)K^\pm$ Channel

In this chapter, flavour tagging in the $B^\pm$ channel is described. The quality of the tag is measured in terms of tagging efficiency, dilution, wrong tag fraction and tagging power. For improvement of the tagging results, the weighted charge in the cone around the muon track is calculated. Finally, the B^+ tagging probability estimate (the calibration curve) for implementation of the tagging information into the CP violation measurement in $B_s^0 \to J/\psi(\mu^+\mu^-)\phi(K^+K^-)$ decay channel is acquired.

5.1 Flavour Tagging Variables

In the following text, a definition of tagging efficiency, dilution, wrong tag fraction, tag power, cone charge and B^+ is presented.

5.1.1 Efficiency

The tagging efficiency is the ratio of the events that can be used for tagging over the total number of events,

$$\epsilon_{tag} = \frac{N_r + N_w}{N_B}, \tag{5.1}$$

where N_r and N_w are number of correctly and incorrectly tag events and N_B is the total number of events with a measured B meson.

5.1.2 Dilution and Wrong Tag Fraction

The dilution describes the purity of the tagging,

$$D_{tag} = \frac{N_r - N_w}{N_r + N_w} = 1 - 2w_{tag}, \tag{5.2}$$

where the variable w_{tag} is the wrong tag fraction, the fraction of the incorrectly tagged events

$$w_{tag} = \frac{N_w}{N_r + N_w}. \tag{5.3}$$

Better tagging has the wrong tag fraction small (ideally zero) and the dilution close to 1.

5.1.3 Tagging Power

Combining the efficiency and dilution, the tagging power is defined as

$$P_{tag} = \epsilon D^2 = \sum_i \epsilon_i D_i^2. \tag{5.4}$$

The tagging power is not directly used as a calibration to $B_s^0 \to J/\psi\phi$ data, but it is useful when selecting the optimum tagging criteria and it helps understanding of the tagging method by describing both the purity of tagging and the ratio of tagged events.

5.1.4 Cone Charge and Tagging Probability

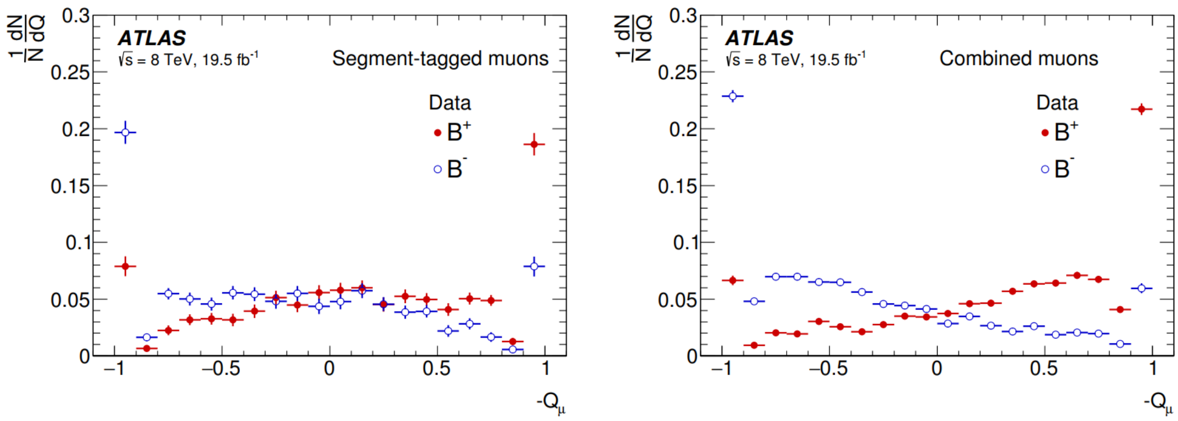

FIGURE 5.1. The opposite side cone charge distribution for $B^{\pm}$ candidates using the combined and segment tagged muons [37].

As stated in the previous chapters, the opposite side b quark can decay via the chained semileptonic decay $b \to c \to \mu$ instead of $b \to \mu$. To optimize the tagging performance, a cone charge variable is constructed around the muon, electron or jet, defined (for muons) as [37]

$$Q_\mu = \frac{\sum_i^{Ntracks} q_i (p_{\mathrm{T}})^\kappa}{\sum_i^{Ntracks} (p_{\mathrm{T}})^\kappa}, \tag{5.5}$$

where q_i is charge of the track, $\kappa = 1.1$ and the sum is performed over the reconstructed Inner Detector tracks within a cone $\Delta R = \sqrt{(\Delta\phi)^2 + (\Delta\eta)^2} < 0.5$ around the muon direction[1]. The cone charge distribution is shown in Figure 5.1. If there are no additional tracks within the cone, the charge of the muon is used. Tracks associated to $B^\pm$ are excluded from the cone charge. The cone charge for combined and segment tagged muons can be seen in Figure 5.1.

To transfer the tagging information from $B^\pm$ into B_s^0 events, the tagging probability is used. Probability, that specific event has B meson containing b quark (B^- meson) or $\bar{b}$ (B^+ meson) is denoted as $P(Q|B^+)$ or $P(Q|B^-)$, respectively. Then, the probability to tag the event as containing $\bar{b}$ is [37]

$$P(B|Q) = \frac{P(Q|B^+)}{P(Q|B^+) + P(Q|B^-)} \tag{5.6}$$

and $P(\bar{B}|Q) = 1 - P(B|Q)$ is the probability to tag the event as containing b. The probability distributions for segment tagged muons, separated into single-track events (left) and cone-charge (right) are in Figure 5.2.

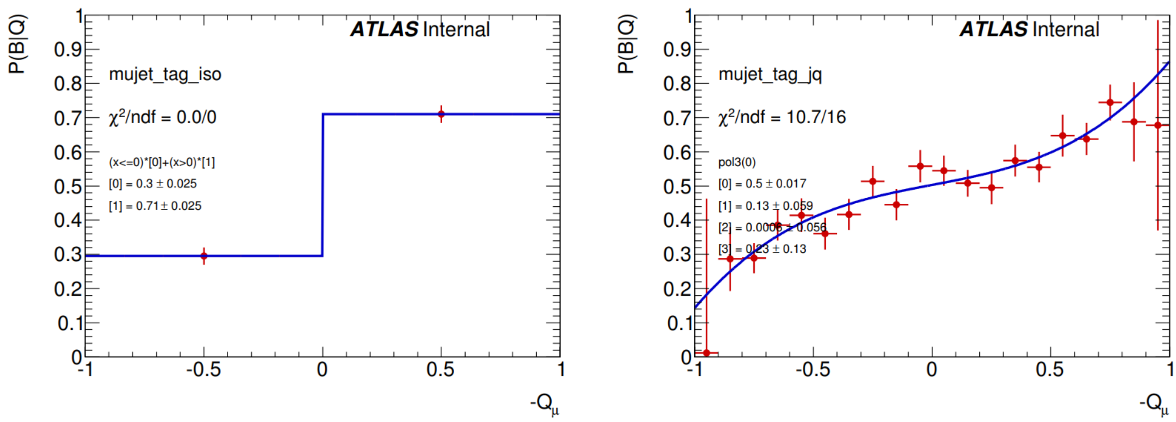

FIGURE 5.2. The probability distribution for segment tagged muons, separated into single-track events (left) and cone-charge (right) [37]. The reason of splitting the tag probability into two part is different treatment of these two parts in the B_s^0 fit described in chapter 6.

[1]The pseudorapidity detector coordinate is defined as $\eta = -\ln\tan(\Theta)$, where Θ is the polar angle from the beam axis. ϕ is the azimuthal angle around the beam axis.

5.2 Data Selection

The data used in this analysis were recorded by the ATLAS experiment in proton-proton collisions during the year 2015 and 2016 $\sqrt{s} = 13\,\text{TeV}$ in both record streams (main and delayed stream). The Good Runs Lists physics_25ns_21.0.19.xml[2] for both years have been applied at the Athena level to remove the luminosity blocks that are not cleared to be used for physics analysis. The data with integrated luminosity

$$\int L\mathrm{d}t = 36.2\,\mathrm{fb}^{-1}$$

were recorded in total during the time period.
In order to remove large number of background events, some selection cuts are applied. The B candidate must satisfy invariant mass condition $5.0 < m(B) < 5.7$ GeV, the transversal momentum $p_\mathrm{T}(B^\pm) > 10\,\text{GeV}$ and pseudorapidity $|\eta(B)| < 2.5$. Additionally, candidates must pass the lifetime cut $\tau > 0.2\,\text{ps}$ applied to remove prompt component of the background and the probability of the vertex fit must be better than $\chi^2 < 10.8$ for one degree of freedom. Additionally, the kaon must satisfy $p_\mathrm{T}(K) > 1$ GeV and $|\eta(K)| < 2.5$ and the J/ψ candidates are reconstructed from two oppositely-charged muons with transversal momentum $p_\mathrm{T}(\mu) > 4$ GeV and pseudorapidity within $|\eta(\mu)| < 2.5$. The third muon used for opposite tagging passes the $|\eta(\mu)| < 2.5$ and $2.5 < p_\mathrm{T}(\mu) < 4$ GeV (so called low-p_T muons) or $p_\mathrm{T}(\mu) > 4$ GeV (tight muons) criteria.

5.3 $B^\pm \to J/\psi K^\pm$ Mass Fit

In this section, the $B^\pm \to J/\psi K^\pm$ mass fit is discussed. The signal-to-background fraction is used for the sideband subtraction method.

5.3.1 Fit Model

An unbinned maximum likelihood fit is performed using roofit on the selected data to fit the invariant mass of B^+ and B^- in the exclusive channel. The signal part is described by two Gauss functions with the same mean. The background is defined by a combination of exponential constant function to describe the overall background and by inverse

[2] http://atlas.web.cern.ch/Atlas/GROUPS/DATABASE/GroupData/GoodRunsLists/data16_13TeV/20180129/,
http://atlas.web.cern.ch/Atlas/GROUPS/DATABASE/GroupData/GoodRunsLists/data15_13TeV/20170619/

hyperbolic tangent function to describe partially reconstructed B candidates. Then, the total likelihood function is defined as a combination of the signal and background probability density functions

$$\begin{aligned} PDF = & f_{sig}[f_{gauss}G_1(\mu,\sigma_1)+(1-f_{gauss})G_2(\mu,\sigma_2)]+ \\ & +(1-f_{sig})[f_{bck1}E(\lambda)+f_{bck2}C+(1-f_{bck1}-f_{bck2})AT(sc,of)], \end{aligned} \tag{5.7}$$

where $G_1(\mu,\sigma_1)$ and $G_2(\mu,\sigma_2)$ are Gauss functions with the same mean μ, $E(\lambda)$ is the exponential function with the slope λ, C is constant function and $AT(sc,of)$ is atanh with the offset of and scale sc. The coefficients f_{sig}, f_{gauss}, f_{bck1} and f_{bck2} are the scale factors between the functions. The coefficients of the fit are in Table 5.1 and the result plots are shown in Figure 5.3.

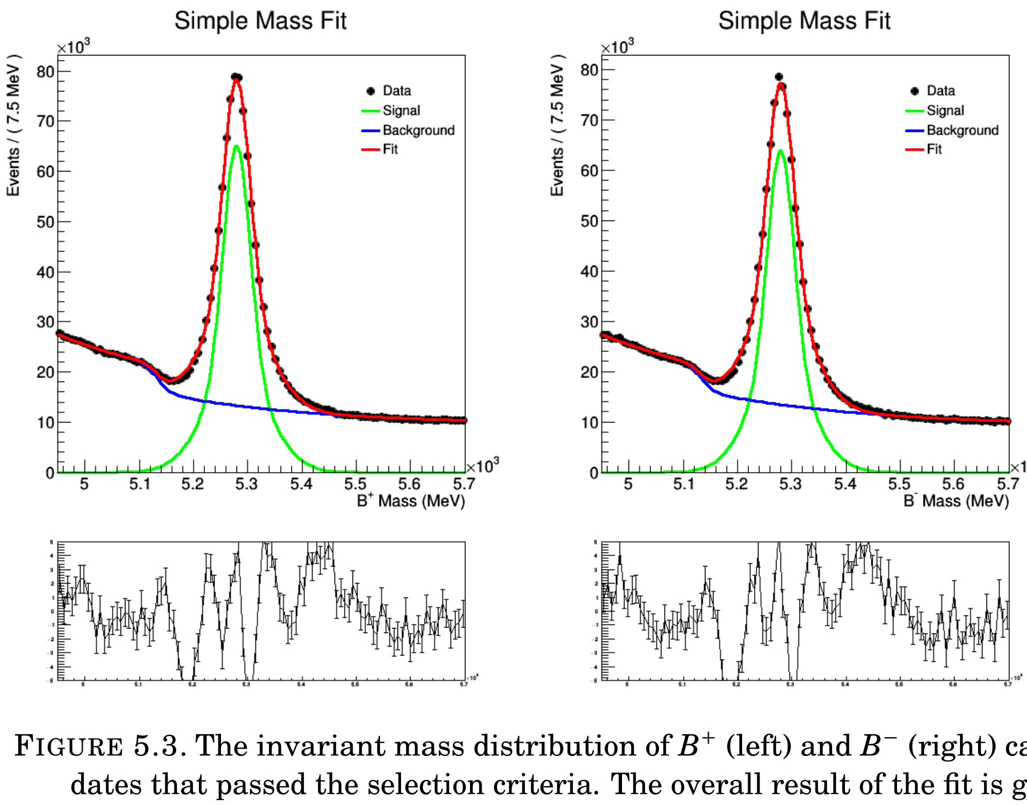

FIGURE 5.3. The invariant mass distribution of B^+ (left) and B^- (right) candidates that passed the selection criteria. The overall result of the fit is given by a red curve, the signal component is denoted by a green curve and the background function with the partially reconstructed B is given by blue curve.

μ	σ_1	σ_2	λ	sc	of	f_{sig}	f_{gauss}	f_{bck1}	f_{bck2}
5279.38	24.5	58.8	-0.00360	-0.042	5133.9	0.331	0.506	0.282	0.627
0.06	0.2	0.5	0.00006	0.002	0.79	0.001	0.006	0.006	0.004
5279.45	23.9	56.5	-0.00340	-0.043	5133.4	0.325	0.481	0.311	0.605
0.06	0.2	0.5	0.00007	0.003	0.9	0.001	0.006	0.009	0.005

TABLE 5.1. Fitted parameters of the total probability density function (5.7). The constant function C is set to be free because of the fit function normalization. μ, σ_i are measured in MeV, meanwhile λ and sc are measured in MeV^{-1}. The rest of parameters is dimensionless.

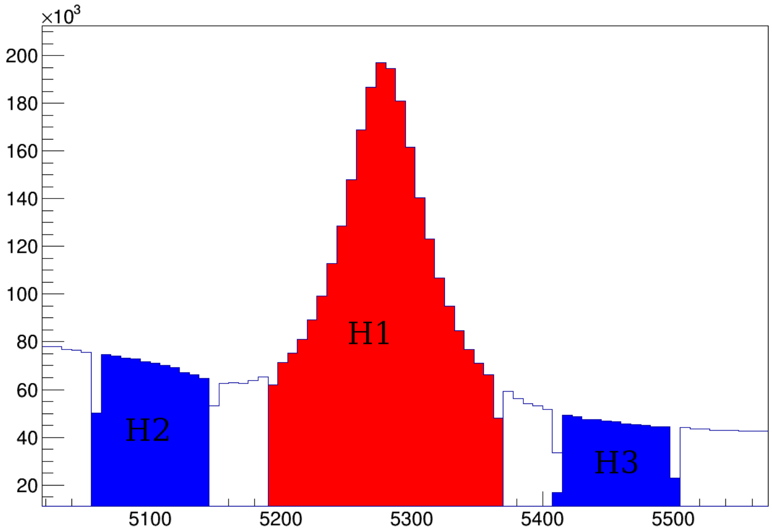

FIGURE 5.4. The sideband subtraction method. $H1$ is the signal region with the number of background candidates Nbg_{sigreg}, $H2$ and $H3$ are the sideband regions with the number of background candidates Nbg_{LSB} and Nbg_{RSB}.

5.3.2 Sideband Subtraction

To study parameter distribution corresponding to the $B^{\pm}$ signal with the background subtracted, sPlot (described in the section 4.3.2) or sideband subtraction can be used.
It is assumed that the background distribution of quantity of interest under the signal peak is approximately identical to the distribution of the background away from the peak region (sidebands).
There are three mass distribution regions defined. The signal region (histogram $H1$ in Figure 5.4) is defined to be $\pm 2\sigma$ around the Gauss mean, where σ is normalisation-weighted average sigma between the narrow and wide Gauss functions (for B^+ it is $\sigma = 44.8 \pm 0.3$, for B^- it is $\sigma = 44.0 \pm 0.3$). The left ($H2$ in Figure 5.4) and right ($H3$ in

Figure 5.4) sideband region are the mass interval $(\mu-5\sigma;\mu-3\sigma)$ and $(\mu+3\sigma;\mu+5\sigma)$. The sideband subtraction method can be also used for the opposite side tagging method. Defining histogram of the opposite side muons charge for $B^{\pm}$ candidates in the mass signal region $G1$ and histograms of the opposite side muons charge for $B^{\pm}$ candidates in the left and right sideband regions $G2$ and $G3$, the number of third muons is

$$G_{final} = G1 - \frac{Nbg_{sigreg}}{Nbg_{LSB} + Nbg_{RSB}} (G2 + G3) = A(G2 + G3), \tag{5.8}$$

where Nbg_{RSB}, Nbg_{LSB} and Nbg_{sigreg} are numbers of muons defined in the Figure 5.4 and their values with statistical errors for both B^+ and B^- are in Table 5.2. Approximately 90% of the signal events are retained.

	Nbg_{SIGREG}	Nbg_{LSB}	Nbg_{RSB}	A
B^+	319600 ± 500	256300 ± 400	137600 ± 200	0.812 ± 0.002
B^-	316300 ± 500	247200 ± 400	135000 ± 200	0.828 ± 0.002

TABLE 5.2. Values and errors of the parameters extracted from the fit using the equation (5.8) and the distribution in Figure 5.4.

5.4 Single Muon Tagging

Not all muon categories in reconstruction quality or type are suitable for the flavour tagging. This section demonstrates the differences in results between sPlot and sideband subtraction methods. It also shows the best selection criteria for the tagging muons (without tracks in cone around these muons). Number of all B events, correctly and incorrectly tagged events obey the Poisson statistics, so the statistical uncertainty of the number of events N is $\sqrt{N}$. Then, all the statistical uncertainties in this section were calculated using the equations (5.1), (5.2) and (5.3) and the definition of the indirect measurement uncertainty, where squared statistical uncertainty of efficiency, dilution or tag power is equal to the sum of partial derivative of a given quantity squared multiplied by its squared error.

5.4.1 Sideband Subtraction versus sPlot

During the analysis, there were two options how to calculate the tag power for muons - the sideband subtraction (described in previous section) and the sPlot (described in section 4.3.2.2). In order to compare these two methods, the same statistical sample was used. The results of the comparison are shown in Table 5.3. The sideband subtraction method has slightly larger efficiency than the sPlot method. Despite this fact, the tag power for both methods is similar, so both methods are equivalent within the statistical uncertainties. Because of the clarity of the code and fast data handling, only the sPlot method is used in later analysis.

	$\epsilon_{\mathbf{tag}}$ (%)	$\mathbf{D_{tag}}$	$\mathbf{P_{tag}}$ (%)
combined	7.44 ± 0.02	0.219 ± 0.003	0.35 ± 0.01
segmentTag	0.75 ± 0.01	0.037 ± 0.009	0.0010 ± 0.0004
caloTag	4.30 ± 0.02	0.021 ± 0.004	0.0019 ± 0.0006
combined	7.88 ± 0.02	0.215 ± 0.003	0.36 ± 0.01
segmentTag	0.792 ± 0.007	0.030 ± 0.009	0.0007 ± 0.0004
caloTag	4.40 ± 0.02	0.025 ± 0.004	0.0028 ± 0.0008

TABLE 5.3. The tag efficiency ϵ_{tag}, dilution D_{tag} and tag power P_{tag} for different muon qualities. Top part of table contains results using the sPlot method, bottom part shows results obtained using the sideband subtraction method. Both tables use same selection criteria, where muon type has higher priority than higher p_{T}.

5.4.2 Order of Selection Criteria

Muons can be divided into groups by two aspects - by the muon quality or by the muon type (see section 4.2). The previous analysis has been made using the combined and segment-tagged muons and only one muon with highest transversal momentum (p_{T}) per event is selected. However, the classification of muons between Run 1 and Run 2 has changed, so both ways have to be tested. Moreover, the order of selection criteria is important, such as there are two possibilities of selection strategies:

- In each event, muon with highest p_{T} is selected. Then, its type or quality is checked and muon with better type within a given sequence of muon types combined-segmentTagged-caloTagged is used for tagging.

- Firstly, the quality or type of all muons in each event is checked. The group with only the best quality (tight muon has better quality than medium muon, medium muon has better quality than loose muon, etc.) or type (combined-segmentTagged-caloTagged) is used. If there is no tight muon, the group with medium quality muons is used and so on. Then, the muon with highest p_{T} in the selected group is only used for the tagging.

	$\epsilon_{\mathbf{tag}}$ (%)	$\mathbf{D_{tag}}$	$\mathbf{P_{tag}}$ (%)
tight	3.02 ± 0.01	0.392 ± 0.004	0.46 ± 0.01
medium	0.158 ± 0.003	0.14 ± 0.02	0.0032 ± 0.0009
loose	0.121 ± 0.003	0.09 ± 0.02	0.0012 ± 0.0005
very loose	8.02 ± 0.02	0.031 ± 0.003	0.008 ± 0.001
tight	4.18 ± 0.02	0.355 ± 0.004	0.53 ± 0.01
medium	0.210 ± 0.004	0.11 ± 0.02	0.0027 ± 0.0009
loose	0.172 ± 0.003	0.09 ± 0.02	0.0013 ± 0.0006
very loose	7.93 ± 0.02	0.028 ± 0.003	0.006 ± 0.001

TABLE 5.4. The tag efficiency ϵ_{tag}, dilution D_{tag} and tag power P_{tag} for different muon qualities. The top part of table shows results for ordering of selection criteria, where higher p_{T} has higher priority than muon quality. The bottom part of table shows results selection criteria, where muon quality has higher priority than higher p_{T}. Tables were produced using the sPlot.

	$\epsilon_{\mathbf{tag}}$ (%)	$\mathbf{D_{tag}}$	$\mathbf{P_{tag}}$ (%)
combined	5.27 ± 0.02	0.244 ± 0.004	0.314 ± 0.009
segmentTag	0.512 ± 0.006	0.04 ± 0.01	0.0010 ± 0.0005
caloTag	5.53 ± 0.02	0.026 ± 0.004	0.0024 ± 0.0008
combined	7.44 ± 0.02	0.219 ± 0.003	0.35 ± 0.01
segmentTag	0.75 ± 0.01	0.037 ± 0.009	0.0010 ± 0.0005
caloTag	4.30 ± 0.02	0.021 ± 0.004	0.0018 ± 0.0007

TABLE 5.5. The tag efficiency ϵ_{tag}, dilution D_{tag} and tag power P_{tag} for different muon types. The top part of table shows results for order of selection criteria, where higher p_{T} has higher priority than muon type. The bottom part of table shows results selection criteria, where muon type has higher priority than higher p_{T}. Tables were produced using the sPlot.

The comparison of these two selection orders is shown in Tables 5.4 and 5.5. The standalone muons are considered in both tables, but at the end of the selection chain, the are thrown away and not considered further. This together with selection order causes lower total efficiency of the muons in the top table. The dilution seems to be similar in both selection chains and the tag power is larger for the second selection chain. Comparing the tag power with respect to the muon quality and muon type, the tight muon has considerable larger tag power. This leads to the conclusion to use only the tight muons for the tagging and exclude all standalone muons from the analysis.

5.4.3 Additional Cuts

Solving the issue with tagging method, usage of type or quality criteria and the order of selection criteria, the tag power in Tables 5.3, 5.4 and 5.5 is still smaller that the tag power from the Run 1 analysis [37]. The reason can be larger pile-up[3] in Run 2. Therefore, some additional cuts had to be made. For example, muon should pass Δz cut of the primary vertex. As it is clear in Figure 5.5, the impact parameter of muon trajectory relative to primary vertex must be smaller than $|\Delta z| < 5$ mm. Also the p_{T} dependence of efficiency, dilution and tag power has been checked, see Figures 5.6, 5.7 and 5.8. Dilution appears to have plateau around 50% from $p_{\mathrm{T}} > 10$ GeV, the efficiency and tag power are higher for low p_{T} tagging muons.

Table 5.6 shows final efficiency, dilution and tag power after applying the Δz cut.

The tag power for tight muons looks satisfactory, since it has larger value than the tag power from [37], where is was improved by the cone charge. However, not all data from dataset were used, the tag variables are calculated with 2016 data only.

Within this data analysis, two stream of data taking are combined. The Table 5.6 shows the comparison between the live and delayed stream. The tag power is significantly larger in the live stream than in the delayed stream. However, both streams are used for the cone charge analysis to have statistical sample as large as possible.

	$\epsilon_{\mathbf{tag}}$ (%)	$\mathbf{D_{tag}}$	$\mathbf{P_{tag}}$ (%)
tight	7.75 ± 0.02	0.358 ± 0.003	0.99 ± 0.02
medium	0.471 ± 0.005	0.12 ± 0.01	0.007 ± 0.001
loose	0.353 ± 0.005	0.09 ± 0.01	0.0030 ± 0.0009
very loose	12.52 ± 0.03	0.044 ± 0.002	0.024 ± 0.003
tight	6.50 ± 0.02	0.451 ± 0.003	1.32 ± 0.02
medium	2.41 ± 0.01	0.253 ± 0.005	0.154 ± 0.006
loose	0.984 ± 0.008	0.175 ± 0.008	0.0030 ± 0.0003
very loose	17.71 ± 0.04	0.062 ± 0.002	0.068 ± 0.004

TABLE 5.6. The tag efficiency ϵ_{tag}, dilution D_{tag} and tag power P_{tag} for different muon qualities with Δz cut applied. Results are shown for delayed stream (top) and live stream (bottom).

[3]The high luminosity of the LHC results in a significant background to interesting physics events known as pile-up, additional proton-proton collisions in the event to the collision of interest.

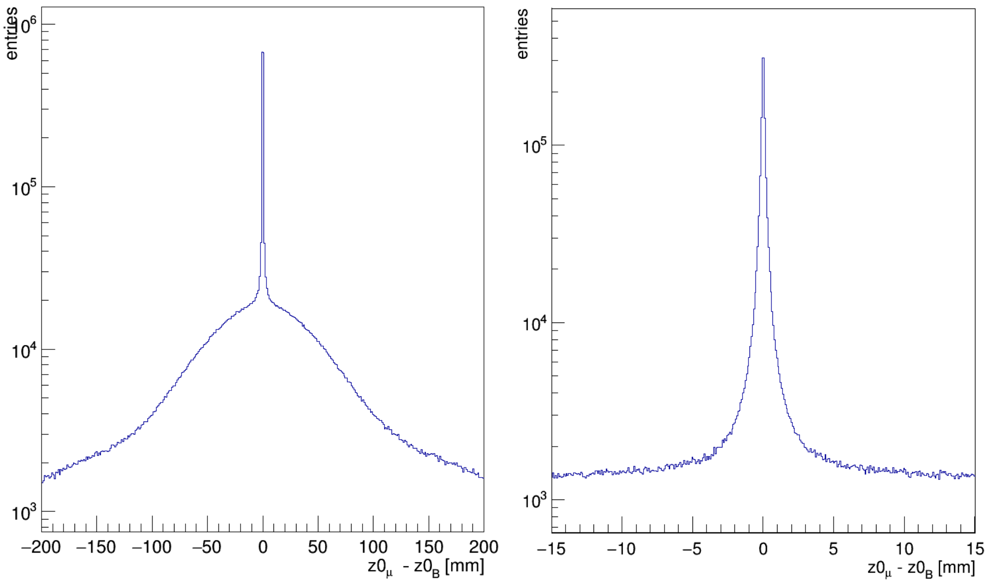

FIGURE 5.5. Left figure shows distribution of Δz, where Δz is impact parameter of muon trajectory relative to the primary vertex identified in the event using B-signal candidate. The narrow peak represents the signal muon candidates and the area under this peak the pile-up background. Right figure is the magnification of the central part.

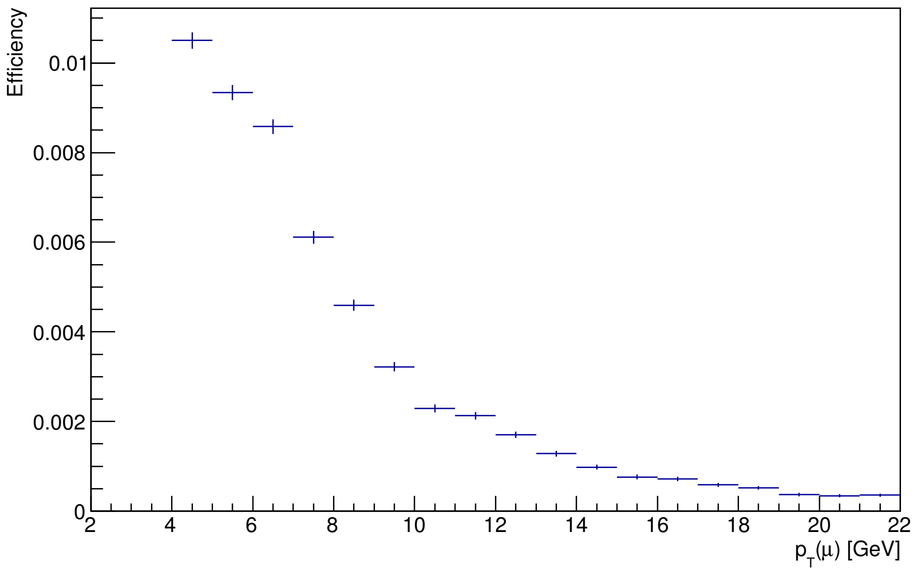

FIGURE 5.6. The muon efficiency dependence on the muon transversal momentum. The errors are statistical and they were calculated as the sum of the square of weights per bin.

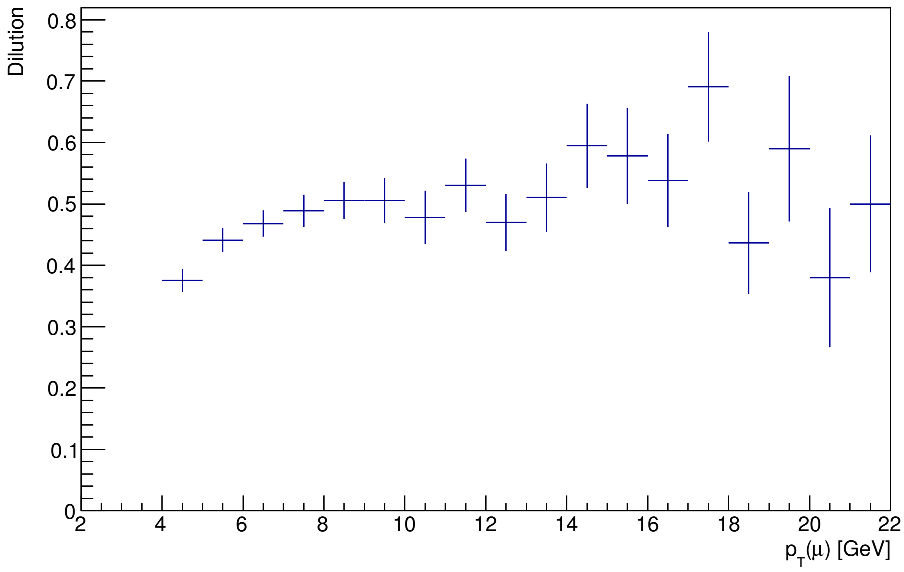

FIGURE 5.7. The muon dilution dependence on the muon transversal momentum. The errors are statistical and they were calculated as the sum of the square of weights per bin.

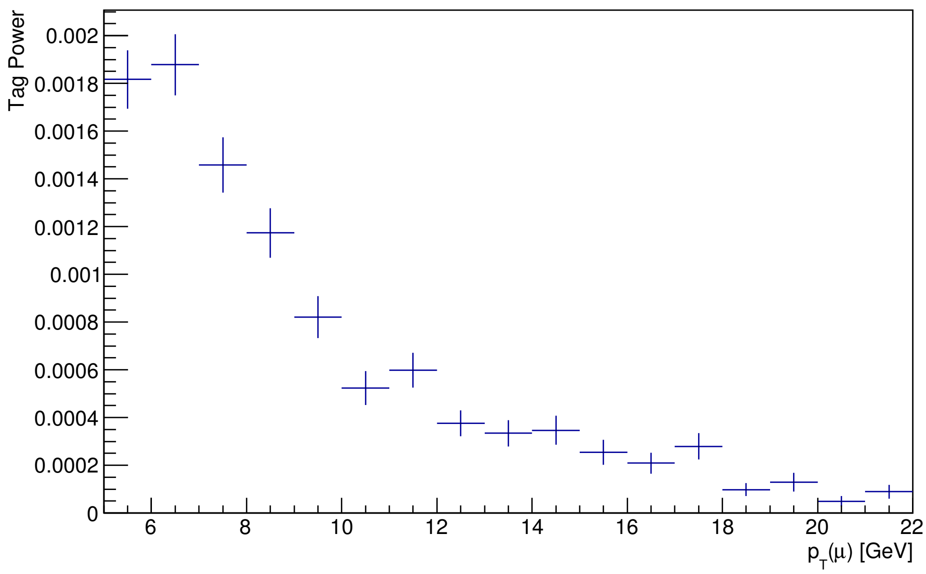

FIGURE 5.8. The muon tag power dependence on the muon transversal momentum. The errors are statistical and they were calculated as the sum of the square of weights per bin.

5.5 Cone Charge Tagging

The cone charge is used for optimization of the tagging performance and it is defined by the equation (5.5). The cone $\Delta R = \sqrt{(\Delta\phi)^2 + (\Delta\eta)^2} < 0.5$ is constructed around selected muon. Only tight muons are used as the leading muon (all cuts are applied on this muon, including the Δz cut) and the tracks of B candidate (and its muons from J/ψ) and kaon are not included in the cone around these muons. No other cuts on track in cone are applied. Sometimes, there is no additional track in the cone around the muon. Then the cone charge has sharp value of ± 1, see Figure 5.9

The tag power in the cone charge case is

$$P_{tag} = \sum_i (\epsilon_{tag})_i \left(2P_i(B^+|Q_i) - 1\right)^2, \tag{5.9}$$

where $P_i(B^+|Q_i)$ is the cone charge for B^+. The B^- tag power can be calculated in the same way and it is equal to the B^+ tag power, so there is no need to repeat it.

Both data streams live and delayed were tested. It is expected, that the results for the live stream would have larger tag power, similarly to the results for the single muon tag power.

5.5.1 All Qualities of Muons

Firstly, the tag power for qualities of muons were calculated, see Table 5.7. It allows to omit the calculation of tag power for cones around medium, loose and very loose muons due to its small tag power. However, the tag power using the cone charge method has smaller tag power than the single muon has (see Table 5.6 top). This implies, that there are some polluting tracks in the cone, which decrease the tag power, or the coefficient κ can be different than defined in the cone charge.

	tight	**medium**	**loose**	**very loose**
$\mathbf{P_{tag}}$ (%)	0.98 ± 0.03	0.020 ± 0.002	0.026 ± 0.003	0.038 ± 0.004

TABLE 5.7. Tag power P_{tag} of cone charge for all qualities of leading muon. The cone charge method on data of release version 20.7 was used to obtain these results.

5.5.2 κ Variation

The stability of the cone charge with respect to variation of the power coefficient κ in (5.5) was also tested. In previous analysis, κ was set to 1.1 (it provided the larger tag power), so the κ variation test was performed around this value. Results for both data streams can be seen in Table 5.8. Despite the fact that there are some small deviations or both streams, the tag power for different κ is stable within the statistical uncertainty and the value $\kappa = 1.1$ is used in next steps of the analysis.

κ	**1.00**	**1.05**	**1.10**	**1.15**	**1.20**
$\mathbf{P_{tag}}$ (%)	0.98 ± 0.01	0.98 ± 0.02	0.98 ± 0.01	0.98 ± 0.03	0.98 ± 0.02
$\mathbf{P_{tag}}$ (%)	1.31 ± 0.02	1.31 ± 0.02	1.312 ± 0.02	1.32 ± 0.03	1.32 ± 0.01

TABLE 5.8. Tag power P_{tag} for κ variation in (5.5). Results for live stream are shown on the first line, results for delayed stream on the second one.

5.5.3 Δz and ΔR variation

Secondary particles created in collisions at the centre of the ATLAS detector pass through the detector layers. This passage can result in interaction of these particles with detector, creating secondary particles. In addition particles created in B meson decay (kaons, muons, electrons) hit some layers of the detector creating daughter particles. This can cause the pollution of the cone charge created around the muon.

ΔR	**no cut**	**< 0.1**	**< 0.2**	**< 0.3**	**< 0.4**	**< 0.5**
$\mathbf{P_{tag}}$ (%)	0.98 ± 0.01	1.01 ± 0.02	1.14 ± 0.03	1.21 ± 0.01	1.23 ± 0.02	1.25 ± 0.02
$\mathbf{P_{tag}}$ (%)	1.31 ± 0.02	1.37 ± 0.02	1.45 ± 0.01	1.51 ± 0.02	1.54 ± 0.03	1.54 ± 0.02

TABLE 5.9. The ΔR cut between B candidate and tracks in the muon cone. The $\Delta R < 0.2$ cut signifies that all tracks in the cone of $\Delta R < 0.2$ around the B candidate are excluded from the cone around the leading muon. Results for delayed stream results are shown on the first line, results for live stream on the second one.

To reduce this pollution, the cone around the B meson is constructed and every particle in this cone in the cone around the leading muon is not included. The size of the cone around B candidate is varied. These tracks are excluded from the cone around muon (still defined as $\Delta R < 0.5$) in order to get the right tracks in the cone and the larger tag power. The results (again for both streams) are shown in Table 5.9. The tag power rises with increasing number of tracks excluded from the cone around the leading muon. Larger cuts were not tested in order to have sufficient number of tracks in the muon cone. It is also expected that the tag power for larger cuts is smaller than results shown

Δz	**no cut**	$>$ **7** mm	$>$ **6** mm	$>$ **5** mm	$>$ **4** mm	$>$ **3** mm
$\mathbf{P_{tag}}$ (%)	0.98 ± 0.01	1.04 ± 0.02	1.04 ± 0.02	1.04 ± 0.03	1.06 ± 0.02	1.06 ± 0.02
$\mathbf{P_{tag}}$ (%)	1.31 ± 0.02	1.31 ± 0.03	1.31 ± 0.02	1.31 ± 0.02	1.32 ± 0.03	1.32 ± 0.03

TABLE 5.10. The Δz cut between B candidate and tracks in the muon cone. The $\Delta z > 4$ mm cut means that all track with distance to B candidate bigger than 4 mm are excluded from the cone around the leading muon. Results for delayed results are shown on the first line, results for live stream on the second one.

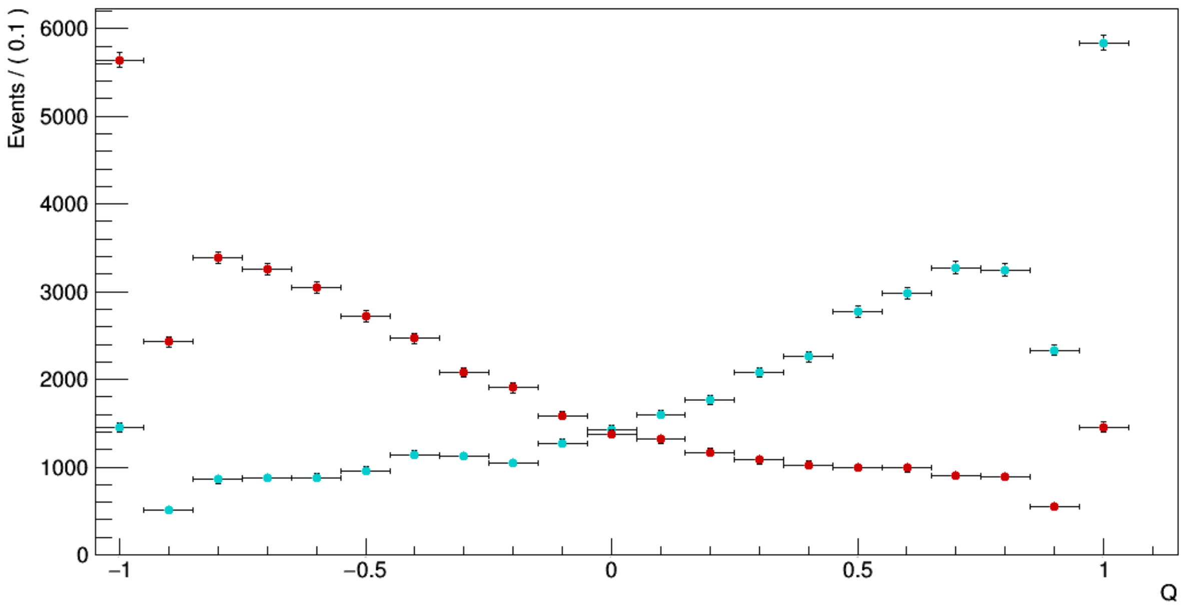

FIGURE 5.9. The muon cone charge distribution (red B^+, blue B^-) for $\Delta R < 0.4$ (all tracks in the cone of $\Delta R < 0.4$ around the B candidate are excluded from the cone around the leading muon).

in Table 5.9.

The second applied cut is the Δz cut (the longitudinal impact parameter of a track trajectory relative to the primary vertex identified in the event using B-signal candidate). It should help to find and include only those tracks, which are close to the B candidate. The situation is similar to the ΔR cut, the tag power rises with decreasing number of tracks in the muon cone, as is shown in Table 5.10. Again, larger cuts were not tested in order to have sufficient number of track in the muon cone.

To conclude, the κ variation does not help as much as needed. Both ΔR and Δz cuts help, the tag power is increased with any of these cuts applied.

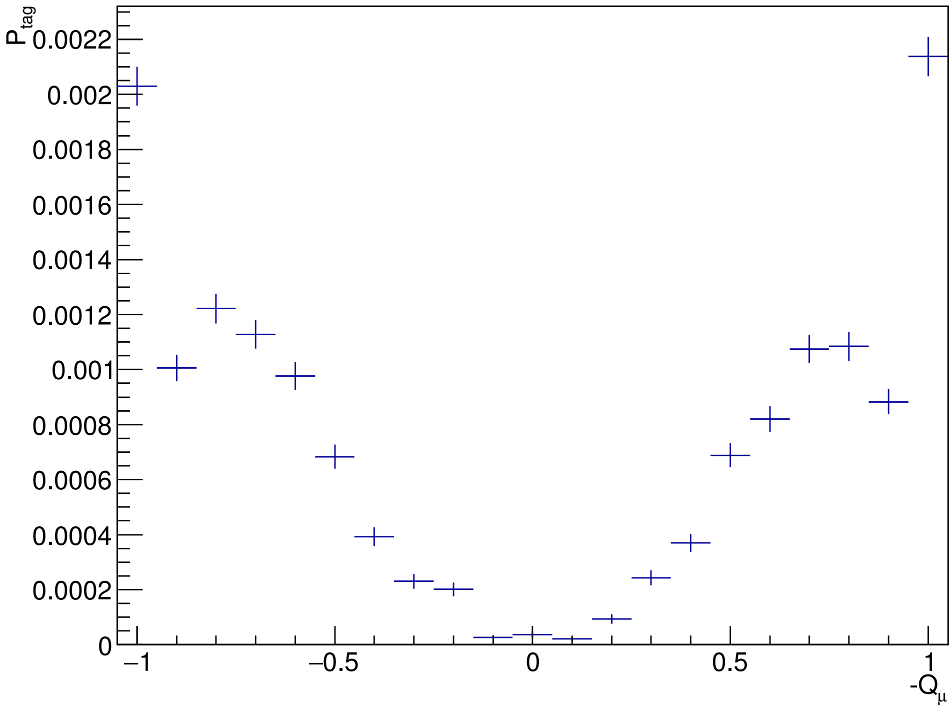

FIGURE 5.10. The tag power distribution with dependence on cone charge for $\Delta R < 0.4$ (all tracks in the cone of $\Delta R < 0.4$ around the B candidate are excluded from the cone around the leading muon).

The previous table contain results only for data taken in 2016, the 2015 tagging variables were tested by other members of the analysis group. Merging both delayed and live streams together (with removal of event data overlap) for both years 2015 and 2016 and applying both cuts together, $|\Delta z| < 3$ mm and $\Delta R < 0.5$ between tracks in muon cone and the B candidate, the final tag power was found to be $P_{tag} = (0.91 \pm 0.01)$ %, where the error denotes statistical uncertainty. The lower value of the tag power is caused by significantly larger statistical sample in the delayed stream and also small tagging power in 2015, see Table 5.11.

5.6 Tag Probability

The main purpose of the study of $B^{\pm} \to J/\psi K^{\pm}$ is to get the probability distribution for tagging. This distribution is used in the core analysis as the calibration distribution.

	$\epsilon_{\mathbf{tag}}$ (%)	$\mathbf{D_{tag}}$ (%)	$\mathbf{P_{tag}}$ (%)
2015	3.03 ± 0.04	48.68 ± 0.07	0.72 ± 0.03
2016	4.00 ± 0.02	49.75 ± 0.03	0.98 ± 0.01
2015+2016	3.81 ± 0.02	48.92 ± 0.04	0.91 ± 0.01

TABLE 5.11. The final tag efficiency ϵ_{tag}, dilution D_{tag} and tag power P_{tag} 2015, 2016 and 2015+2016 data. These results were produced using the cuts $|\Delta z| < 3$ mm and $\Delta R < 0.5$ between tracks in muon cone and the B candidate for both data streams together.

The probability of B^+ tagging for each passed event is calculated using the formula

$$P(B|Q) = \frac{P(Q|B^+)}{P(Q|B^+) + P(Q|B^-)} \tag{5.10}$$

where $P(Q|B^+)$ is the cone charge value of the B^+ for the specific event and the $P(Q|B^-)$ is the cone charge value of the B^- for the same event. There is no need to construct the probability distribution function of B^- tagging, because these two probabilities are related by $P(\bar{B}|Q) = 1 - P(B|Q)$.

The tag probability has been produced separately for muons with at least one additional track in a cone (continuous part of the tag probability) and for a muon without additional tracks in the cone (single-track part). The continuous part is fitted with the third order polynomial function and the sigle-track part is fitted with the sum of two constant functions (see Figure 5.11). The fitted function are then used as the calibration curve for transferring the B_s^0 cone charge into the B_s^0 tag probability.

Electrons, jets and low-p_{T} muons are used for the flavour tagging in the physical analysis in addition to muons discussed in this thesis. The calculation of the efficiency, dilution, tag power and the tag probability of jets and low-p_{T} muons as carried out by other members of analysis group as well as the complete electron tagging analysis. My task was to fit the low-p_{T} and jet calibration distributions and apply them for transferring the B_s^0 cone charge into the B_s^0 tag probability in a similar way as for the tight muon. The low-p_{T} muon calibration distribution is fitted with the first order polynomial function (continuous part) and with the sum of two constant function(single-track part). The jets calibration distribution is fitted with the third order polynomial function (continuous part) and with the sum of two constant functions (single-track part). All plots are in Figure 5.11.

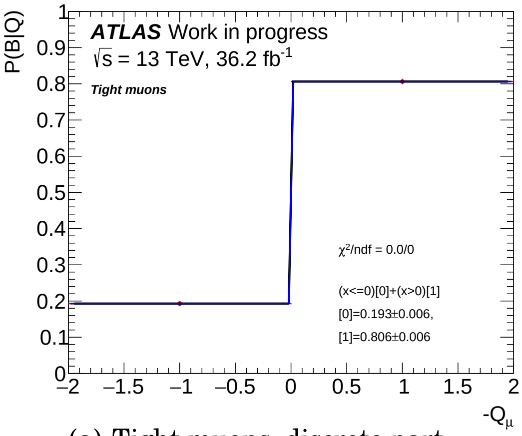

(a) Tight muons, discrete part.

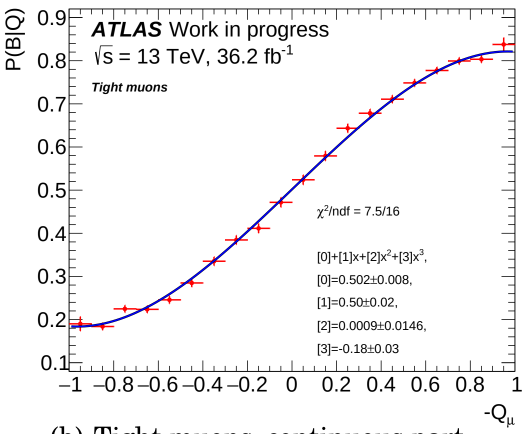

(b) Tight muons, continuous part.

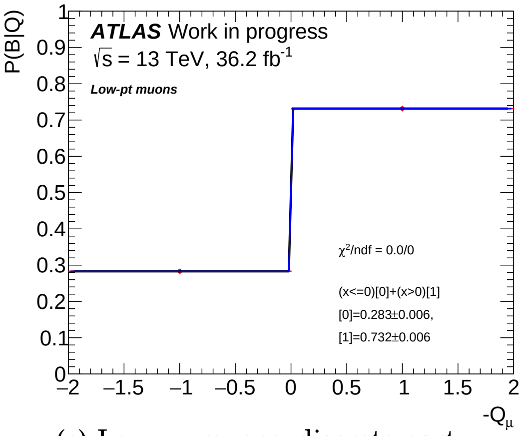

(c) Low-p_{T} muons, discrete part.

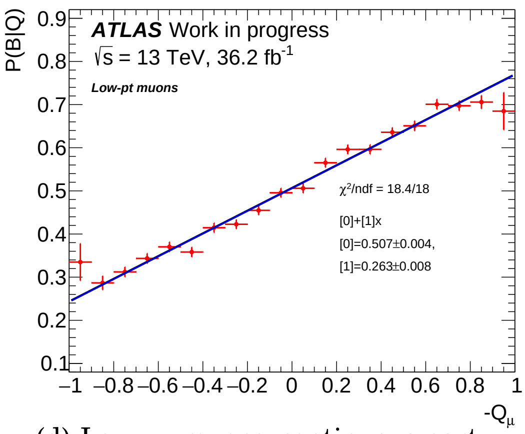

(d) Low-p_{T} muons, continuous part.

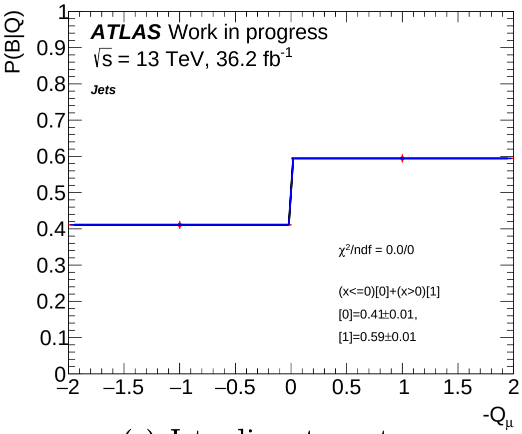

(e) Jets, discrete part.

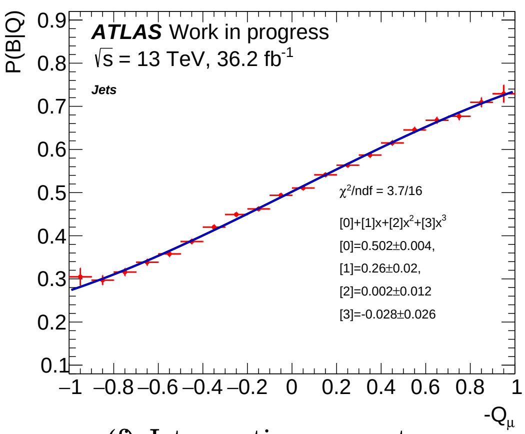

(f) Jets, continuous part.

FIGURE 5.11. B^{+} tag probability distribution for different tag method. The tight muon and jet continuous part fitted with third order polynomial function, low-p_{T} muon continuous part fitted with linear function.

5.7 B^+ Tag Probability Systematics

There are two categories of the measurement uncertainty - the statistical and the systematic contribution. The statistical uncertainty is given by the size of the $B^\pm \to J/\psi K^\pm$ sample and it is included in the statistical uncertainty of the tagging variable and the tag probability distribution.

The systematic contribution is given by the precision of the tagging calibration. This precision is estimated by varying the model used to parametrize the calibration distribution. Also, each point of the calibration distribution was moved up and down by the bin statistical uncertainty. Two calibration distributions (lower and upper) are fitted by the defaults fit function. These fits are included into the set of alternative calibration curves. For tight muon calibration, the third order polynomial function is used as the default parametrisation and several alternative functions are used for the systematics. The alternatives used are: functions from statistical test (lower and upper), a linear function, a fifth-order polynomial, a sinus function or two third-order polynomials describing the positive and negative regions that share the constant and linear terms but have independent quadric and cubic terms. The largest difference (upper and lower - see Figure 5.12) is then used as the calibration curve for the main B_s^0 fit, giving the systematic uncertainty of the fitted parameters. The alternative fits are presented in the appendix A, Figure A.1.

The situation for low-p_{T} muons and jets is similar to the tight muon. The linear function (low-p_{T} muons) and the third order polynomial function (jets) are set as the default parametrisation. The alternative functions are linear function, cubic function, fifth order polynomial function and sinus function. The total systematic uncertainty is also shown in Figure 5.12 for both low-p_{T} muon nad jets. The alternative fits are presented in the appendix A, Figures A.2 and A.3.

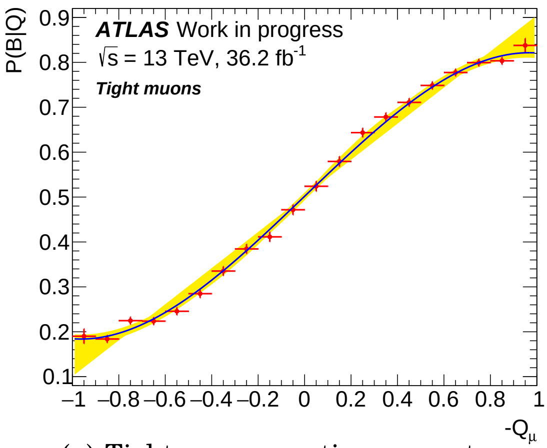

(a) Tight muons, continuous part.

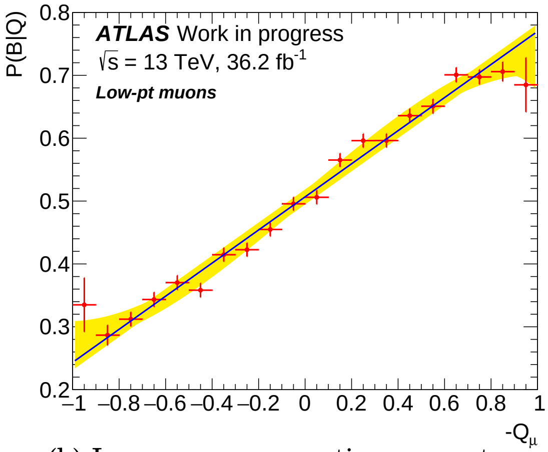

(b) Low-p_T muons, continuous part.

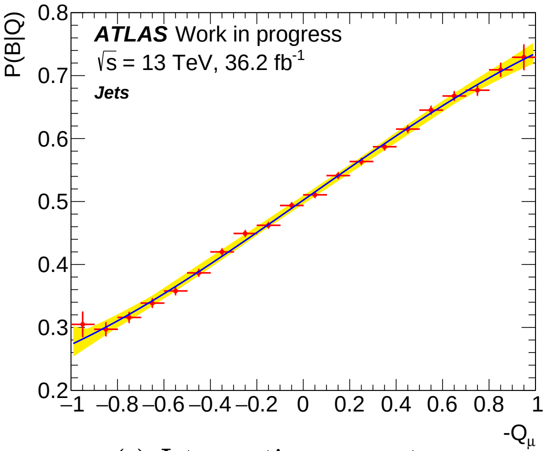

(c) Jets, continuous part.

FIGURE 5.12. The probability distribution with dependence on the tight muon cone-charge (cone-charge directly equal to +1 or -1 removed) with systematic uncertainty (yellow area).

CHAPTER 6

Muon Tagging in the Measurement of the CP Violating Phase ϕ_s in the $B_s^0 \to J/\psi\phi$ Channel

A $B_s^0 \to J/\psi\phi$ channel is expected to be sensitive to the physics beyond the Standard Model. The CP violation phase can be measured together with decay width $\Gamma_s = (\Gamma_L + \Gamma_H)/2$ and decay width difference $\Delta\Gamma$ (see chapter 2 for further details). This analysis provides a measurement of the $B_s^0 - \overline{B}_s^0$ decay parameters using the $36.2\,\text{fb}^{-1}$ of LHC $p-p$ data recorded by the ATLAS detector during 2015 and 2016 at the centre-of-mass energy $\sqrt{s} = 13\,\text{TeV}$. The flavour tagging calibrations from the previous chapter (by tight muons, low-p_T muons, jets and electrons) is used for distinguish between the initial B_s^0 and $\overline{B}_s^0$ states. In next sections, both initial states are noted as B_s^0 (if not denoted differently).

6.1 Data Selection

Candidate B_s^0 events are selected by fitting the tracks for each combination of $J/\psi \to \mu\mu$ and $\phi \to K^+K^-$ to a common vertex. Kaons emerging from ϕ decay must be oppositely charged particles with transversal momentum $p_\text{T}(K^\pm) > 1\,\text{GeV}$, pseudorapidity $|\eta| < 2.5$ and the invariant mass of the kaons must fall between $1.0085 < m(K^+K^-) < 1.0305\,\text{GeV}$. J/ψ must decay into two oppositely charged muons with three different invariant mass ranges according to the pseudorapidity of muons. When both muons have $|\eta| < 1.05$, the muon invariant mass must fall between 2.959 GeV and 3.229 GeV. When both muons have $1.05 < |\eta| < 2.5$, the dimuon invariant mass region is wider with $2.852 < m(\mu^+\mu^-) < 3.332$ GeV. The last option is when one muon has $|\eta| < 1.05$ and the other muon has $1.05 < |\eta| < 2.5$, then the dimuon invariant mass range is defined to be $2.913 < m(\mu^+\mu^-) < 3.273$ GeV. Each of the four tracks is required to have at least one hit in the pixel detector, at least four hits in the silicon microstrip detector and in addition muons are required to have at least one hit in the Muon Spectrometer. If there is more than one B_s^0 candidate per event, the candidate with lowest χ^2/d.o.f is selected. In total, 1548122 B_s^0 candidates are selected in the mass range of $5.150 < m(B_s^0 \to J/\psi\phi) < 5.650$ GeV.

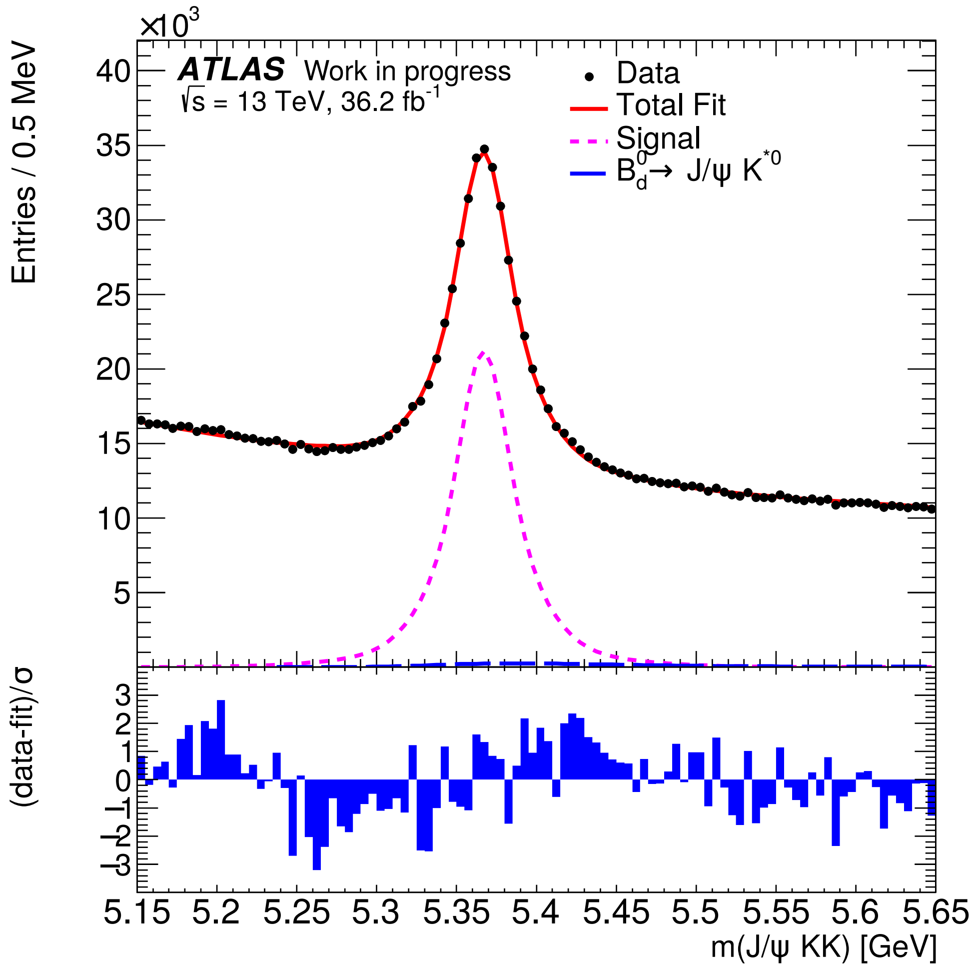

FIGURE 6.1. The invariant mass distribution of B_s^0 candidates that passed the selection criteria. The overall result of the fit is given by the red curve, the signal component is given by the magenta curve and the contamination of $B_d^0 \to J/\psi K^{\star 0}$ is given by the blue curve.

6.2 B_s^0 Mass Fit

An unbinned maximum likelihood fit is performed using roofit on the selected data to fit the invariant mass of B_s^0 in the exclusive channel. The signal part is described by three Gauss functions with the same mean. The background is defined by a combination of exponential constant function to describe the overall background and by a Gauss function to describe $B_d^0 \to J/\psi K^{\star 0}$. Then, the total likelihood function is defined as a combination of the signal and background probability density functions similarly to the $B^{\pm}$ case presented in previous chapter

$$\begin{aligned} PDF = & f_{sig}[f_{gauss1}G(\mu,\sigma_1) + f_{gauss2}G(\mu,\sigma_2) + (1 - f_{gauss1} - f_{gauss2})G(\mu,\sigma_3)] + \\ & + (1 - f_{sig})[f_{bck1}E(\lambda) + (1 - f_{bck1})G(\mu_{bd},\sigma_{bd})], \end{aligned} \tag{6.1}$$

where G are Gauss functions with the same mean μ and different widths σ_1, σ_2 and σ_3, $E(\lambda)$ is the exponential function with the slope λ and $G(\mu_{bd},\sigma_{bd})$ with mean μ_{bd} and σ_{bd} describing the contamination from $B_d^0 \to J/\psi K^{\star 0}$ candidates (this contribution is obtained from the B_d^0 Monte Carlo study and is set to be constant in this mass fit). The coefficients f_{sig}, f_{gauss1}, f_{gauss2} and f_{bck1} are the scale factors of these functions. All parameter values are shown in Table 6.1 and the final B_s^0 mass plot is shown in Figure 6.1. The signal-to-background fraction f_{sig} is crucial in the section, where is used in the B_s^0 tag probability fitting.

μ [MeV]	5366.97 ± 0.06	λ [MeV]	0.43 ± 0.02
σ_1 [MeV]	26.1 ± 0.8	f_{bck1}	0.60 ± 0.04
σ_2 [MeV]	54 ± 2	μ_{bd} MeV	5386.4
f_{gauss1}	0.71 ± 0.02	σ_{bd} [MeV]	51.54
f_{gauss2}	0.72 ± 0.02	f_{sig}	0.1521 ± 0.0005
σ_3 [MeV]	12.8 ± 0.3		

TABLE 6.1. Fitted parameters of the total probability density function (6.1).

6.3 Using Tag Information in the B_s^0 Fit

The initial B_s^0 or $\overline{B}_s^0$ flavour determination is improved by the opposite side flavour tagging (described in the section 2.3.1). The selected tagging methods are tight and low-p_{T} muons, electrons and jet. The cone charge is defined as

$$Q_\mu = \frac{\sum_i^{Ntracks} q_i (p_{\mathrm{T}})_i}{\sum_i^{Ntracks} (p_{\mathrm{T}})_i} \tag{6.2}$$

Tag method	Signal	Background
Tight μ	0.0385 ± 0.0009	0.0331 ± 0.0001
Medium e	0.0163 ± 0.0005	0.01289 ± 0.00009
Low-pt μ	0.0274 ± 0.0008	0.0256 ± 0.0001
Jets	0.135 ± 0.002	0.1084 ± 0.0003
Untagged	0.782 ± 0.004	0.8200 ± 0.0007

TABLE 6.2. Table summarizing the relative fractions of signal and background events tagged using the different tag method. The fractions include both the continuous and discrete contributions. Only statistical errors are quoted.

where q_i is charge of the track, $\kappa = 1.1$ and the sum is performed over the reconstructed Inner Detector tracks within a cone $\Delta R = \sqrt{(\Delta\phi)^2 + (\Delta\eta)^2} < 0.5$ around the tagging particle. The cone charge distribution for tight muons is in Figure 6.2.

The continuous part of cone charge distribution and discrete part (the cone charge with values directly equal to ± 1 are treated separately). Unfortunately, the tagging particle do not exists (was not reconstructed) for all B_s^0 candidates, approximately 80% of events are untaged for both signal and background. The relative fractions of tagged events (for different tag method) are presented in Table 6.2.

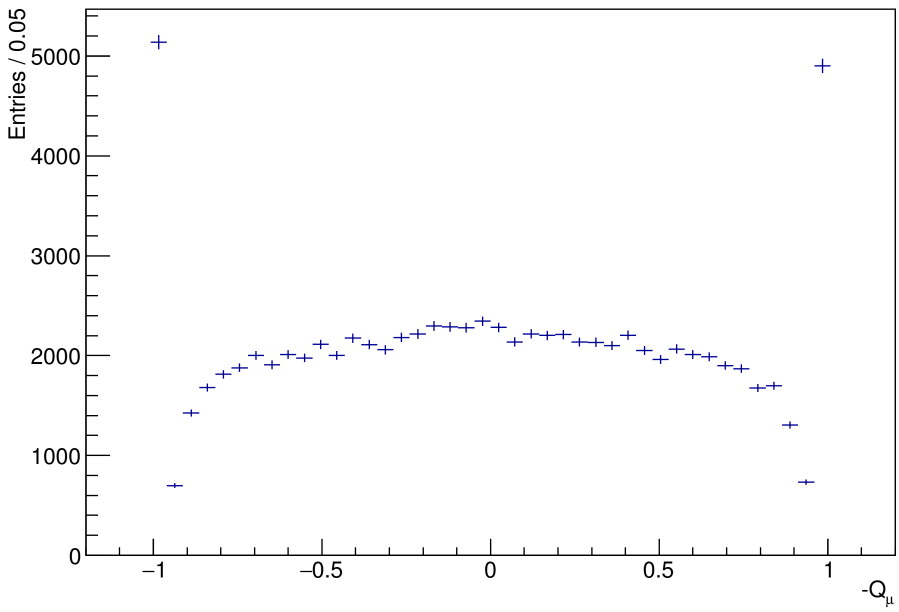

FIGURE 6.2. The cone charge distribution for tight muons.

6.3.1 Continuous Components of Tag Probability Distribution

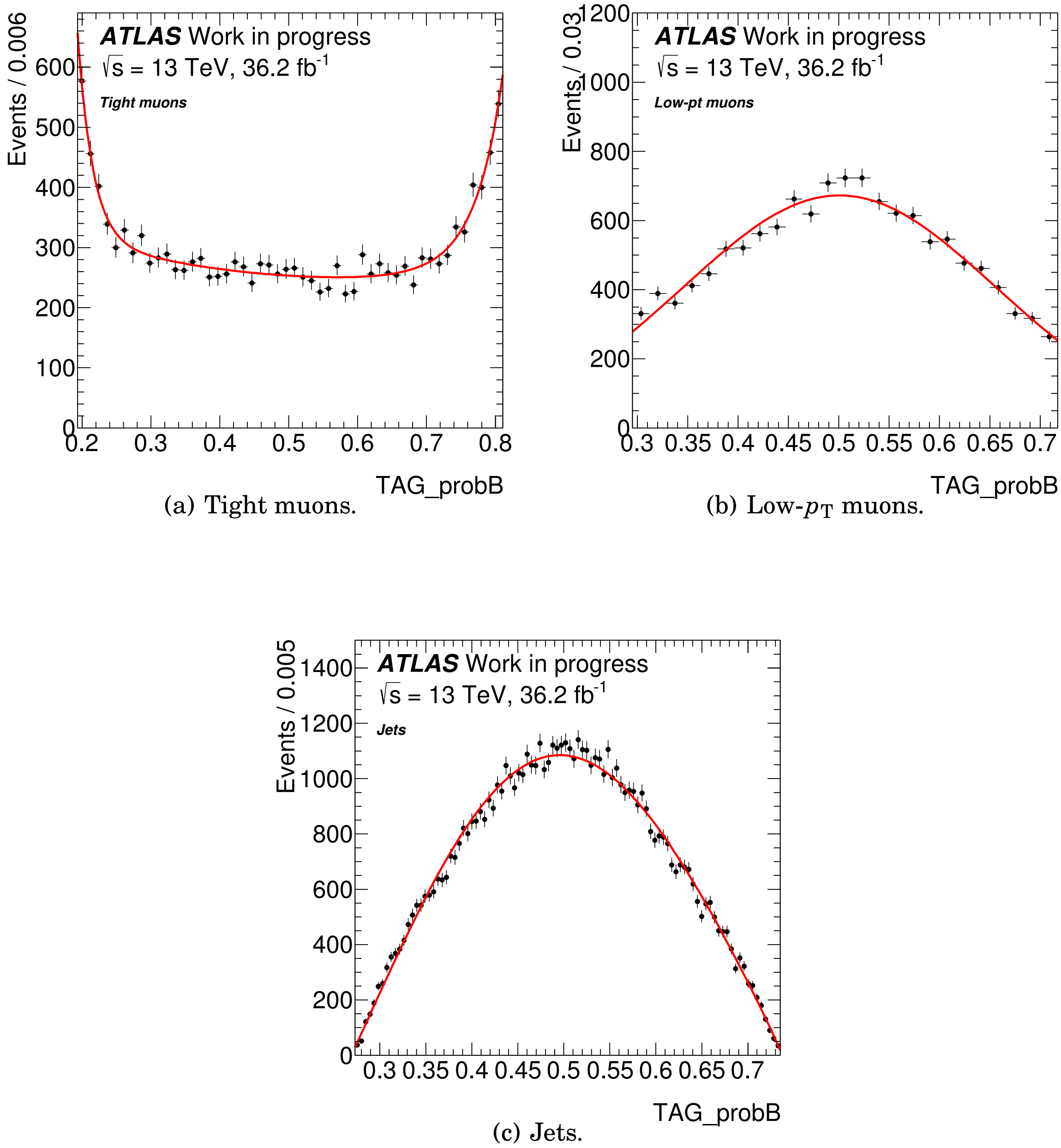

(a) Tight muons.

(b) Low-p_{T} muons.

(c) Jets.

FIGURE 6.3. B_s^0 sideband tag probability distribution for different tag method.

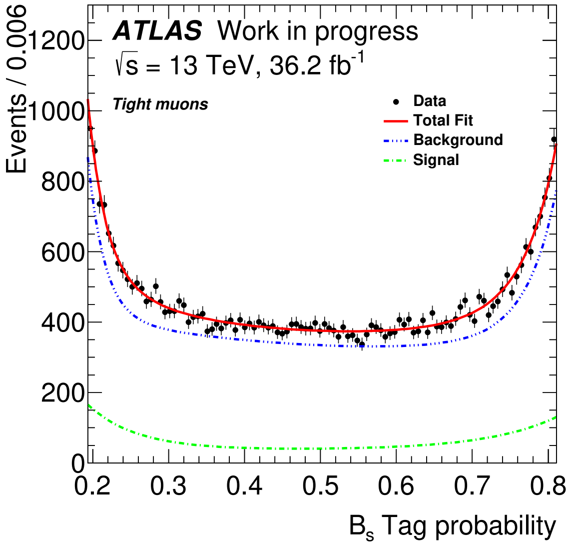

(a) Tight muons.

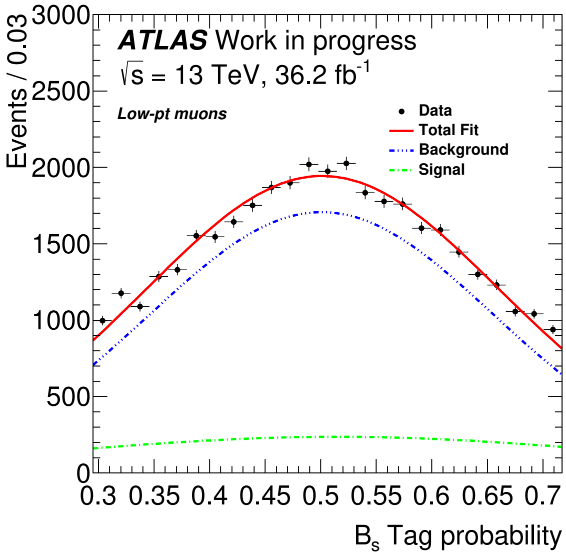

(b) Low-p_{T} muons.

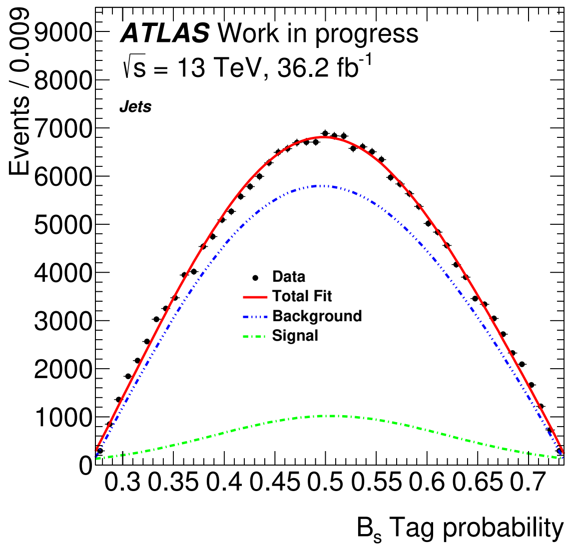

(c) Jets.

FIGURE 6.4. B_s^0 tag probability distribution for different tag method.

The aim of producing the B^+ tag probabilities (calibration curves) is to transform the continuous part of the B_s^0 cone charge distribution into the B_s^0 tag probabilities (separately for each tagger).

The background part of the B_s^0 tag probability is described by the sideband data, with mass in two regions $5.150 < m(B_s^0) < 5.317$ GeV and $5.417 < m(B_s^0) < 5.650$ GeV. Different functions for fitting these sideband distributions are used for different tagging method (different taggers). The sum of two exponential and the second order polynomial function are used for tight muons, the Gaussian function is used for low-p_T muons and eighth order polynomial function describes the jets sideband data. Unbinned maximum-likelihood fits to data are used in all three cases. The sideband tag probabilities distributions with fits are in Figure 6.3. The electron tag probability was accomplished by another member of the analysis group.

In the next step, the whole B_s^0 tag probability distributions are fitted. The parameters of the background (sideband) fits are fixed to the values obtained from these fits and the signal-to-background ratio obtained from the mass fit is also fixed and used, so only signal component of each probability density function can varied in the overall fit. The signal parts are also different for different tag method. The sum of two exponential and one constant function is used for tight muons and the Gaussian function is used for both low-p_T muons and jets. The tag probabilities distributions with fits are in Figure 6.4. These fit serves as the Punzi tag probabilities (described in the appendix B) in the B_s^0 maximum likelihood fit described in the next section.

6.3.2 Discrete Components of Tag Probability Distribution

The case with only single track in the cone, giving the cone charge +1 or -1, is treated in a different way than the continuous part. The fraction of events with cone charge +1 or -1 (f_{+1} or f_{-1}) is determined for each signal and background contribution using the sideband subtraction. The remaining fraction of events, $1 - f_{+1} - f_{-1}$, constitute the continuous part of the distributions. These fractions f_{+1} and f_{-1} play roles of the Punzi terms in the B_s^0 maximum likelihood fit. The fractions f_{+1} and f_{-1} obtained for signal and background events and for the different tag methods are shown in Table 6.3.

6.4 Maximum Likelihood Fit

An unbinned maximum likelihood fit is performed in order to get the values estimates of the parameters of the $B_s^0 \to J/\psi(\mu^+\mu^-)\phi(K^+K^-)$ decay. The fit uses the B_s^0 mass m, the proper decay time t with its resolution σ_t, transversity angles described in Figure 2.3 and the B_s^0 tag probability. The likelihood function is a combination of signal and

Tag Method	Signal		Background	
	f_{+1}	f_{-1}	f_{+1}	f_{-1}
Tight μ	0.073 ± 0.005	0.081 ± 0.006	0.051 ± 0.001	0.053 ± 0.001
Medium e	0.18 ± 0.01	0.16 ± 0.01	0.159 ± 0.003	0.161 ± 0.003
Low-pt μ	0.120 ± 0.008	0.125 ± 0.008	0.074 ± 0.001	0.080 ± 0.001
Jets	0.038 ± 0.002	0.039 ± 0.002	0.0324 ± 0.0004	0.0323 ± 0.0004

TABLE 6.3. Fractions of events f_{+1} and f_{-1} with cone charge +1 or -1 for signal and background and for different tag methods separately. Only statistical uncertainties are quoted.

background probability density functions,

$$\begin{aligned} L = \sum_{i=1}^{N} \ln \Big[& f_s F_s \left(m_i, t_i, \sigma_{t_i}, \Omega_i, p_{\mathrm{T}_i}, P(B|Q)\right) + f_s f_{B^0} F_{B^0} \left(m_i, t_i, \sigma_{t_i}, \Omega_i, p_{\mathrm{T}_i}, P(B|Q)\right) \\ & + f_s f_{\Lambda_b} F_{\Lambda_b} \left(m_i, t_i, \sigma_{t_i}, \Omega_i, p_{\mathrm{T}_i}, P(B|Q)\right) \\ & + \left(1 - f_s(1 + f_{B^0} + f_{\Lambda_b})\right) F_{bkg} \left(m_i, t_i, \sigma_{t_i}, \Omega_i, p_{\mathrm{T}_i}, P(B|Q)\right) \Big], \end{aligned} \tag{6.3}$$

where N is number of events, f_s is the signal fraction, f_{B^0} and f_{Λ_b} are the fraction of B_d and Λ_b wrongly identified as the B_s^0 candidate (these fractions are obtained from the Monte Carlo analysis and are set to be constant in this fit). The F_s, F_{B^0}, F_{Λ_b} and F_{bkg} are the probability density function describing the signal, B_d^0 background, Λ_b background and other background distributions.
The signal contribution is modelled with the function

$$\begin{aligned} & F_s \left(m_i, t_i, \sigma_{t_i}, \Omega_i, p_{\mathrm{T}_i}, P(B|Q)\right) = \\ & \quad = P_s(m_i) \cdot P_s(\Omega_i, t_i, P(B|Q), \sigma_{t_i}) \cdot P_s(\sigma_{t_i}) \cdot P_s(P(B|Q)) \cdot A(\Omega_i, p_{\mathrm{T}_i}) \cdot P_s(p_{\mathrm{T}_i}), \end{aligned} \tag{6.4}$$

where $P_s(m_i)$ is described by sum of three Gaussian function, $P_s(\sigma_{t_i})$ and $P_s(p_{\mathrm{T}_i})$ are modelled by gamma functions (Punzi terms created by another member of the analysis group), $P_s(P(B|Q))$ is the Punzi term describing the B_s^0 tag probability (green curve in Figure 6.4) and the angular sculpting of the detector and kinematic cuts on the angular distributions is included in the likelihood function $A(\Omega_i, p_{\mathrm{T}_i})$. The probability $P_s(\Omega_i, t_i, P(B|Q), \sigma_{t_i})$ is a joint PDF for the transversity angles and decay time and is described by the function (2.12). This PDF term takes into account the lifetime resolution, so each time element in the function (2.12) is smeared with a Gaussian function. This smearing is performed numerically on an event-by-event basis where the width of the Gaussian function is the proper decay time uncertainty, measured for each

event, multiplied by a scale factor to account for any mis-measurements.
The background PDF is modelled by

$$\begin{aligned} F_{bkg}(m_i,t_i,\sigma_{t_i},\Omega_i,P(B|Q),p_{\mathrm{T}_i}) = \\ = P_b(m_i)\cdot P_b(t_i|\sigma_{t_i})\cdot P_b(P(B|Q))\cdot P_b(\Omega_i)\cdot P_b(\sigma_{t_i})\cdot P_b(p_{\mathrm{T}_i}), \end{aligned} \tag{6.5}$$

where $P_s(\sigma_{t_i})$ and $P_s(p_{\mathrm{T}_i})$ are modelled by gamma functions (Punzi terms created by colleagues in the analysis group), $P_s(P(B|Q))$ is the Punzi term describing the B_s^0 tag probability (blue curve in Figure 6.4), $P_b(m_i)$ is an exponential function with a constant term added, $P_b(t_i|\sigma_{t_i})$ is parametrised as a prompt peak modelled by a Gaussian distribution (modelling the combinatorial background events, which are expected to have reconstructed lifetimes distributed around zero), two positive exponential functions (representing a fraction of longer-lived backgrounds with non-prompt J/ψ, combined with hadrons from the primary vertex) and a negative exponential function (taking into account events with poor vertex resolution). The shape of the background angular distribution, $P_b(\Omega_i)$ describes the detector and kinematic acceptance effects, modelled by Legendre polynomial functions

$$\begin{aligned} Y_l^m(\theta_T) &= \sqrt{(2l+1)/(4\pi)}\sqrt{(l-m)!/(l+m)!}\,P_l^{|m|}(\cos\theta_T), \\ P_k(x) &= \frac{1}{2^k k!}\frac{\mathrm{d}^k}{\mathrm{d}x^k}(x^2-1)^k, \\ P_b(\theta_T,\psi_T,\phi_T) &= \sum_{k=0}^{6}\sum_{l=0}^{6}\sum_{m=-l}^{l}\begin{cases} a_{k,l,m}\sqrt{2}Y_l^m(\theta_T)\cos(m\phi_T)P_k(\cos\psi_T) & \text{where } m>0 \\ a_{k,l,m}\sqrt{2}Y_l^{-m}(\theta_T)\sin(m\phi_T)P_k(\cos\psi_T) & \text{where } m<0 \\ a_{k,l,m}\sqrt{2}Y_l^0(\theta_T)P_k(\cos\psi_T) & \text{where } m=0. \end{cases} \end{aligned} \tag{6.6}$$

The coefficients $a_{k,l,m}$ are adjusted to give the best fit to the angular distributions for events in the B_s^0 mass sidebands (between 5.150 and 5.650 GeV excluding the signal mass region $|(m(B_s^0) - 5.366\,\mathrm{GeV}| < 0.110\,\mathrm{GeV}$).

6.5 Results

Nine physical parameters ($\Delta\Gamma_s$, ϕ_s, Γ_s, $|A_0(0)|^2$, $|A_\parallel(0)|^2$, $\delta_{||}$, $\delta_\perp$, $|A_S(0)|^2$ and δ_S) are employed in the full unbinned maximum likelihood fit. Another parameters in the full fit are signal fraction f_s, terms describing the B_s^0 mass, decay time, decay time uncertainty distributions.
The results with correlation matrix are presented in Tables 6.4 and 6.5, all employed

Parameter	Value	Statistical uncertainty	Systematic uncertainty
$\lvert A_0(0)\rvert^2$	0.549	0.0021	0.0007
$\lvert A_{\parallel}(0)\rvert^2$	0.2125	0.0028	0.0001
$\lvert A_S(0)\rvert^2$	0.135	0.005	0.002
Γ_S [ps^{-1}]	0.664	0.002	0.001
$\Delta\Gamma_s$ [ps^{-1}]	0.1189	0.0069	0.0001
ϕ_S	-0.0785	0.0459	0.008
$\delta_{\parallel}$ [rad]	3.1415	0.0389	0.0001
$\delta_{\perp}$ [rad]	2.6801	0.1436	0.0004
$\delta_{\perp} - \delta_S$ [rad]	-0.0693	0.0170	0.0003

TABLE 6.4. Fitted values for the physical parameters of interest with their statistical and systematic uncertainties.

	$\lvert A_0(0)\rvert^2$	$\lvert A_{\parallel}(0)\rvert^2$	$\lvert A_S(0)\rvert^2$	Γ_S	$\Delta\Gamma_s$	ϕ_S	$\delta_{\parallel}$	$\delta_{\perp}$
$\lvert A_{\parallel}(0)\rvert^2$	-0.33	1						
$\lvert A_S(0)\rvert^2$	0.291	0.039	1					
Γ_S	-0.01	-0.118	0.217	1				
$\Delta\Gamma_s$	0.105	0.08	0.008	-0.296	1			
ϕ_S	-0.001	-0.008	0.008	-0.006	-0.072	1		
$\delta_{\parallel}$	-0.008	0.041	-0.024	-0.012	0.004	0.008	1	
$\delta_{\perp}$	-0.014	0.003	-0.034	-0.009	0.007	-0.005	0.094	1
$\delta_{\perp} - \delta_S$	0.011	-0.01	0.032	0.01	-0.005	0.008	0.006	0.047

TABLE 6.5. Fit correlations between the physical parameters in Table 6.4.

values are in appendix C. The systematic errors are calculated in the section 6.6. Only systematics due to the tag probability functions and terms are included. Other systematic uncertainties have not been calculated yet.

6.5.1 Comparison with Other Measurements

A comparison of results of this analysis with the ATLAS [37], CMS [62] and LHCb [63] Run 1 results is shown in Figure 6.6. Most of of the ATLAS Run 2 results are compatible with other results within 2σ.

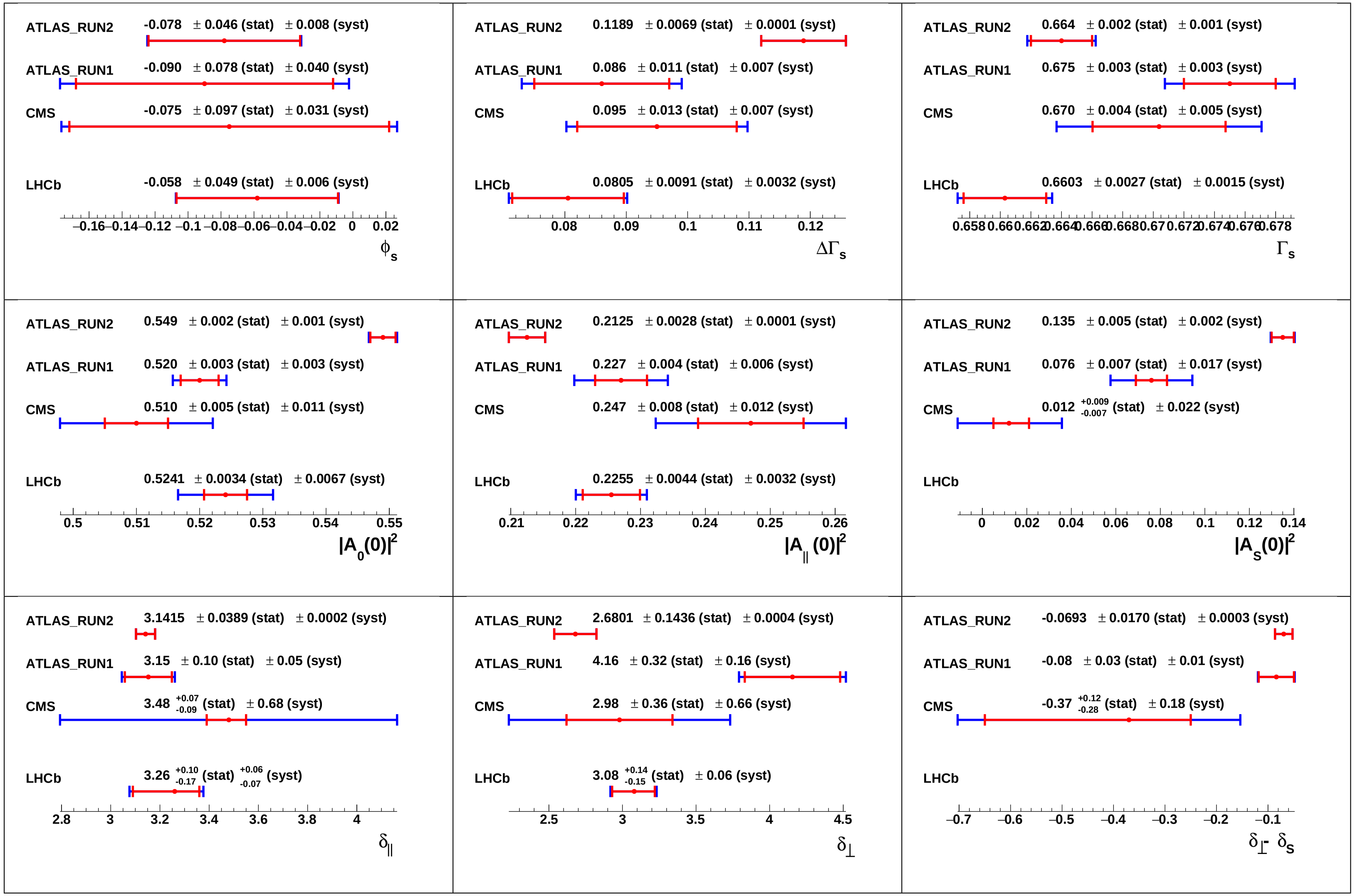

FIGURE 6.6. Comparison of ATLAS Run-2 results with ATLAS Run1 [37], CMS Run1 [62] and LHCb Run1 [63] results. Red are statistical errors and blue are sum of statistical and systematic errors.

The ϕ_s and $\delta_\parallel$ are consistent with other measurements within 1σ. The parameters Γ_s and $\delta_\perp$ are compatible with LHCb and CMS within 1σ and with ATLAS Run1 result within 2σ. However, the parameters $|A_S(0)|^2$ and $|A_0(0)|^2$ seem to not be compatible with other measurement as the difference is larger than 2σ. $|A_{||}(0)|^2$ is compatible with LHCb and ATLAS Run1 within 2σ, but not with the CMS result. The angle $\delta_\parallel$ is consistent with all previous measurement, $\delta_\perp$ with LHCb and CMS and $\delta_\perp - \delta_S$ with ATLAS Run1 results. The reason of the inconsistency can be the instability of the $B_s^0 \to J/\psi\phi$ fit. This will be tested in following steps of the analysis.

6.6 Systematic Uncertainties

The $B_s^0 \to J/\psi\phi$ fit has several contributors to systematic errors. The considered effects are flavour tagging, Inner Detector alignment, angular and acceptance maps, trigger efficiency, choice of mass sidebands, B_d and Λ_b contributions and fit model variations. Only the flavour tagging systematics contribution is discussed in this thesis as the rest is performed by analysis group colleagues. The results of systematics due to the tag probability functions and terms is presented in the next section. The systematic error estimation due to the variation of calibration curve has not been finished yet.

6.6.1 Systematics due to Tag Probability Functions and Terms

The systematics due to the tag probability functions and term takes into account that the tag probability punzi terms (Figure 6.4) are not fitted correctly. The systematic uncertainty is estimated by comparison of the baseline fit and the fit with tag probability punzi terms removed for both signal and background PDF. The impact of this test is shown in Table 6.7.

	Difference	Difference/Error
$\lvert A_0(0)\rvert^2$	0.00068	0.319
$\lvert A_{\lvert\rvert}(0)\rvert^2$	0.00011	0.040
$\lvert A_S(0)\rvert^2$	0.00212	0.453
Γ_S [ps^{-1}]	0.00134	0.719
$\Delta\Gamma_s$ [ps^{-1}]	0.00007	0.010
ϕ_S	0.00840	0.183
$\delta_{\parallel}$ [rad]	0.00017	0.004
$\delta_{\perp}$ [rad]	0.00040	0.003
$\delta_{\perp} - \delta_S$ [rad]	0.00029	0.017

TABLE 6.7. Results of the fitting procedure under the variation of signal and background tag probability terms. The values in the third column are obtained by division of the difference by the statistical uncertainty from Table 6.4.

Conclusion

The thesis is devoted to the study of the properties of the B meson opposite side tagging method. The analysis provides the tag power information about the strength and quality of tagging and establish the calibration curve which is extracted from known $B^{\pm}$ events and is used for transformation of the muon cone charge distribution for B_s^0 into the B_s^0 tag probability distribution. For this purpose the data from the proton-proton collisions with the energy of $\sqrt{s} = 13$ TeV have been used. The data were recorded by the ATLAS apparatus at the LHC during the years 2015 and 2016.

The important part of the thesis is devoted to the data flow and the description of the tagging data analysis. After testing and applying sets of cuts the tag power was found to be $(0.91 \pm 0.01)\%$, what demonstrates the stability of the measurements between Run 2 and Run 1 already presented in [37].

For the tagging calibration of the B_s^0 decays, the B^+ tag probability has been used. The B^+ tag probabilities for different tagging methods (tight muons, low-pt muons and jets) with both statistical and systematic uncertainties are shown in Figure 5.12 of this thesis. Cuts discussed in 5.4 and 5.5 were applied on muons and tracks in the muon cone. Consequently the B_s^0 tag probabilities obtained from the B_s^0 cone charge by applying the calibration curves have been extracted by fitting distributions shown in Figure 6.4). Obtained probabilities are consequently used in the B_s^0 decay fit.

The most interesting observables are weak phase ϕ, Γ_s and $\Delta\Gamma$. Obtained values from the B_s^0 extended likelihood fit are

$$\begin{aligned} \phi_s &= -0.079 \pm 0.046(\text{stat}) \pm 0.008(\text{syst}), \\ \Gamma_s &= 0.664 \pm 0.002(\text{stat}) \pm 0.001(\text{syst}), \\ \Delta\Gamma &= 0.1189 \pm 0.0069(\text{stat}) \pm 0.0001(\text{syst}). \end{aligned} \tag{6.7}$$

These results are compatible with previous ones presented in [37] within 2σ.

Quoted systematic errors come from variation of tag probability functions and terms. The calculation of further systematic uncertainties will be subject of future analysis.

APPENDIX A

B^+ Tag Probability Distributions Fits

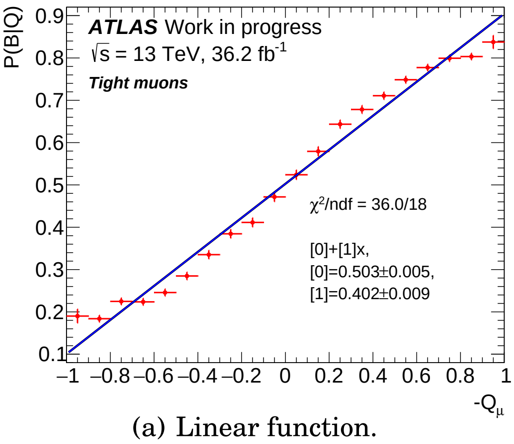

(a) Linear function.

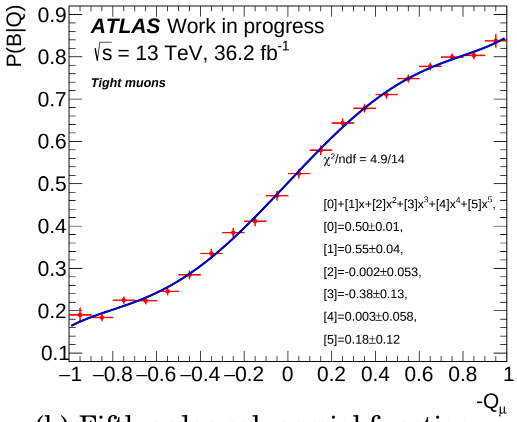

(b) Fifth order polynomial function.

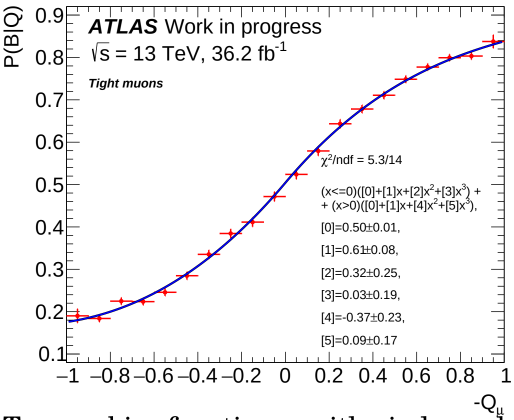

(c) Two cubic functions with independent quadric and cubic terms.

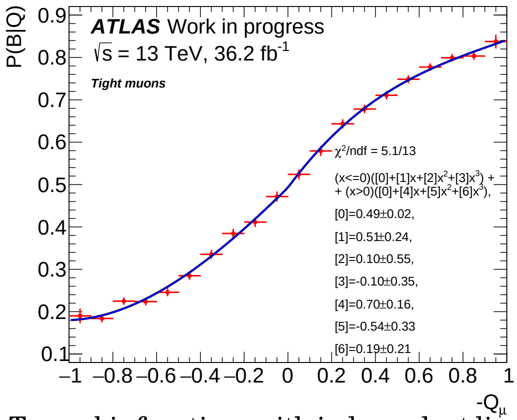

(d) Two cubic functions with independent linear, quadric and cubic terms.

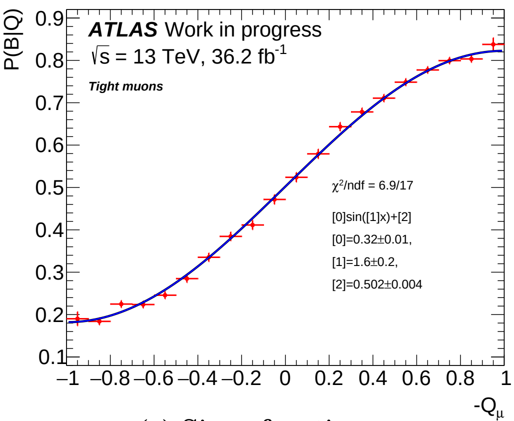

(e) Sinus function.

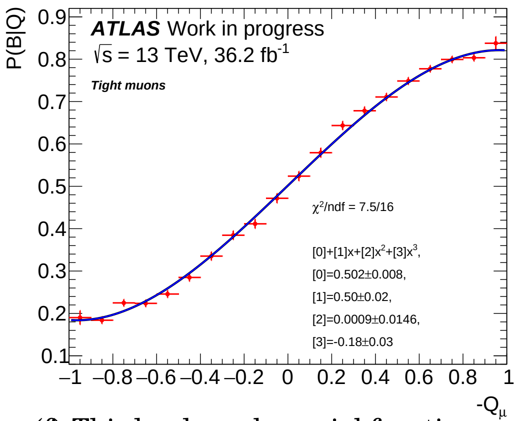

(f) Third order polynomial function.

FIGURE A.1. Alternative parametrisation of the B^+ tag probability distribution for tight muons.

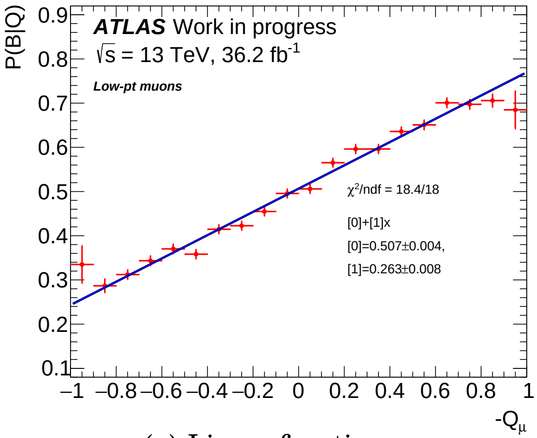

(a) Linear function.

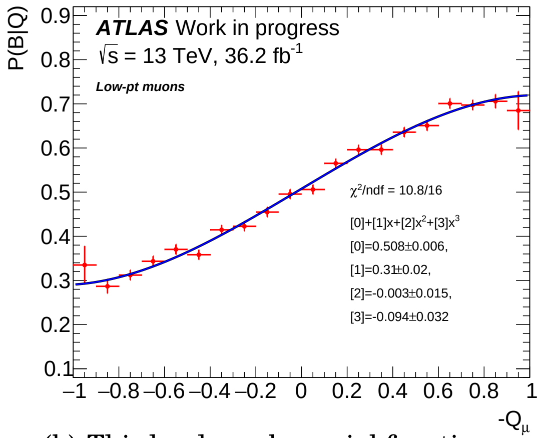

(b) Third order polynomial function.

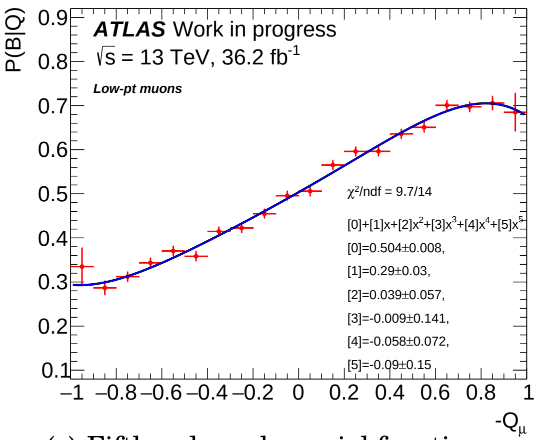

(c) Fifth order polynomial function.

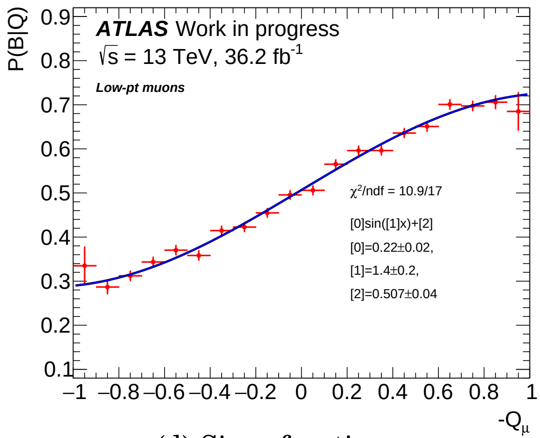

(d) Sinus function

FIGURE A.2. Alternative parametrisation of the B^+ tag probability distribution for low-p_T muons.

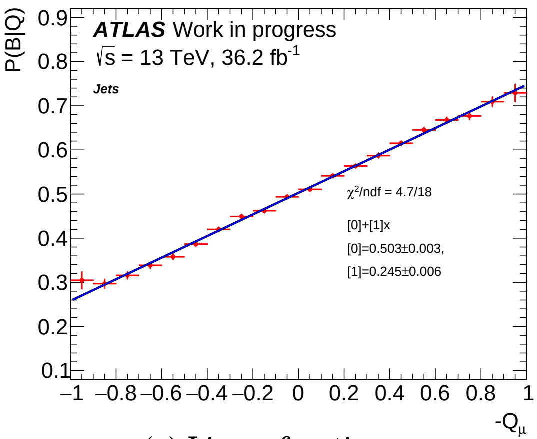

(a) Linear function.

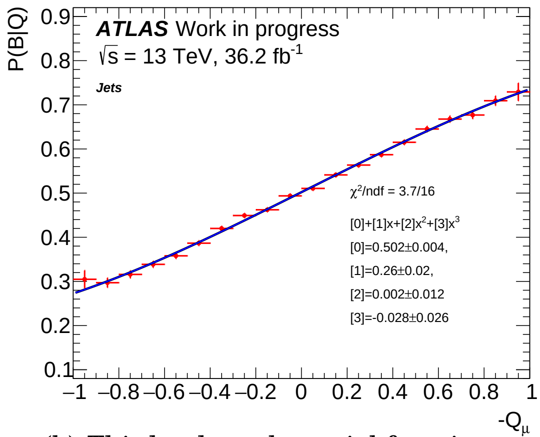

(b) Third order polynomial function.

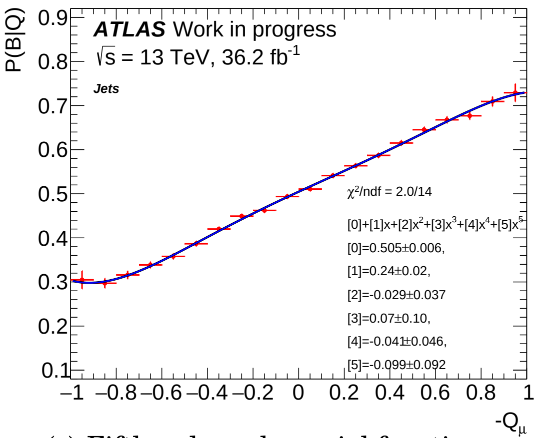

(c) Fifth order polynomial function.

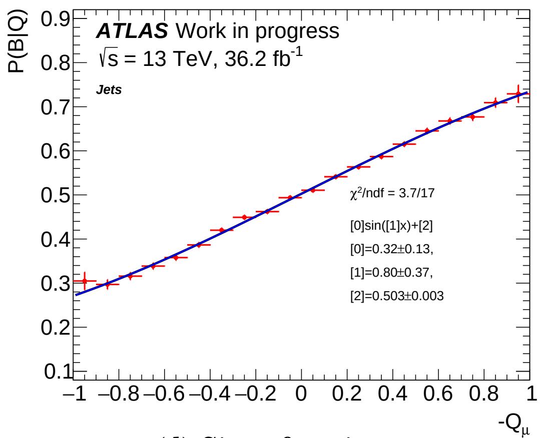

(d) Sinus function

FIGURE A.3. Alternative parametrisation of the B^+ tag probability distribution for jets.

APPENDIX

B

PUNZI TERMS

The maximum likelihood fit is used in the B_s^0 decay width fit. This procedure uses the template functions for describing the each signal and background components, each consisting of the probability density function. As the variables of these fucntions also have some distribution, the Punzi terms are necessary.
For better explanation, an experiment, in which two types of events (A and B) can occur, is considered. With given a fraction of A events f and probability functions of A and B,

$$\begin{aligned} p(x|A) &= N(0,\sigma) \\ p(x|B) &= N(1,\sigma), \end{aligned} \tag{B.1}$$

the likelihood function is

$$L(f) = \prod_i [fN(x_i,0,\sigma) + (1-f)N(x_i,1,\sigma)], \tag{B.2}$$

where $N(x,\mu,\sigma)$ indicates the Gaussian function in observable x, which is considered to have constant resolution.
Usually, the each measurement of observable x_i has different resolution σ_i, giving the likelihood function

$$L(f) = \prod_i [fN(x_i,0,\sigma_i) + (1-f)N(x_i,1,\sigma_i)]. \tag{B.3}$$

However, this likelihood does not describe the observable x. The reason is that we have now set of observables x_i, σ_i and the probability density functions depends on both. This means that the likelihood function (B.3) must be written as

$$\begin{aligned} L(f) &= \prod_i [f\,p(x_i,\sigma_i|A) + (1-f)p(x_i,\sigma_i|B)] = \\ &= \prod_i [f N(x_i,0,\sigma_i)p(\sigma_i|A) + (1-f)N(x_i,1,\sigma_i)p(\sigma_i|B)], \end{aligned} \tag{B.4}$$

where $p(\sigma_i|A)$ and $p(\sigma_i|B)$ are the probability density functions of σ_i, also called the Punzi terms. Note that the $p(\sigma_i|A)$ and $p(\sigma_i|B)$ are distributions, but σ_i is just the number in the Gaussian function. In the case of $p(\sigma_i|A) = p(\sigma_i|B)$, the Punzi terms can be factorised out and the likelihood (B.4) becomes (B.3).

APPENDIX C

FULL RESULTS OF THE $B_s^0 \rightarrow J/\psi\phi$ FIT

Fit Parameter	Fitted value	Range	step
$\lvert A_0(0)\rvert^2$	$0.549224238 \pm 0.0021191495$	$(0 \rightarrow 1)$	1.00E-06
$\lvert A_{\parallel}(0)\rvert^2$	$0.212525259 \pm 0.002756345$	$(0 \rightarrow 1)$	1.00E-06
$\lvert A_S(0)\rvert^2$	$0.135103073 \pm 0.0046852246$	$(0 \rightarrow 1)$	1.00E-06
Γ_S [ps^{-1}]	$0.663708057 \pm 0.0018682362$	$(0.4 \rightarrow 0.9)$	1.00E-06
$\Delta\Gamma_s$ [ps^{-1}]	$0.118851392 \pm 0.0069234722$	$(0.01 \rightarrow 0.6)$	1.00E-06
ΔM [$\hbar$ps^{-1}]	17.757	$(17.757 \rightarrow 17.757)$	0
ϕ_S	$-0.0784511591 \pm 0.0459048062$	$(-20 \rightarrow 20)$	1.00E-06
$\delta_{\parallel}$ [rad]	$3.14147762 \pm 0.0392423911$	$(-10 \rightarrow 10)$	1.00E-06
$\delta_{\perp}$ [rad]	$2.6800988 \pm 0.143592715$	$(-6 \rightarrow 7.9)$	1.00E-06
$\delta_{\perp} - \delta_S$ [rad]	$-0.0693485685 \pm 0.0170453732$	$(-10 \rightarrow 10)$	1.00E-06
$m_{B_s^0}$ [GeV]	$5.36694108 \pm 0.00006424$	$(5 \rightarrow 6)$	1.00E-06
$SF\tau_{B_s^0}$	$1.02914261 \pm 0.0013808208$	$(0.8 \rightarrow 1.2)$	1.00E-06
f_sig	$0.15406627 \pm 0.0004814702$	$(0 \rightarrow 1)$	1.00E-06
σ_1 [GeV]	$0.0273420768 \pm 0.000552874$	$(0 \rightarrow 0.3)$	1.00E-06
$Sigma1_{frac}$	$0.744453501 \pm 0.0120634382$	$(0 \rightarrow 1)$	1.00E-06
σ_2 [GeV]	$0.0618517408 \pm 0.001635726$	$(0 \rightarrow 0.3)$	1.00E-06
$Sigma12_{frac}$	$0.706494798 \pm 0.0144782882$	$(0 \rightarrow 1)$	1.00E-06
$\sigma 3$ [GeV]	$0.0130558292 \pm 0.0002378607$	$(0 \rightarrow 0.3)$	1.00E-06
$mExp_{Scale}$	$0.534851186 \pm 0.029816783$	$(0 \rightarrow 1000)$	1.00E-06
$mExp_{Slope}$ [MeV]	$0.407582544 \pm 0.0137984756$	$(0 \rightarrow 1000)$	1.00E-06

Fit Parameter	Fitted value	Range	step
f_{prompt}	$0.660834268 \pm 0.0012223026$	$(0 \to 1)$	1.00E-06
$f_{indirect}$	$0.228312888 \pm 0.0017810093$	$(0 \to 1)$	1.00E-06
f_{tails}	$0.0772318887 \pm 0.0015310335$	$(0 \to 1)$	1.00E-06
τ_{fast} [ps]	$0.219759077 \pm 0.001077001$	$(0.01 \to 10)$	1.00E-06
τ_{slow} [ps]	$1.65129227 \pm 0.0098129233$	$(0.01 \to 10)$	1.00E-06
τ_{tails} [ps]	$0.137880111 \pm 0.0016854156$	$(0.01 \to 10)$	1.00E-06
$f_{BdK\star}$	0.0331341	$(0 \to 1)$	0
$\tau BdBs$[ps]	1.5441	$(0.5 \to 2)$	0
$mpv_{BdK\star}$ [GeV]	5.38647	$(5 \to 6)$	0
$mArea_{BdK\star}$	0.512802	$(0.5 \to 2)$	0
$\sigma_{BdK\star}$ [GeV]	0.0515447	$(0.01 \to 1)$	0
$TagMethod_{sig} = 0$	0.782261	$(0 \to 1)$	0
$TagMethod_{sig} = 1$	0.0385353	$(0 \to 1)$	0
$TagMethod_{sig} = 2$	0.0274752	$(0 \to 1)$	0
$TagMethod_{sig} = 3$	0.135379	$(0 \to 1)$	0
$TagMethod_{sig} = 4$	0	$(0 \to 1)$	0
$TagMethod_{sig} = 5$	0.0128903	$(0 \to 1)$	0
$TagMethod_{bck} = 0$	0.819982	$(0 \to 1)$	0
$TagMethod_{bck} = 1$	0.0331372	$(0 \to 1)$	0
$TagMethod_{bck} = 2$	0.0255813	$(0 \to 1)$	0
$TagMethod_{bck} = 3$	0.108409	$(0 \to 1)$	0
$TagMethod_{bck} = 4$	0	$(0 \to 1)$	0
$TagMethod_{bck} = 5$	0.0128903	$(0 \to 1)$	0
$TagMethod_1 f_{sig}(+1)$	0.0732523	$(0 \to 1)$	0
$TagMethod_1 f_{sig}(-1)$	0.081911	$(0 \to 1)$	0
$TagMethod_2 f_{sig}(+1)$	0.11977	$(0 \to 1)$	0
$TagMethod_2 f_{sig}(-1)$	0.125184	$(0 \to 1)$	0
$TagMethod_3 f_{sig}(+1)$	0.0375708	$(0 \to 1)$	0
$TagMethod_3 f_{sig}(-1)$	0.0386014	$(0 \to 1)$	0
$TagMethod_5 f_{sig}(+1)$	0.178204	$(0 \to 1)$	0
$TagMethod_5 f_{sig}(-1)$	0.161693	$(0 \to 1)$	0
$TagMethod_1 f_{bck}(+1)$	0.051177	$(0 \to 1)$	0
$TagMethod_1 f_{bck}(-1)$	0.0526305	$(0 \to 1)$	0
$TagMethod_2 f_{bck}(+1)$	0.073741	$(0 \to 1)$	0
$TagMethod_2 f_{bck}(-1)$	0.0801508	$(0 \to 1)$	0
$TagMethod_3 f_{bck}(+1)$	0.0324313	$(0 \to 1)$	0
$TagMethod_3 f_{bck}(-1)$	0.0323235	$(0 \to 1)$	0
$TagMethod_5 f_{bck}(+1)$	0.159002	$(0 \to 1)$	0
$TagMethod_5 f_{bck}(-1)$	0.160591	$(0 \to 1)$	0

Fit Parameter	Fitted value	Range	step
$tag1Sig_{exp}1$	-15.431	$(-200 \to 0)$	0
$tag1Sig_{exp}2$	10.837	$(0 \to 200)$	0
$tag1Sigf_{Fraction1}$	0.2105	$(0 \to 1)$	0
$tag1Sigf_{Fraction2}$	0.57109	$(0 \to 1)$	0
$tag1Sig_{min}$	0.193521	$(0 \to 1)$	0
$tag1Sig_{max}$	0.810954	$(0 \to 1)$	0
$tag2Sig_{\mu}$	0.514722	$(0 \to 1)$	0
$tag2Sig_{\sigma}$	0.25	$(0 \to 0.3)$	0
$tag2Sig_{min}$	0.295062	$(0 \to 1)$	0
$tag2Sig_{max}$	0.717363	$(0 \to 1)$	0
$tag3Sig_{\mu}$	0.50503	$(0 \to 1)$	0
$tag3Sig_{\sigma}$	0.11464	$(0 \to 1)$	0
$tag3Sig_{min}$	0.273089	$(0 \to 1)$	0
$tag3Sig_{max}$	0.735249	$(0 \to 1)$	0
$tag5Sig_{exp}1$	-27.364	$(-100 \to 0)$	0
$tag5Sig_{exp}2$	40.158	$(0 \to 100)$	0
$tag5Sigf_{Fraction1}$	0.24039	$(0 \to 1)$	0
$tag5Sigf_{Fraction2}$	0.51961	$(0 \to 1)$	0
$tag5Sig_{m}in$	0.246658	$(0 \to 1)$	0
$tag5Sig_{m}ax$	0.754704	$(0 \to 1)$	0
$tag1Bck_{e}xp1$	-45	$(-1500 \to 0)$	0
$tag1Bck_{e}xp2$	25.18	$(0 \to 1000)$	0
$tag1Bck_{P}1$	-1.192	$(-200 \to 200)$	0
$tag1Bck_{P}2$	1.003	$(-200 \to 200)$	0
$tag1Bckf_{Fraction1}$	0.04154	$(0 \to 1)$	0
$tag1Bckf_{Fraction2}$	0.8895	$(0 \to 1)$	0
$tag1Bck_{min}$	0.193521	$(0 \to 1)$	0
$tag1Bck_{max}$	0.810954	$(0 \to 1)$	0
$tag2Bck_{\mu}$	0.50074	$(0 \to 1)$	0
$tag2Bck_{\sigma}$	0.15496	$(0 \to 0.25)$	0
$tag2Bck_{min}$	0.295062	$(0 \to 1)$	0
$tag2Bck_{max}$	0.717363	$(0 \to 1)$	0
$tag3Bck_{P1}$	-1178.9	$(-2000 \to 2000)$	0
$tag3Bck_{P2}$	5769.6	$(-6000 \to 6000)$	0
$tag3Bck_{P3}$	-3351.1	$(-4000 \to 4000)$	0
$tag3Bck_{P4}$	-7259.9	$(-8000 \to 8000)$	0
$tag3Bck_{P5}$	-1574.9	$(-2000 \to 2000)$	0
$tag3Bck_{P6}$	8725.6	$(-9000 \to 9000)$	0
$tag3Bck_{P7}$	11047	$(-12000 \to 12000)$	0
$tag3Bck_{P8}$	-13128	$(-20000 \to 20000)$	0

Fit Parameter	Fitted value	Range	step
$tag3Bck_{min}$	0.273089	$(0 \to 1)$	0
$tag3Bck_{max}$	0.735249	$(0 \to 1)$	0
$tag5Bck_{exp}1$	-79.416	$(-100 \to 0)$	0
$tag5Bck_{exp}2$	57.911	$(0 \to 100)$	0
$tag5Bck_{P1}$	-3.5039	$(-200 \to 200)$	0
$tag5Bck_{P2}$	3.4425	$(-200 \to 200)$	0
$tag5Bckf_{Fraction}1$	0.10321	$(0 \to 1)$	0
$tag5Bckf_{Fraction}2$	0.78808	$(0 \to 1)$	0
$tag5Bck_{min}$	0.246658	$(0 \to 1)$	0
$tag5Bck_{max}$	0.754704	$(0 \to 1)$	0

FitStatus	1
HesseStatus	1
MinosStatus	0
fcn	12439501.1

Bibliography

[1] C. Patrignani et al. Review of Particle Physics. *Chin. Phys.*, C40(10):100001, 2016.

[2] Georges Aad et al. Observation of a new particle in the search for the Standard Model Higgs boson with the ATLAS detector at the LHC. *Phys. Lett.*, B716:1–29, 2012.

[3] M. Agostini et al. A test of electric charge conservation with Borexino. *Phys. Rev. Lett.*, 115:231802, 2015.

[4] D. H. Perkins. *Introduction to high energy physics*. 1982. ISBN 9780521621960.

[5] B. P. Abbott et al. Observation of Gravitational Waves from a Binary Black Hole Merger. *Phys. Rev. Lett.*, 116(6):061102, 2016.

[6] Kimmo Kainulainen, Kimmo Tuominen, and Jussi Virkajärvi. A model for dark matter, naturalness and a complete gauge unification. *JCAP*, 1507:034, 2015.

[7] C.W. Misner, K.S. Thorne, and J.A. Wheeler. *Gravitation*. 1970. ISBN 9781400889099.

[8] Barry R. Holstein. Graviton Physics. *Am. J. Phys.*, 74:1002–1011, 2006.

[9] H. L. Anderson, E. Fermi, E. A. Long, and D. E. Nagle. Total Cross-sections of Positive Pions in Hydrogen. *Phys. Rev.*, 85:936, 1952.

[10] O. W. Greenberg. Spin and unitary-spin independence in a paraquark model of baryons and mesons. *Phys. Rev. Lett.*, 13:598–602, Nov 1964. URL `https://link.aps.org/doi/10.1103/PhysRevLett.13.598`.

[11] O. W. Greenberg. Spin and Unitary Spin Independence in a Paraquark Model of Baryons and Mesons. *Phys. Rev. Lett.*, 13:598–602, 1964.

[12] Wolfgang Pauli. Pauli letter collection: letter to Lise Meitner. Typed copy. URL `http://cds.cern.ch/record/83282`.

[13] P. A. R. Ade et al. Planck 2015 results. XIII. Cosmological parameters. *Astron. Astrophys.*, 594:A13, 2016.

[14] G. Zweig. An SU(3) model for strong interaction symmetry and its breaking. Version 2. In D.B. Lichtenberg and Simon Peter Rosen, editors, *DEVELOPMENTS IN THE QUARK THEORY OF HADRONS. VOL. 1. 1964 - 1978*, pages 22–101. 1964.

[15] Murray Gell-Mann. A Schematic Model of Baryons and Mesons. *Phys. Lett.*, 8: 214–215, 1964.

[16] J. J. Aubert et al. Experimental observation of a heavy Particle J. *Adv. Exp. Phys.*, 5:128, 1976.

[17] S. W. Herb et al. Observation of a Dimuon Resonance at 9.5-GeV in 400-GeV Proton-Nucleus Collisions. *Phys. Rev. Lett.*, 39:252–255, 1977.

[18] F. Abe et al. Observation of top quark production in $\bar{p}p$ collisions. *Phys. Rev. Lett.*, 74:2626–2631, 1995.

[19] Ahmed Ali, Christian Hambrock, and M. Jamil Aslam. A Tetraquark interpretation of the BELLE data on the anomalous Upsilon(1S) pi+pi- and Upsilon(2S) pi+pi- production near the Upsilon(5S) resonance. *Phys. Rev. Lett.*, 104:162001, 2010.

[20] Roel Aaij et al. Observation of the resonant character of the $Z(4430)^-$ state. *Phys. Rev. Lett.*, 112(22):222002, 2014.

[21] Roel Aaij et al. Observation of $J/\psi p$ Resonances Consistent with Pentaquark States in $\Lambda_b^0 \to J/\psi K^- p$ Decays. *Phys. Rev. Lett.*, 115:072001, 2015.

[22] P. A. M. Dirac. A Theory of Electrons and Protons. *Proc. Roy. Soc. Lond.*, A126:360, 1930.

[23] C. S. Wu, E. Ambler, R. W. Hayward, D. D. Hoppes, and R. P. Hudson. Experimental Test of Parity Conservation in Beta Decay. *Phys. Rev.*, 105:1413–1414, 1957.

[24] J. H. Christenson, J. W. Cronin, V. L. Fitch, and R. Turlay. Evidence for the 2π Decay of the K_2^0 Meson. *Phys. Rev. Lett.*, 13:138–140, 1964.

[25] Bernard Aubert et al. Search for CPT and Lorentz violation in B0 - anti-B0 oscillations with dilepton events. *Phys. Rev. Lett.*, 100:131802, 2008.

[26] Nima Arkani-Hamed, Hsin-Chia Cheng, Markus Luty, and Jesse Thaler. Universal dynamics of spontaneous lorentz violation and a new spin-dependent inverse-square law force. *Journal of High Energy Physics*, 2005(07):029, 2005.

[27] D. Babusci et al. Test of CPT and Lorentz symmetry in entangled neutral kaons with the KLOE experiment. *Phys. Lett.*, B730:89–94, 2014.

[28] Nicola Cabibbo. Unitary Symmetry and Leptonic Decays. *Phys. Rev. Lett.*, 10: 531–533, 1963. [,648(1963)].

[29] P. J. Woods and C. N. Davids. Nuclei beyond the proton drip-line. *Annual Review of Nuclear and Particle Science*, 47(1):541–590, 1997.

[30] *The CKM matrix and the unitarity triangle. Workshop, CERN, Geneva, Switzerland, 13-16 Feb 2002: Proceedings*, 2003. doi: 10.5170/CERN-2003-002-corr. URL `http://lss.fnal.gov/cgi-bin/find_paper.pl?conf-02-422`.

[31] John Ellis. Where is Particle Physics Going? *Int. J. Mod. Phys.*, A32(34):1746001, 2017.

[32] S. W. Herb et al. Observation of a Dimuon Resonance at 9.5-GeV in 400-GeV Proton-Nucleus Collisions. *Phys. Rev. Lett.*, 39:252–255, 1977.

[33] E. Norrbin and T. Sjostrand. Production and hadronization of heavy quarks. *Eur. Phys. J.*, C17:137–161, 2000.

[34] Roel Aaij et al. Measurement of the $B_s^0 \to \mu^+\mu^-$ branching fraction and effective lifetime and search for $B^0 \to \mu^+\mu^-$ decays. *Phys. Rev. Lett.*, 118(19):191801, 2017.

[35] R. Aaij et al. Effective lifetime measurements in the $B_s^0 \to K^+K^-$,$B^0\imath K^+\pi^-$ and $B_s^0 \to \pi^+K^-$ decays. *Phys. Lett.*, B736:446–454, 2014. doi: 10.1016/j.physletb.2014.07.051.

[36] Sheldon Stone. New physics from flavour. In *Proceedings, 36th International Conference on High Energy Physics (ICHEP2012): Melbourne, Australia, July 4-11, 2012*, volume ICHEP2012, page 033, 2013.

[37] Georges Aad et al. Measurement of the CP-violating phase ϕ_s and the B_s^0 meson decay width difference with $B_s^0 \to J/\psi\phi$ decays in ATLAS. *JHEP*, 08:147, 2016.

[38] Abazov et al. Measurement of the cp-violating phase $\phi_s^{J/\psi\phi}$ using the flavor-tagged decay $B_s^0 \to j/\psi\phi$ in 8 fb^{-1} of $p\overline{p}$ collisions. *Phys. Rev. D*, 85:032006, Feb 2012.

[39] Yuehong Xie. CP Violation in Bs->J/psi phi. In *Proceedings, 10th Conference on Flavor Physics and CP Violation (FPCP 2012): Hefei, Anhui, China, May 21-25, 2012*, 2012.

[40] `https://espace.cern.ch/acc-tec-sector/default.aspx`, . Accessed: 2018-04-13.

[41] Georges Aad et al. Observation of a new χ_b state in radiative transitions to $\Upsilon(1S)$ and $\Upsilon(2S)$ at ATLAS. *Phys. Rev. Lett.*, 108:152001, 2012.

[42] G. Apollinari, O. Brüning, T. Nakamoto, and Lucio Rossi. High Luminosity Large Hadron Collider HL-LHC. *CERN Yellow Report*, (5):1–19, 2015.

[43] `http://home.web.cern.ch/about/accelerators`, . Accessed: 2018-04-13.

[44] `http://home.cern/about/experiments`, . Accessed: 2018-04-13.

[45] G. Aad et al. The ATLAS Experiment at the CERN Large Hadron Collider. *JINST*, 3:S08003, 2008. doi: 10.1088/1748-0221/3/08/S08003.

[46] Alexander V. Zlobin. *Superconducting Magnets - Principles, Operation, and Applications*. 2014. ISBN 9780471346081.

[47] M Capeans, G Darbo, K Einsweiller, M Elsing, T Flick, M Garcia-Sciveres, C Gemme, H Pernegger, O Rohne, and R Vuillermet. ATLAS Insertable B-Layer Technical Design Report. Technical Report CERN-LHCC-2010-013. ATLAS-TDR-19, Sep 2010.

[48] ATLAS Phase-II Upgrade Scoping Document. Technical Report CERN-LHCC-2015-020. LHCC-G-166, CERN, Geneva, Sep 2015.

[49] C. Nellist. Achievements of the ATLAS Upgrade Planar Pixel Sensors R&D Project. In *Proceedings, 10th International Conference on Position Sensitive Detectors (PSD10): Surrey, UK, September 7-12, 2014*, volume 10, page C01027, 2015.

[50] A. Ruiz Martínez. The Run-2 ATLAS Trigger System. *J. Phys. Conf. Ser.*, 762(1): 012003, 2016.

[51] Morad Aaboud et al. Performance of the ATLAS Trigger System in 2015. *Eur. Phys. J.*, C77(5):317, 2017.

[52] Georges Aad et al. Muon reconstruction performance of the ATLAS detector in proton–proton collision data at $\sqrt{s}$ =13 TeV. *Eur. Phys. J.*, C76(5):292, 2016.

[53] Nicola Orlando. Muon reconstruction efficiency measurement in the ATLAS experiment. *EPJ Web Conf.*, 28:12040, 2012.

[54] R. Nicolaidou, L. Chevalier, S. Hassani, J. F. Laporte, E. Le Menedeu, and A. Ouraou. Muon identification procedure for the ATLAS detector at the LHC using Muonboy reconstruction package and tests of its performance using cosmic rays and single beam data. *J. Phys. Conf. Ser.*, 219:032052, 2010.

[55] Muon reconstruction performance in early $\sqrt{s}$ = 13 TeV data. Technical Report ATL-PHYS-PUB-2015-037, CERN, Geneva, Aug 2015.

[56] `http://proj-gaudi.web.cern.ch/proj-gaudi/`, . Accessed: 2018-04-13.

[57] Jack Cranshaw. Early experience with the Run 2 ATLAS analysis model. First experience with the new ATLAS analysis model. Technical Report ATL-SOFT-PROC-2016-007, CERN, Geneva, Oct 2016.

[58] `https://root.cern.ch/`, . Accessed: 2018-04-13.

[59] R. Brun and F. Rademakers. ROOT: An object oriented data analysis framework. *Nucl. Instrum. Meth.*, A389:81–86, 1997.

[60] `http://roofit.sourceforge.net/`, . Accessed: 2018-04-13.

[61] Muriel Pivk. sPLOT: A Quick introduction. In *Statistical Problems in Particle Physics, Astrophysics and Cosmology (PHYSTAT 05): Proceedings, Oxford, UK, September 12-15, 2005*, pages 173–177, 2006.

[62] Vardan Khachatryan et al. Measurement of the CP-violating weak phase ϕ_s and the decay width difference $\Delta\Gamma_s$ using the $\mathrm{B}_s^0 \to J/\psi\phi(1020)$ decay channel in pp collisions at $\sqrt{s}$ = 8 TeV. *Phys. Lett.*, B757:97–120, 2016.

[63] Roel Aaij et al. Precision measurement of CP violation in $B_s^0 \to J/\psi K^+K^-$ decays. *Phys. Rev. Lett.*, 114(4):041801, 2015.